Numerical modelling of a moist casting self-assembly process leading to ordered macro-porous polymer films.

Battenbo, Huw

Numerical modelling of a moist casting self-assembly process leading to ordered macro-porous polymer films

Huw Battenbo

School of Engineering

Swansea University UK

Submitted to the University of Wales in fulfilment of the requirements for the Degree of Doctor of Philosophy

2008

DECLARATION

This work has not previously been accepted in substance for any degree and is not being concurrently submitted in candidature for any degree.

Signed. ..... (Candidate)

Date 04-19-2009

STATEMENT 1

This thesis is the result of my own investigations, except where otherwise stated. Where correction services have been used, the extent and nature of the correction is clearly marked in a footnote(s)
Other sources are acknowledged by footnotes giving explicit references. A bibliography is appended.

Signed. ..... (Candidate)

Date 04-19-2009

STATEMENT 2

I hereby give consent for my thesis, if accepted, to be available for photocopying and for inter-library loan, and for the title and summary to be made available to outside organisations.

Signed... ..... (Candidate)

Date 04-19-2009

Summary

This thesis presents to our knowledge the first investigation into using a numerical modelling method to simulate the role of the bulk casting conditions in a moist casting method derived from the formation of condensed water droplets 'breath figures'. The results show that the casting solution surface can obtain a constant temperature and induce a constant rate of condensation through part of a casting procedure if heat transport at the bottom of the substrate when made of glass, is sufficient to maintain the temperature here constant through the experiment. Predictions are made for the lowest chamber relative humidity for which the polymer material produced should posses a porous architecture when using either carbon disulphide or chloroform as a solvent; these results are in good agreement with experimental observations in the literature suggesting that our simulations of the thermodynamics are accurate. Further results show that the thickness of the substrate can change the timescale of the process, and an adjustment of the evaporation rate leads to a change in the amount of deposited condensate through an induced change in liquid temperature. This result suggests that the process could be manipulated by simply accurately changing the substrate thickness with other conditions remaining constant. In conjunction an image analysis technique is developed to assess the quality of these macro-porous films.

The automation of this technique allows large amounts of image data to be analysed which can be used to assess improvements to long range order in casting experiments. Standard optical microscopy and a micro-manipulator unit allowed an assessment radially through whole films created under differing casting conditions. The findings of these results are discussed in detail.

Acknowledgements

Firstly I would like to thank Dr Richard Cobley who has always been willing to listen to my thoughts and ideas. When I started this work I had little to none experience in numerical modelling. Dr Cobleys expertise in this area allowed me to reach such a level of competence as to realise simulation of my theoretical ideas regarding this subject, frequent trips to the gym also helped ease frustration. For this I am indebted to him.

My thanks to Dr Alex Labansky for our in depth discussions about my work, or any subject matter. These conversations were always insiteful. Dr Labansky also introduced me to typesetting in Latex, which has aided the writing process substantially. For this I am truly grateful.

Thanks to Dr Rob Bryant as a Chemical Engineer, who offered his opinion regarding some of the physical phenomenon involved in this work.

My parents gave their full support during my work as always, which came as no surprise to me. I must also thank some special people, Pete and Pip.

I must also thank my grandfather John Battenbo, he has been a great inspiration to me over the course of my education both as a mathematician and a person. I am very proud that at the age of 79 he still has enough thirst for knowledge to undertake studying for another degree. I hope my thirst for knowledge and understanding will show the same longevity.

Finally I would like to thank my supervisor Professor Steve Wilkes who introduced me to this subject and has provided continuing encouragement over the course of my work. He has remained positive despite some set backs, for this support he will always have my gratitude.

Contents

List of Figures

List of Tables

Chapter 1

Introduction

This thesis discusses the production of highly-ordered macro-porous materials, which in the literature have shown to have pore sizes ranging from 50nm to 20μm. Highly ordered porous materials with these topographical scales have many potential applications across a varying range of technological areas. Some examples include the basis for data storage systems, photonic band gap materials, templates for cell culture and pico-litre beakers for bio-analysis techniques. Creating such heavily sort after materials has been attempted using a variety of techniques. Many of these techniques are so called 'top down' techniques, the most commonly referred to of which is photolithography. The technique of photolithography uses photons to transfer patterns from a mask onto a substrate [2]. In this patterning technique, silicon is coated with a photo resistive material. A photo resistive material or photo-resist is a material that changes chemical composition when exposed to light. A mask is

used, such as to expose only the desired regions of photo-resist to a light source. When the mask is removed, only the unexposed regions remain on the silicon substrate. This patterned substrate now serves as a stencil for structuring the silicon by etching. This process involves many stages, all of which must be achieved with success, in order to produce an ordered film with high resolution. Due to the time consumption, and cost of such processes, so called 'bottom up techniques' are attracting much attention. These techniques predominantly use self-assembled templates. Such techniques are very attractive because they could reduce cost and time expenditure. Some of these techniques use colloidal crystals to produce templates[3][4]. Usually close packed mono-disperse colloidal spheres are used to form a template into which a liquid (the desired film material) is poured. The liquid subsequently solidifies. The temperature of the mix is then increased such that the colloidal spheres are extracted, leaving in their place a monodisperse porous film.

Bottom up techniques using emulsions have also been used to prepare macro-porous films [5]. Instead of using solid spheres, these techniques use liquid droplets to form the template. An emulsion of roughly uniform-sized droplets is cast onto a suspending solution whereby the droplets self-assemble into a colloidal crystal. The whole sample is then treated so that the droplets are extracted leaving in their place a macro-porous film. This process has been demonstrated for titania, silica and zirconia [5]. There are some problems

associated with this process. In order to produce a mono-disperse pore size distribution in the final film, the droplet size distribution of the emulsion must also be mono-disperse. A fractionation process is usually used, but this is time consuming and it is difficult to produce large quantities of droplets with uniform size. Also the self-assembly process is non perfect, and using external fields and shear flows has been suggested as a means of aiding the process.

Another experimental procedure for producing a macro-porous film is discussed by a team from the Institute of Polymer Research in Dresden [6]. In this technique small areas are hydrophilized by micro-contact printing of undecanoic acid. The new material is then exposed to a water-saturated atmosphere, and the material cooled to below the corresponding dewpoint temperature. Preferential condensation of water droplets then occurs on the hydrophilized sites. This material is then transferred to a water immiscible phase in which a hydrophobic polymer is dissolved. The solution is then allowed to dry and a polymer film is produced, with voids at the locations of the previously condensed water droplets which subsequently evaporate. This technique once again has many stages which must be performed correctly in order to produce the end result; in theory this technique is highly desirable because any structure could in principle be produced on the polymer, as long as the initial pattern could be printed on the mask. However, creating the

mask in the first place is the inverse task of the latter as the mask must have the inverse topography, so this process cannot really be considered as self-assembly. Also if the locations of the condensation sites are too close together, cohesive forces between the condensed droplets will start to cause coalescence; this defines the minimal size scale obtainable using this method.

This thesis discusses a method of preparation of such porous materials using a self- assembling moistcasting method. The materials produced have been called 'breath figures' (see figure 1.1).

The pore size obtained in the casting process can be controlled by controlling the casting conditions, although at present no quantitative relation between all of the casting conditions and pore size has been reported. The templating method is very desirable as it is self-assembling in nature and porous materials can be prepared in a ten minute epoch, with the process completed. Unlike other techniques, there is no template that needs to be removed at the end of the process. Condensed water droplets serve as the template in the process and evaporate, leaving in their place a macro-porous film. In this process, a polymer solvent solution is allowed to evaporate in a humid environment. As the solvent evaporates, transfer of latent heat of vaporization cools the region close to the evaporating interface. This cooling process causes rapid condensation of water vapour from the surrounding air, forming water droplets on the surface of the evaporating solution. When all

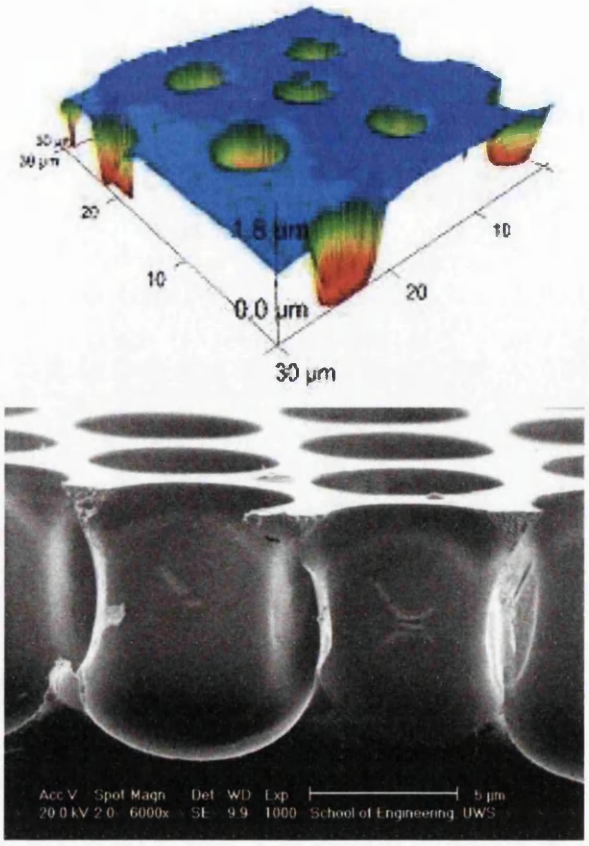

Figure 1.1: Images of polymer films produced using the breath figure method (i)Atomic force microscopy (ii) Scanning electron microscopy

the solvent has been evaporated as well as the condensed water droplets, cavities are left at the locations of the previously condensed water droplets set in the polymer precursor. Unlike the method discussed previously, involving micro-contact printing and creation of hyrophilized cites, non-coalescing behaviour between condensed droplets has been observed and high speed video microphotography studies show the condensed water droplets displaying hard sphere like behaviour [7].

In the literature, the dynamics of the process described above often contain generalizations, and the casting method is sometimes made to look deceptively simple because only a few variables for the processes are quoted. Often, images of small areas of films are displayed to portray a general trend in the pore size obtained in relation to casting conditions; however in contradiction workers have noted that pore size often varies unpredictably throughout the film surface [8]. In a review paper on the subject Uwe Bunz discusses this very issue. "The breath figure method of templating polymer films has complex thermodynamic, kinetic and entropic underpinnings which are not yet understood". The study carried out in this thesis uses this as its motivation. The aim is to achieve a better experimental approach in order to make experiments repeatable and avoid generalizations in the literature. Numerical modelling is used to understand which variables should be quoted in a growth experiment to characterize the process that took place.

This numerical modelling in conjunction with experimental procedure is used to understand how one might control the pore size in each film, and strive for a quantitative relation between casting conditions, pore size and order. An attempt is made to understand if this is possible. This study aims to understand the process of formation in greater detail, in order to understand which factors will influence the process to the greatest extent. The study mainly focuses on the prediction of condensation rate of water

vapour from the surrounding environment and not surface-droplet, droplet-droplet interactions. The numerical model is an attempt to quantify the rate of condensation of water vapour from the air onto the surface of the solution under different environmental and material conditions. As will be discussed in the subsequent chapters, a variety of mechanisms have been proposed for the observed non- coalescence of the water droplets on the surface. If one can make quantitative predictions for the prevailing thermodynamic conditions using a given experimental setup, then one can start to see if the onset of these mechanisms is plausible. The onset of these mechanisms might be key to the degree of ordering, so experiments could possibly be created to facilitate this onset. Knowledge of condensation rate during the process of breath figure formation could also prove useful for determining the rate of deposition and timescale in random sequential adsorption modelling which has already been used to study the growth of breath figures [9][10]. A marriage of these two concepts could lead to a quantitative relation between casting conditions and pore size.

Chapter 2

Breath Figures

In this thesis the main topic of interest is a self-assembly technique for producing macro-porous materials. This method is based on a phenomenon which has been described as the formation of breath figures. This term is a general term used to describe the formation of patterns of water droplets on cooled surfaces arising from the process of condensation under partial wetting conditions. The phenomena was first reported by Aitken in 1893 [11], shortly followed by Rayleigh [12]. Beysens and Knobler later described the formation of the patterns on solid surfaces [13] and on the surface of viscous oil [14] at constant super-saturations. In the later publication, comparisons are made between the growth dynamics in the two cases via optical microscopy studies. In the case of growth on a fluid substrate (viscous oil), the average droplet diameter is observed to grow according to two distinct dynamic processes. At early times the growth of the average droplet is found to grow according to a

power law $\langle D \rangle \propto t^{\frac{1}{3}}$ and at a later time according to $\langle D \rangle \propto t$ where $\langle D \rangle$ is the average droplet diameter, and t is time. The authors attribute the crossover between the two regimes to a result of a transition between times when the mechanism of growth is dominated by the growth of isolated droplets and a time when the droplets achieve a size such that effects of coalescence become dominant. The growth dynamics on the solid substrate showed some significant differences. The workers were not able to observe a regime dominated by isolated droplet growth at early times, as in the case of the liquid. After 0-1s a growth law of $t^{0.7}$ followed, indicating a coalescence-dominated stage. It is concluded that this observation is an effect attributable to the differences in initial droplet density caused by the differences in available nucleation sites in the two cases, mainly due to the higher surface roughness in the case of the solid substrate. Another important observation is that the polydispersity of droplet size in the case of the liquid substrate is lesser, which it is suggested could be attributable to a suppression of the coalescence-dominated stage due to the presence of the liquid oil.

Later (1994) Widawski and co-workers [15] would discover that this phenomenon is applicable to the production of porous polymer membranes. The workers noticed the appearance of regular hexagonal arrays of pores, when preparing polystyrene-polyparaphenylene (PS-PPP) block copolymer films, for radiation scattering experiments, by evaporating solutions of the polymer

in carbon disulphide. The appearance of the arrays was only observed in the presence of a moist airflow. It was noted that the solution concentration could also influence the production of mono or multi-layered structures, and also that the length of the polystyrene(PS) sequences in PS-PPP copolymers, or the number of arms in star-like Ps could also influence the pore size and ordering. The workers observed a general increase in pore size with increasing relative molecular weight and that regular arrays could be produced for relative molecular masses between 1,500 and 50,000. Attempts to produce the structures with polymers without polystyrene sequences were unsuccessful.

This discovery lead to the generally accepted technique which is now used for the casting procedure depicted in figure 2.1, although it must be noted that other techniques have been used such as lowering the non condensable gas content in a humid environment [16].

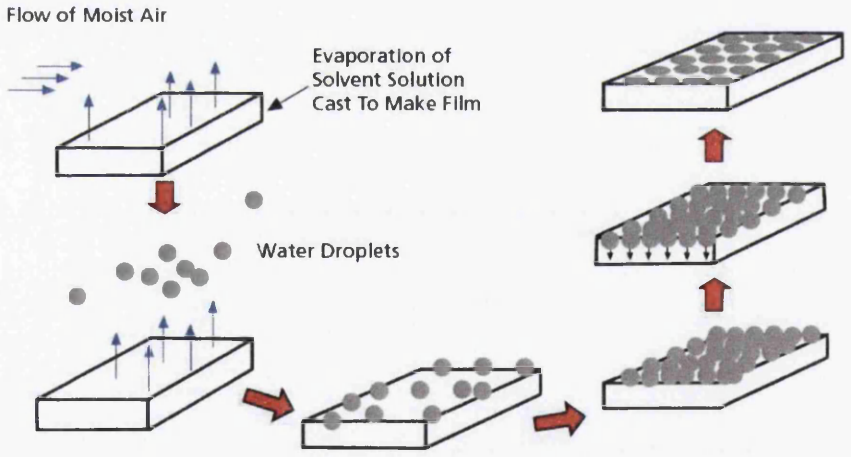

Figure 2.1: Simplified experimental procedure

2.0.1 Where Do The Patterns Come From?

It is clear from substantial evidence in the literature that the patterns originate from the condensation of water vapour, due to evaporative cooling of the liquid solvent [7][15][17]. The exact dynamics for arrangement of the condensed droplets into the observed ordered hexagonal arrays is a topic of discussion at present. However it seems that an essential precursor for the formation of regular arrays is the ability of a particular polymer solvent combination to suppress water droplet coalescence. Observations of the growth process using high speed video microphotography studies were made by Barrow and co-workers [7]. These observations confirm this non-coalescing behaviour in the case of solutions containing monocarboxy-terminated polystyrene ($M_w = 50,000$) and carbon disulphide. The nucleation and subsequent growth of the arrays were visualised and eventually, after about fifty seconds, the formation of close hexagonally packed rafts were observed.

Limaye and co-workers [18] demonstrated that when the surface of formation is volatile the dynamics of formation can be severely altered and descriptions on the process needed some revision with respect to the work of Beysens and co-workers. In order to draw conclusions on how solvent properties affect the growth dynamics, two growth solutions were tested. Both contained about a 5% weight for weight concentration of polystyrene in order to capture the patterns for observation. The solvents used were benzene and

chloroform. Benzene has a density less than that of water and chloroform a greater density. These two fluids were chosen particularly because they have similar values of the enthalpy of vaporization, surface tension and coefficient of viscosity. But they have significantly different values for their vapour pressures. Various volumes of the two solutions were allowed to evaporate in a constant 80% relative humidity atmosphere. The patterns created show great differences

In the case of benzene the average pore size observed in the patterns is much smaller for all solution volumes as compared to chloroform. The researchers suggested that since chloroform has a greater saturation vapour pressure and should evaporate faster, one would expect that the condensation process occurs for a correspondingly lesser time. Therefore one would expect smaller pores than in the case of benzene. The greater average pore size can be explained on the basis that the rate of droplet growth, and therefore coalescence events, must be larger. In order to see whether the liquid properties could account for the proposed greater rate of coalescence events in the case of chloroform, the researchers looked at the hydrodynamic interaction between two water droplets on the surfaces in question. This force is given for two droplets supported on a liquid surface at a distance l as

$$F = \frac{8\pi R^6 \omega^2}{9l\sigma}[1/\rho_s - 1/2 + 0.25(1-\rho^2)^{3/2} - 0.75(1-\rho^2)^{1/2}]^2$$

Where ρ_s is the specific gravity of the liquid, ω is the specific weight, σ

is the liquid-air surface tension and $\rho = r/R$, where r is the apparent drop radius above the surface and R is the drop radius below the surface. Evaluating this force for both liquids, it turns out that the force between water droplets on the chloroform surface is twice that of droplets on the benzene surface. It is concluded that this difference is not significant enough to account for the difference in the pore sizes observed, so it is suggested that other considerations are needed.

The observed differences in the pore sizes in the work of Limaye and coworkers could be accounted for by ideas presented by Srinvasarao *et al* [17] who observed that when solvents are used that have a density less than that of water, the pore array propagates through the film. This explains the pore size difference between films made from benzene and chloroform. Benzene is less dense than water with a density of ($\rho = 0.88 g/cm^3$) so based on the observations of Srinvasarao multi-layered structures could be preserved in the final film. The surface that the researchers imaged would be the top layer of many. Over the time scale of the film formation many layers would have been formed during the time taken for the solvent to evaporate. According to the formation mechanism now being proposed, the droplets levitate above the solution due to thermal gradients that exist between the droplets and the evaporating solvent, resulting from latent heat of evaporation and condensation. Once the surface is totally covered by droplets it is suggested that this

gradient dissipates and the droplets can then sink into the solution. When the surface is then clear the process can start again. The patterns observed by Limaye and co-workers in the case of benzene could be the end result of droplet growth process that started as the subsequent layer sank into the solution, i.e. a correspondingly lesser time than in the case of chloroform, hence the smaller pore sizes observed.

2.0.2 Why Do The Droplets Not Coalesce?

The question remains of why the pores are uniform in size. And why are condensed water droplets observed to display non-coalescing behaviour when creating breath figures using volatile solvent/polymer combinations? Srinivasarao provides two explanations for the non-coalescence. The first explanation is that the evaporating solvent escaping the surface of the solution provides a separating layer between droplets, preventing them from coalescing. The droplets would be prevented from coalescing as long as the interaction time of the droplets (the time in which cohesive forces are affecting the droplet's motion) is less than the time taken for the vapour to escape the layer interstices. This could possibly account for the observations of large regions of coalesced pores on the outer parts of breath figures, where the solvent evaporation should be faster. The second explanation provided by Srinivasarao is justified on the basis that thermo-capillary convection currents

exist between the droplets and the surface. The condensing water droplets are hotter because of the latent heat of condensation, and the solution surface colder because of evaporative cooling; hence the presence of Marangoni convection currents. There is a wealth of material that examines this phenomena [19][20][21]. Monti and co-workers for example show that if a liquid drop is placed in a liquid matrix which is lighter than the drop it can experience a pushing force if there is sufficient temperature gradient between the liquid drop and the matrix due to the Marangoni effect and can even be made to levitate by increasing the temperature gradient further. Numerical modelling has also been presented simulating the pressing of two liquid drops of the same liquid in the presence of thermo-capillary convection [22]. During the experimental situation which this modelling simulates, a temperature difference is imposed between two discs that support liquid drops; they are contained within an air filled environment at ambient temperature. When the temperature difference is set up, Marangoni flows start inside the drops. The spacial distance between drops is then decreased gradually. If the temperature difference is large enough, the droplets do not coalesce. The droplets are then pushed together until a flattening of the contact interface occurs. The temperature difference is then gradually reduced until at some critical temperature coalescence occurs. Numerical modelling of this situation examines the flow fields within the liquid drops and shows that the overall effect of

the induced Marangoni flows is such that a driving action is set up, from the hot drop to the colder drop, which in turn entrains the ambient air towards the contact region. This creates a pressurised air film between the drops, which can prevent the droplet's cohesive forces from causing the droplets to coalesce.

Another explanation for the observed non coalescing behaviour has been proposed by Pitois and Francois. This is based upon the possibility of the formation of solid polymer shields around the water droplets during the formation process [23][24]. It is argued that it is the ability of the polymer to precipitate at the solution-water interface that determines if these 'shields' form and therefore inhibit coalescence. It is also suggested that the immediate precipitation of the polymer is key in the preparation of highly ordered breath figures. It has already been observed that a spherical-shaped polystyrene is needed to obtain high regularity (either star or block-copolymer). Experiments have shown that linear polystyrene hardly precipitates at the solution-water droplet interface, whilst polystyrene stars and polystyrene block copolymers immediately form a solid layer; this seems to indicate that non-coalescence is essential. Stenzel and co-workers formulated a possible proof of this theory by injecting two millemetric solution drops into water and pressing them together. When using PPP/CS_2 solutions, the polymer layer that formed around the droplets was sufficiently strong to pre-

vent coalescence, even when the contact area was close to the droplet radius. However when the same process was repeated with linear polystyrene solutions, the droplets coalesced immediately. A further publication by the same authors [25] presents data from light scattering experiments, which is concluded to indicate the same behavior based on the observed growth laws for droplets. The growth of the droplets is seen to evolve as a power law, with an exponent of 1/3 which indicates a lack of coalescence and indicates non interacting droplet growth.

Yet another explanation for the formation process is provided by Schimomura and co-workers [26]. This group believe that the observed ordering of the pores is a result of the condensed water droplets becoming submerged in the evaporating solvent solution. Forces exerted on the condensed droplets, caused by thermo-capillary effects, are presumed responsible for the observed hexagonal ordering.

It is clear to see then, that there is need for some qualitative evidence regarding the observed non-coalescence. Although researchers provide thorough explanations for their beliefs, at present all are really just valid proposals. It could be that all these effects play a role in the creation of breath figure patterns. In order to really proceed in explaining these theories work is required to predict the onset of some of these effects based on the thermal changes occurring in a particular system. However the balance of available evidence

seems to favour, the theory of polymer shields preventing coalescence.

2.0.3 Film Preparation And Casting

The basic procedure for creating macro-porous materials using the breath figure method is allowing a suitable polymer solvent solution to evaporate in an environment in which moisture is present. There are then two scenarios which distinguish the types of growth carried out; that where a flow is applied, to transport moist air over the evaporating solution[17], and that where a flow is not used but moisture is present[1]. In order to try and create repeatable results the casting conditions must be recorded accurately. The process of formation is not yet completely understood, but there have been experimental reports on some of the variables shown to affect feature size and ordering. Humidity, air flow speed and also the relative weighting of the polymer/solvent solutions affect pore sizes and morphology. There are other variables which could be postulated to play a role in the dynamics of the formation process. For instance since the process described is definitely driven by a thermodynamic change in the system, anything that affects this thermodynamic change will affect the rate of evaporation and subsequent condensation of water from the air. The rate of evaporation of the solvent will be affected by the substrate onto which the solution is deposited. The efficiency of heat transport from the substrate to the solution as it evaporates

will affect the evaporative cooling of the surrounding air and hence the subsequent condensation rate. The substrate material itself is therefore in a sense a casting condition. And also the material on which the substrate rests. If an insulating material is used as a substrate, heat transfer to the evaporative liquid will be lessened, so the liquid and surrounding air should cool to a greater extent and facilitate condensation to a greater extent. However, the greater the extent of the cooling, the lesser the rates of solvent evaporation due to decreasing saturation vapour pressure with temperature and hence, cooling brought about by the evaporation; these changing dynamics will inevitably change the pore size in the final film. This effect is investigated numerically and experimentally in the results sections.

2.0.4 Observed Trends In Growth In Relation To Casting Conditions

Some general observations have been noted about the pore sizes obtained under different casting conditions. It has been noted many times that when a solvent is used for casting which is less dense than water, such as benzene or toluene, multilayered structures can be produced. When using a solvent that is more dense than water, just a single layer can be produced [17]. It was observed that the relative humidity in the casting chamber had to be above 50% [27] to observe a porous film at the end of casting, and a featureless film

with no pores is obtained when casting in a dry atmosphere. It has been noted that increasing airflow speed leads to decreasing pore sizes [17] and that increasing airflow from 30m/min to 300m/min has led to decreasing the pore sizes from 6 μm to 0.5 μm. Also, when changing the concentration of polymer in the initial growth solution, changes in pore sizes have been noted. In general lowering the concentration of polymer leads to increasing pore sizes but lowering too much leads to irregularities. There are many arguments about the nature of the material systems and which properties affect the patterns and pore sizes. Widowski *et al* observed a regular morphology for instance when the relative molecular mass of the polymers used was between 15,000 and 50,000 and the pore size was found to increase with the relative molecular mass.

2.0.5 Materials

Many polymers have shown their compatibility with this process including linear homopolymers [28], rod coil or coil-coil block copolymers [15][27][29][30], star like homopolymers and copolymers [25][31]. Solvents applicable to the process tend to be highly volatile organic solvents, the two most frequently used of which being carbon disulphide and chloroform.

Some authors are of the opinion that the material system used in the creation of the structures is the most important parameter affecting order.

It has been suggested that the interfacial forces between the solvent and water droplets can significantly affect ordering. In an article by a team of researchers in Belgium [32] it is shown that the material 2,2,6,6-tetramethyl-1-piperdinyloxyl (TEMPO) terminated polystyrene can be made into a material capable of creating breath figures when its termination is converted, using p-toluenesulfonic acid, into p-toluenesulfonate piperidinium(TEMPO/PTS) acid salt. This indeed is a clear demonstration of the sensitivity of the process to the material systems involved. Time-of-flight secondary ion-mass-spectrometry is used to image the surface of the produced materials. A high degree of uniformity is noticed in the orientation of the pores, but also a chemical pattern is observed to exist within the material which is proposed to be due to the differences in polarity of the end groups and the polymeric chains. The TEMPO and PTS groups are shown to be mostly confined on the cavity openings in the form of small rings. This seems to show that adding polar end groups can functionalize a material for breath figure imprinting through water micelle formation. This again seems in agreement that the precipitation of the polymer at the droplet interface is essential in order to prevent droplet coalescence.

Apart from the influence of the materials used on the templating dynamics another challenge is apparent; the structural stability of the polymer after casting.

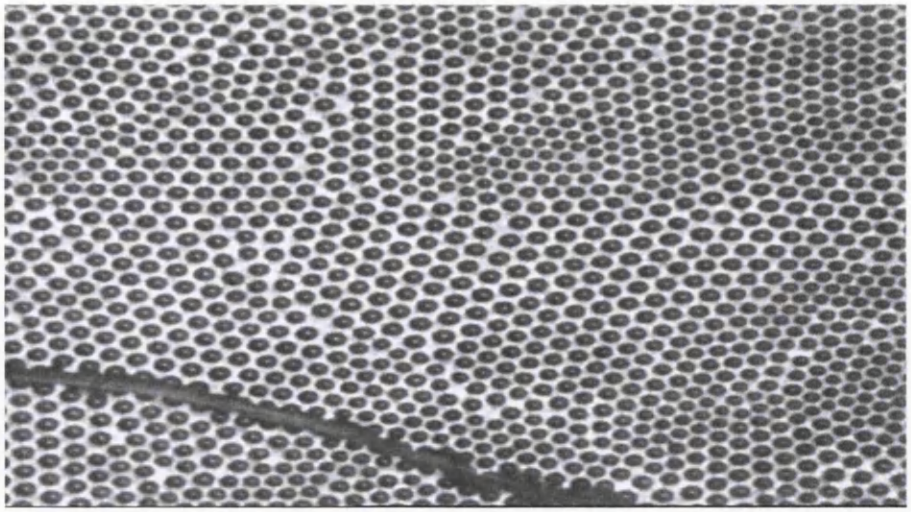

Figure 2.2: Observed cracking

As the porous polymer film is drying after completion of the process cracks often develop (figure 2.2). Developing the perfect material for the process then involves maintaining structural stability whilst not altering the dynamics considerably in a detrimental way. Recently it has been shown that materials can be manufactured which maintain the structural integrity of the structures even when casing onto three dimensional surfaces [33]. Connal and co-workers demonstrate this ability, when using a new polymer material in conjunction with benzene, to contour the breath figure patterns to micro-particles which are also inherent in the casting solution. These particles have a range of shapes such as doughnut, spherical and amorphous shapes.

2.0.6 Decoration And Functionalisation Of Breath Figures

In relation to the decoration of breath figures the most frequently cited work seems to be the work of Boker and co-workers [28]. Here an investigation is made of the self-assembly of CdSe nano-particles on a breath figure substrate. Microscopy studies show that the nano-particles become preferentially gathered around the polymer solution/water droplet interface. After the casting procedure, 5-7nm layers of the nano-particles are observed around the cavities left in the polymer surface. "As can be seen, the size scales and characteristics of the breath figures, do not depend on the presence of the nano-particles and, therefore, the parameters that are key in the pure polymer film preparation, will also be key in the case of the polymer/nanoparticle mixtures. Thus, we may assume that the droplet growth and particle segregation to the resulting liquid-liquid interface, are two processes occurring simultaneously, without significantly influencing each other." This work has great importance since it shows the ability to introduce other substances to the growth solution without significantly influencing the growth itself.

More recently it has been observed [1] that the breath figure moist casting method can be used to assist the formation of $AuNR(PS)_n$ nano-rods. It has been shown that gold nanorods when functionalised with hydrophobic polystyrene arms can self organize into ring structures when incorporated

in an evaporating CH_2CL_2 solution(figure 2.3). The workers show evidence that the hydrophobicity of the polystyrene arms prevents the nonorods from entering condensed water droplets, formed due to evaporative cooling induced condensation from a humid atmosphere. After complete evaporation rings of nanorods are observed templated by the previously condensed water droplets.

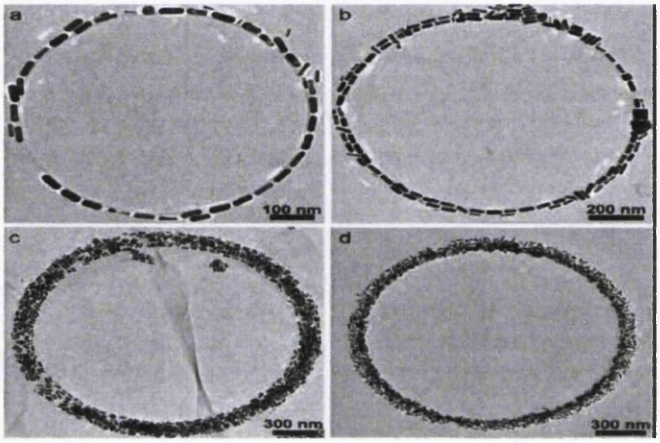

Figure 2.3: Self assembled $AuNR(PS)n$ nano-rods templated by breath figures [1]

2.0.7 Applications

One suggested application of breath figure substrates is the production of photonic band gap materials or PBG materials. PBG is a phrase adopted because of the analogy between the solution of the Schrodinger equation in a material with a periodic electronic potential and the solution of Maxwell's equations in a material with a periodic change in dielectric constant. When solving in the first case one finds that there is a disallowed band of energies

for electrons traversing the material and in the latter, a disallowed band of wavelengths for photons traversing the media. Hence the name photonic band gap materials. The PBG research area has many branches including microwave engineering, quantum optics, the semiconductor industry and laser theory. There are some materials in nature which have a suitable periodic structure to exhibit PBG properties such as parrots wings. Unfortunately these materials do not have a highly enough contrasting dielectric constant throughout their structure [34] to exhibit the associated optical behaviour. Typically the contrast ratio must be greater than a factor of 2. A multi-layer breath figure material could therefore with suitable refractive index contrast and periodicity, serve as a 3-dimensional photonic bandgap structure. Light propagating through the structure in certain directions would encounter a band of disallowed wavelengths. Breath figure templates have in fact already been used indirectly for this purpose [35]. In this work, breath figures are used as a sacrificial mask to create metallic masks in order to structure silicon materials by etching. In this manner the workers were able to create 'silicon cylinders' which they postulate could be used as two dimensional photonic crystals. The workers also demonstrate the applicability experimentally of using breath figure templates to make dichloric filters.

It has been suggested [36] that breath figure structured porous films, because of their narrow pore size distribution, are a suitable media for studying

the effect of surface and pore size on cell adhesion. Tissue engineering methods, whose aim is to replace organs, bone and tissue, predominantly use bio-degradable polymers as the initial scaffold for the development of a new extra cellular matrix (ECM). The scaffold should then be absorbed into the body leaving just the ECM. Different factors are involved in the successful production of these biological materials, such as cell-cell interactions. In current methods scaffolds are normally seeded with cells after their production. However ensuring even transport of the cells throughout the scaffold is difficult. Inclusion of the cells during the scaffold manufacture may improve this transport. In most of the methods currently used to create the scaffold's inclusion of the cells during the scaffold formation process, would be impossible due to the high temperatures needed in production. It has therefore been suggested that the moist casting method presented in this thesis could be a desirable method for creating scaffolds for tissue growth. However it must be noted that the temperature decreases involved in the growth process could also affect cell migration. This is yet another reason why simulation of the thermodynamics is useful.

2.1 Theoretical Treatment And Simulation

There are a variety of publications discussing the growth of liquid droplets on a 2d surface. Two of the most frequently cited in work concerning the growth

of breath figures are the studies of Beysens and Knobler [10] and Meakin and Family [37] so these shall be addressed here. The work of Beysens and Knobler aims to describe the growth of droplets on a surface during early stages of formation via simulation, starting with droplets of the critical radius. That is, droplets with a large enough size such that growth rather than decay is the favourable energetic configuration (nucleation theory critical radii). These droplets are referred to as monomers in the work. The monomers are created on the 2d surface at a constant rate at random locations with the condition that monomers cannot be created at locations on the surface which correspond to the locations of previously condensed droplets. The deposited drops are then allowed to perform a random walk on the surface. This is simulated by moving a droplet of radius ρ a length $\frac{l_0^2}{\rho_i}$ such that its simulated speed on the surface is retarded by its size. When two droplets come into contact they are allowed to coalesce and form a drop whose size is determined by the conservation of the masses of the coalesced droplets. The simulation results show that a well-defined droplet family is brought into existence as the simulation develops, which corresponds to a secondary maxima of a plot of droplet radius vs frequency of occurrence. The other maxima is the radius corresponding to the monomer size, or critical droplet radius. The average droplet size is seen to follow a power law $t^{0.48}$. The surface coverage is also seen to remain low and asymptotically approach a

value of about 0.1 throughout the simulation. A second part of the work presented in this publication is concerned with the growth of an isolated drop which is surrounded by monomers. The monomers are only allowed to grow via coalescence with the isolated drop itself. In this situation a power law of $t^{1/3}$ is observed for the growth of the isolated droplet over time; this $t^{1/3}$ growth rate is a result that has been widely observed in the breath figure experiments. This experimental observation however could be due to the fact that observations are most noted, for times corresponding to when the family of droplets are large enough, such that this mechanism is dominant with respect to the growth of monomers by coalescence, that is when the surface coverage is high and the droplet size is macroscopic.

Meakin and Family [37] present simulations in which droplets increase in size by their coalescence with each other, and also by coalescence with monomers, produced on a two-dimensional substrate, whose rate of production are governed by theories of heterogenous and homogenous nucleation. In the model presented for homogenous nucleation, an assumption is made that droplets can form and grow anywhere in the system. For heterogenous nucleation a fixed number of sites are prescribed, for which droplets can be positioned on deposition. This is meant to simulate the presence of nucleation sites on the substrate. The droplets then grow according to a functional form, which is chosen to simulate the addition of vapour to the condensed

droplets. The functional form is chosen with a form $\frac{dr}{dt}\alpha r^w$ where r is the current droplet size, and w is an arbitrary exponent. This form is chosen to simulate the fact that in a uniform vapour droplets grow at a rate proportional to their area. The droplets then grow according to this functional form and also by coalescence. The results of the simulation in the case of homogenous nucleation show once again the emergence of a family of large droplets and a polydisperse distribution of smaller droplets. The results of the simulations for heterogenous nucleation show only a monodisperse distribution of droplets that grows with time. It is concluded that the homogenous nucleation case is more applicable to the study of vapour deposited thin films. It must also be mentioned that Briscoe and Galvin [38] have developed an analytical solution for the growth of breath figures and the results for the growth of droplets under the analytical solution compare very well with the results of the corresponding simulations. In they're analytical model the authors develop they're model in terms of the mean surface coverage the area based mean diameter and the number density of droplets. Equations are developed utilising a scaling law for the growth of individual droplets found by Beysens and Knobler during experiments. Development of these equations also returns some key features of the system found in experiments such as the equilibrium value of the surface coverage during the intermediate self similar regime.

These theoretical treatments offer much insight into ways of simulating droplet growth mechanics on 2 dimensional substrates, however they are not really applicable as they stand to make quantitative prediction of droplet sizes for vapour deposited thin films grown under differing casting conditions. To do so, some intermediate step is needed which predicts the flux of vapour to the 2d surface dependant on an experimental setup and the global casting conditions. This is yet another motivation for the prediction of rates of condensation under differing experimental setups. Combining these methods could then lead to a quantitative relation between pore size and casting conditions.

Chapter 3

Numerical Modelling Methods

This chapter aims to present an overview of the development process in formulating a numerical model to describe the evapotranspiration dynamics involved in the described moist casting method. Several different schemes were considered in order to model the essential dynamics of the method. The original model considered a stagnant system, with a hypothetical closed container above the evaporating casting solution. This container was then split up into small boxes and the mass rate of flow from each box was calculated via an expression for molecular flux derived from kinetic theory, at this point the model was intended to be semi empirical with the fluxes calculated based on fits to experimental temperature data. Adaptation of this model led to solution of a diffusion equation for the evaporating solvent above the casting solution. The empirical nature of both these models became unsatisfying besides only considering mass transfer in one spacial dimension within this

closed container meant that the container would become saturated with solvent vapour and start to overestimate any resistance to evaporation in this stagnant system. In order to consider a stagnant system successfully three dimensional equations needed to be solved numerically and doing so would have needed better computational resources than available. For this reason these models were scrapped and a more conceptually satisfying model was developed. The original models are not discussed in detail in this thesis in order to avoid any confusion, here we dicuss the model used currently. By including flow in the dynamics of the current model, the governing equations could be solved without need for parallel computing facilities. This model shall now be presented.

The general system that shall be simulated is presented in figure 3.1. This system consists generally of substrate casting solution and humid airflow. The model presented shall describe the interplay between solvent evaporation from the casting solution, applied flow rates of humid air, thermal changes and condensation.

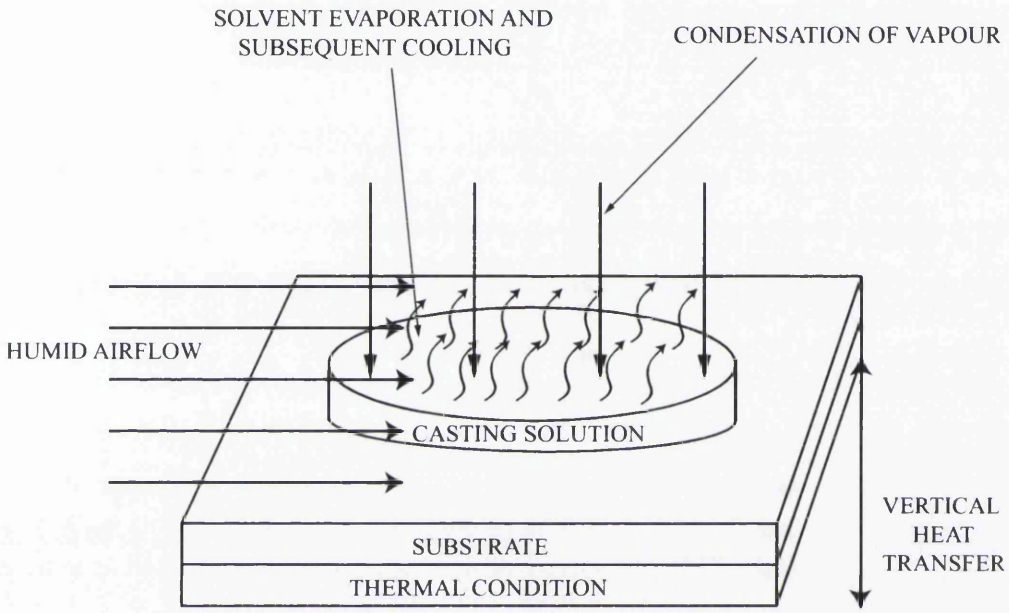

Figure 3.1: Diagrammatic depiction of the physical system

3.1 Evaporation

In order to calculate the condensate deposition rates, firstly the evaporation dynamics of the solvent used in the casting process must be evaluated, such that the energy exchanges which take place as a result can be deduced. In order to do this some assumptions about the system must be made. Firstly it is assumed that the liquid solvent phase is well mixed, i.e. that no concentration gradients exist within the solvent.

The mass in moles of solvent material leaving the interface is then given by a balance equation of the form 3.1 derived from Fick's law

$$\frac{dN_i}{dt} = -A(t)J_i \tag{3.1}$$

Where N_i is the number of moles of component i, A(t) is the interfacial surface area, and J_i is the molar flux of component i. J has units of moles per unit area per unit time. The flux is given by

$$j_i = -D_i \left|\frac{dc_i}{dz}\right|_{lim\ z\to 0} = k^*_{av}(c_i^{int}) \tag{3.2}$$

where C^{int} is the interfacial solvent molar vapour phase concentration and k^*_{av} is the average mass transfer coefficient for the evaporating solution. The concept of the mass transfer coefficient is used as to allow the evaporation flux to be calculated with knowledge of the concentration at just the solution interface. This concept will be discussed in detail later where the average

evaporating mass transfer coefficient is derived.

Substituting equation 3.2 into the mole balance equation

$$\frac{dN_i}{dt} = -Ak^*_{av}(c_i) \tag{3.3}$$

The mass of liquid solvent at each time step is then simply found by iterating the above, using an Euler step

$$M_s(j) = M_s(j-1) + \frac{dN_i}{dt}(j)\Delta t \tag{3.4}$$

In order to calculate the evaporative flux, the interfacial concentration needs to be calculated at each timestep. This can be achieved by making an assumption of local liquid-vapour phase equilibrium at the liquid-vapour interface [39]. This is common assumption observed in the literature concerning evaporative systems [40][39].

3.1.1 Liquid-Vapour Phase Equilibrium

By assuming liquid-vapour equilibrium at the casting solution interface, we are assuming that at the interface the transfer rates from one phase to another are approximately equal for all species in the solution. It is the aim to know the compositions of each phase for all species at temperature T and pressure P at the phase interface. Although at this stage the aim is to calculate rates of evaporation for the solvent, it must be considered that water is also expected

to condense onto the evaporating solvent. Expressions are made in as general a manner as possible, such as to account for deposited liquid water resulting from condensation.

The condition of thermodynamic equilibrium is given by 3.5 expressing the equality of fugacity for both phases [41]

$$f_i^v = f_i^L \tag{3.5}$$

The concept of fugacity is closely related to the equality of chemical potential for phase equilibrium. It is essentially a measure of preference of phase for a species at temperature T and pressure P.

The fugacity of a mixture component in the vapour phase can be related to the vapour composition, expressed in terms of the mole fraction using the fugacity coefficient Φ_i

$$\Phi_i = \frac{f_i^v}{y_i P} \tag{3.6}$$

This can be calculated using an equation of state for the vapour phase or experimental data. For a mixture containing ideal gases, $\Phi_i = 1$. At low pressure it is common to make this assumption.

The fugacity of a mixture component in the liquid phase, can be related to the liquid composition, expressed in terms of the mole fraction using the activity coefficient γ_i

$$\gamma_i = f_i^L / x_i f_i^0 \tag{3.7}$$

Where f_i^0 is the standard state fugacity. This can be chosen arbitrarily, but must be specified in calculations in order to give numerical values of γ_i physical meaning. For most solutions of non-electrolytes, f_i^0 is chosen as the fugacity of pure liquid component at system temperature and pressure.

The fugacity of pure liquid i at temperature T and pressure P is given by

$$f_i^L(T, P, x_i = 1) = P_{vp_i}(T)\Phi_i(T) exp \int_{P_{vp_i}}^{P} \frac{V_i^L(T, P)}{RT} dp \tag{3.8}$$

where P_{vp_i} is the saturation vapour pressure at temperature T, and V_i^L is the ratio of molecular weight to the density.

Substituting these expressions into the initial expression for equality of fugacity in the liquid and vapour phases gives

$$y_i P = \gamma_i x_i P_{vp_i} \mathcal{F}_i \tag{3.9}$$

where, $\mathcal{F}_i = \frac{\Phi_i^s}{\Phi_i} exp \int_{P_{vp_i}}^{P} \frac{V_i^L(T,P)}{RT} dp$

If the total pressure is sufficiently low, a reasonable assumption is that $\mathcal{F}_i = 1$.

Thus the final expression used to describe liquid/vapour equilibrium in the numerical model is

$$y_i P = \gamma_i x_i P_{vp_i} \tag{3.10}$$

In order to calculate the vapour phase composition for the solvent y_i the activity coefficients γ_i must be determined for the mixture. Since liquid-vapour data was not readily available for the water/carbon disulphide system, the UNIFAC solution of groups method is used to estimate the activity coefficients. The UNIFAC method uses existing phase equilibrium data, in order to predict behaviour of systems, for which experimental data is not available. The activity coefficients in mixtures are calculated by analysing interactions between molecular structural groups. These interactions are based upon experimental data for other mixtures, containing the same structural groups. In the UNIFAC method the molecular activity coefficient is formed from two parts. One part due to the differences in molecular size and shape of molecules in the mixture, the 'combinatorial' part. The other part is due to energy interactions and interaction surface areas, the 'residual' part. The equation expressing the above is the UNIQAUC equation

$$ln(\gamma_i) = \overset{combinatorial}{ln\gamma_i^C} + \overset{residual}{\gamma_i^R} \tag{3.11}$$

Where

$$\overset{combinatorial}{ln\gamma_i^C} = ln\frac{\phi_i}{x_i} + \frac{z}{2}q_i ln\frac{\theta_i}{\phi_i} + l_i - \frac{\phi_i}{x_i}\sum_j x_j l_j \tag{3.12}$$

and

$$l = \frac{z}{2}(r_i - q_i) - (r_i - 1) \tag{3.13}$$

Where z=10

$$\theta_i = \frac{q_i x_i}{\sum_j q_j x_j} \tag{3.14}$$

$$\phi_i = \frac{\tau_i x_i}{\sum_j r_j x_j} \tag{3.15}$$

and

$$\tau_{ji} = exp(-\frac{u_{ji} - u_{ii}}{RT}) \tag{3.16}$$

Where x_i is the mole fraction of component i in the mixture. The summations in equation 3.12 are over all mixture components. ϕ_i is the segment fraction, and θ_i is the area fraction. r_i is a pure component property, which is a measure of the molecular Van der Waals force, and q_i is a measure of molecular surface area. These properties can be calculated as the sum of group volume and area parameters R_k and Q_k which are available in chemical data literature [41]. i.e.

$$r_i = \sum_k v_k^{(i)} R_k \tag{3.17}$$

$$q_i = \sum_k v_k^{(i)} Q_k \tag{3.18}$$

Where $v_k^{(i)}$ is the number of groups of type k in molecule i.

The residual component of the activity coefficient is calculated using the solution of groups concept

$$ln\gamma_i^{R\,residual} = \sum_k v_k{}^i (ln\Gamma_k - ln\Gamma_k{}^{(i)}) \tag{3.19}$$

Where Γ_k is the group residual activity coefficient given by

$$ln\Gamma_k = Q_k \left[1 - ln(\sum_m \theta_m \psi_{mk}) - \sum_m \frac{\theta_m \psi_{km}}{\sum_n \theta_n n \psi_{nm}}\right] \tag{3.20}$$

and $\Gamma_k{}^{(i)}$ is the group residual activity coefficient of group k in a reference solution containing only molecules of type i.

θ_m is the area fraction of group m calculated using

$$\theta_m = \frac{Q_m \mathcal{X}_m}{\sum_n Q_n \mathcal{X}_n} \tag{3.21}$$

$\mathcal{X}_n$ is the mole fraction of group m in the mixture. The group interaction parameter ψ_{mn} is given by

$$\psi_{mn} = exp(-\frac{U_{mn} - U_{nm}}{RT}) = exp(-\frac{a_{mn}}{T}) \tag{3.22}$$

U_{mn} is a measure of the energy of interaction between groups m and n. The parameter a_{mn} can be found in chemical database resources and the sums are then performed over all groups.

A summary of the group data for water-carbon disulphide is shown in table 3.1.

Molecule	Main group-no	Sec	V_j^i	R_j	Q_j
CS_2	28	19	1	2.0576	1.656
H_2O	7	17	1	0.920	1.4

Table 3.1: Data, for calculation of activity coefficients using UNIFAC

The calculation for water and CS_2, can be found in the appendix section. We may now proceed to derive an expression for the interface vapour liquid compositions using

$$y_i P = \gamma_i x_i P_{vp_i} \tag{3.23}$$

Equilibrium vapour pressures for the liquid solvent can be calculated using a published function [42] according to the temperature of the interface layer, using

$$P_{vap} = e^{[c1+(\frac{c2}{T_{int}})+c3ln(T_{int})+c4{T_{int}}^{c5}]} \tag{3.24}$$

Substituting the appropriate activity coefficient allows the partial pressure $P_i = \gamma_i x_i P_{vap_i}$ to be calculated; that is with knowledge of the interface tem-

perature. The vapour phase mole fractions, can now be calculated according to

$$y_i = \frac{P_i}{P} \tag{3.25}$$

Then assuming an ideal gas law $PV = NRT$, the definition of a mole fraction $y_i = N_i/N$ and defining the concentration as $C = \frac{N_i}{V}$, the relation $C = \frac{y_i P}{RT}$ can be used to calculate the vapour phase concentration at the interface at all time steps in determining the evaporative flux

$$\frac{dN_i}{dt} = -A(t)k^*({c_i}^{int}) \tag{3.26}$$

As will become evident later, in order to evaluate the mass transfer coefficient k^* the diffusivity of the solvent through the carrier gas D_i must be calculated according to the local temperature and pressure.

3.1.2 Prediction Of Binary Gas Diffusivity

The diffusion coefficients for the vapour phase components are calculated using the method of Fuller *et al* [43]. This method employs an empirical correlation, developed by the experimental analysis of diffusion coefficients, under varying temperature and pressures for a large range of gases. This method uses 'atomic diffusion volumes' which are available in the literature [41]. The correlation is given as

$$D_{ab}(T,P) = \frac{1}{10000}\frac{10^{-3}T^{1.75}(1/m_a + 1/m_b)^{1/2}}{P[(\Sigma V_a)^{1/3} + (\Sigma V_b)^{1/3}]^2} \tag{3.27}$$

Where m_j is the molecular weight of molecule j, P is the pressure in atmospheres, T is the temperature in Kelvin, ΣV_i is the sum of the diffusion volume for component i and D_{ab} is the diffusivity in units of m^2/s. The data needed for this numerical model is given in table 3.2

Molecule	Molecular weight	Diffusion Volume
CS_2	76	50.5
$CHCL_3$	119	76.98
H_2O	18	12.7
air	29	20.1

Table 3.2: Data for calculating binary gas diffusion coefficients

To summarize, so far an expression has been developed for calculating the evaporative flux from the casting solution in order to do this we have assumed a condition of phase equilibrium. This expression contains parameters which are temperature dependant. In order to allow evaluation of these parameters the thermodynamic behavior of the system must now be discussed. In the treatment that follows the aim is to evaluate the temperature at any location at any time in the system depicted in figure 3.1.

3.2 Thermodynamic Treatment

In order to evaluate the temperature distribution at any time in the system, an energy balance is considered for an arbitrary volume element in the system of size $A\Delta x$.

$$\Delta Q_{TOTAL} = \Delta Q_{ENTERING} - \Delta Q_{LEAVING} + \Delta Q_{GENERATED\ OR\ CONVERTED} \tag{3.28}$$

The left hand side of equation 3.28, can be evaluated by considering the amount of heat energy that is required to create any temperature changes which occur inside the volume element in time Δt. Since in this model, there are three materials present (substrate, liquid and vapour), all material parameters are position dependent. The mass of a volume element is therefore given by $M_{element} = A\Delta x\rho(x)$ where $\rho(x)$ is the density of the element dependant on its spacial position. Therefore the energy required to create a temperature difference $u(x, t + \Delta t) - u(x, t)$ is given by

$$\rho(x)c(x)A(x)\Delta x u(x, t + \Delta t) - \rho(x)c(x)A(x)\Delta x u(x, t) \tag{3.29}$$

Where *c(x)* is the specific heat capacity of the material present in the volume element.

The right hand side of equation 3.28 can be formed by considering the transfer of energy due to spacial temperature gradients at the edges of the

element and the inclusion of a source term $Q(x,t)$, defined as the amount of energy produced or converted per unit volume per unit time in an element. The presence of the source term is included to account for the changes in thermal energy lost or gained as a result of the occurrence of phase changes due to evaporation or condensation. This gives the right hand side of equation 3.28 as

$$\Delta t A(-k(x)\frac{\partial U}{\partial x})_{x+\Delta x} - \Delta t A(-k(x)\frac{\partial U}{\partial x})_x + Q(x,t)A\Delta x\Delta t \tag{3.30}$$

Where *k(x)* is the spacially dependent thermal conductivity of the material present in the volume element.

Dividing both sides by $A\Delta x\Delta t\rho(x)c(x)$ the left hand side becomes

$$\frac{u(x,t+\Delta t) - u(x,t)}{\Delta t} \tag{3.31}$$

Which is a finite difference approximation for the partial derivative

$\frac{\partial U}{\partial t}$

the term $\frac{1}{c(x)\rho(x)}(-k(x)\frac{\partial U}{\partial x})_{x+\Delta x} - (-k(x)\frac{\partial U}{\partial x})_x$

is a finite difference approximation for the derivative

$\frac{1}{c(x)\rho(x)}\frac{\partial(k(x)\frac{\partial U}{\partial x})}{\partial x}$

So the final form of the equation describing heat transfer in the system, ignoring time dependant thermal properties, is

$$\frac{\partial U}{\partial t} = \frac{1}{c(x)\rho(x)} \frac{\partial(k(x)\frac{\partial U}{\partial x})}{\partial x} + \frac{Q(x,t)}{c(x)\rho(x)} \tag{3.32}$$

Since the composition changes spacially in the system described above involve sharp changes at the interface between substrate/liquid and liquid/vapour, an additional condition is required at these interfaces. This condition stipulates equality of heat fluxes, from each material, through these interfaces (Jump Balance Condition)[44]. i.e.

$$k_{m_1} \left(\frac{\partial u}{\partial x}\right)_{m_1} = k_{m_2} \left(\frac{\partial u}{\partial x}\right)_{m_2} \tag{3.33}$$

Approximating equation 3.32 as a finite difference expression, using a Crank Nicolson Scheme and denoting the grid spacings in the x and t directions by Δx and Δt and the spacial and temporal nodes by j and n respectively gives

$$x_j = j - 1\Delta x$$

$$t_j = n - 1\Delta t$$

and

$$\frac{U^{n+1}{}_j - U^n{}_j}{\Delta t} = \frac{1}{c^n{}_j \rho^n{}_j} \frac{1}{2} \left\{ \left(\frac{\partial(k(x)\frac{\partial U}{\partial x})}{\partial x}\right)^{n+1}_{i} + \left(\frac{\partial(k(x)\frac{\partial U}{\partial x})}{\partial x}\right)^{n}_{i} \right\} + \frac{Q(x,t)}{c^n{}_j \rho^n{}_j} \tag{3.34}$$

letting $\Gamma = \frac{\Delta t}{2\Delta x^2}$

and

$$K_{j+\frac{1}{2}} = k(x_i + \tfrac{1}{2})$$

$$K_{i-\frac{1}{2}} = k(x_i - \tfrac{1}{2})$$

gives

$$U_j^{n+1} - U^n{}_j =$$
$$\frac{\Gamma}{2c^n{}_j\rho^n{}_j}|(k_{j+\frac{1}{2}}(U_{j+1}^{n+1} - U_j^{n+1})) - k_{j-\frac{1}{2}}(U_j^{n+1} - U_{j-1}^{n+1}) +$$
$$(k_{j+\frac{1}{2}}(U_{j+1}^n - U^n{}_j) - k_{j-\frac{1}{2}}(U_j^n - U_{j-1}^n))| + \Delta t\frac{Q(x,t)}{c^n{}_j\rho^n{}_j} \qquad (3.35)$$

Numerically, the terms $K_{j+\frac{1}{2}}$ and $K_{j-\frac{1}{2}}$ can be evaluated using the average of the values at the spatial nodes before and after. i.e. $K_{j+\frac{1}{2}} = \frac{k(j)+k(j+1)}{2}$.

Taking terms which involve the $(n+1)^{th}$ time step to the left and terms involving the nth to the right gives

$$U_j^{n+1}\left\{1 + \frac{\Gamma}{2c^n{}_j\rho^n{}_j}(K_{i+\frac{1}{2}} + K_{i-\frac{1}{2}})\right\} - \frac{\Gamma}{2c^n{}_j\rho^n{}_j}U^{n+1}{}_{j-1}K_{i-\frac{1}{2}} - \frac{\Gamma}{2c^n{}_j\rho^n{}_j}U^{n+1}{}_{j+1}K_{i+\frac{1}{2}}$$
$$= U^n{}_j\left\{1 - \frac{\Gamma}{2c^n{}_j\rho^n{}_j}(K_{i+\frac{1}{2}} + K_{i-\frac{1}{2}})\right\} + \frac{\Gamma}{2c^n{}_j\rho^n{}_j}U^n{}_jK_{i+\frac{1}{2}} + \frac{\Gamma}{2c^n{}_j\rho^n{}_j}U^n{}_{j+1}K_{i-\frac{1}{2}}$$
$$+\Delta t\frac{Q(x,t)}{c^n{}_j\rho^n{}_j} \qquad (3.36)$$

The extra boundary conditions at the interfaces given in equation 3.33 can be included by expressing them as finite difference approximations

$$k_{m_2}U_{j+1}^{n+1} + k_{m_1}U_{j-1}^{n+1} - U_j^{n+1}(k_{m_1} + k_{m_2}) = 0 \qquad (3.37)$$

The equations described are then solved at each time step, by expressing them in matrix form. This gives a tri-diagonal matrix which must be solved at each time step in order to calculate the system temperature distribution.

$$\begin{pmatrix} e_{left} & 0 & 0 & 0 \\ \Omega(K_{i-\frac{1}{2}}) & 1+\Omega(K_{i+\frac{1}{2}}+K_{i-\frac{1}{2}}) & \Omega(K_{i+\frac{1}{2}}) & 0 \\ 0 & \Omega(K_{i-\frac{1}{2}}) & 1+\Omega(K_{i+\frac{1}{2}}+K_{i-\frac{1}{2}}) & \Omega(K_{i-\frac{1}{2}}) \\ 0 & 0 & 0 & e_{right} \end{pmatrix} \begin{pmatrix} U_1^{n+1} \\ U_2^{n+1} \\ U_3^{n+1} \\ U_4^{n+1} \end{pmatrix} = \begin{pmatrix} \partial_1 \\ \partial_2 \\ \partial_3 \\ \partial_4 \end{pmatrix}$$

Figure 3.2: Crank Nicolson matrix equation for heat transfer equation

Where $\Omega = \frac{\Gamma}{2c^n{}_j\rho^n{}_j}$ and e_{left} and e_{right} are related to the boundary conditions.

The LHS of the matrix equation has size $N \times N + zN$, where N is the number of elements in the spacial grid used and z is the number of interfaces in the domain. In order to avoid writing the whole matrix to memory and improve efficiency the MATLAB sparse organization command is used.

The source term present in the equation $Q(x,t)$ is then related to the evaporation and condensation fluxes and defined by

$$Q(x,t) = 0 \qquad for \qquad 0 \leq x \leq Int_{sub-liq} \tag{3.38}$$

$$Q(x,t) = \frac{(L(T)_{water} M_{water} \frac{dm_{water}}{dt} \Delta t + L(T)_{sol} M_{solvent} \frac{dm_{solvent}}{dt} \Delta t)}{V_{liquid} \Delta t} + \Psi(Tamb - Tint) + (KE_{ave}) \tag{3.39}$$

for

$$\text{for } Int_{sub-liq} \leq x \leq Int_{liq-vap}$$

and

$$Q(x,t) = 0 \qquad for \qquad Int_{liq-vap} \leq x \leq xL \tag{3.40}$$

In the above expressions $\frac{dm_j}{dt}$ denotes the change in the molar quantity of species j and M_j denotes the molar mass of the component j. $L(T)_j$ is the heat of vaporization of species j and V_{liquid} is the volume occupied by the casting solution. Since the latent heat describes the heat required, for the corresponding change in entropy between the initial and final phase $\Delta(s) = s^f - s^i$, the latent heat is strictly temperature dependent. i.e. $\Delta(Q) = L(T) = T(s^f - s^i)$. In this model an empirical correlation which will be described later is used to describe the latent heats. The term KE_{ave} accounts for the translational kinetic energy which must be lost for a moving amount of substance to be brought to rest at the casting solution surface. This is calculated according to the flow rate prescribed. In fact this term is negligible, only contributing about 0.0022 Joules per mole of condensed water for a flow rate of $1ms^{-1}$. The term Ψ is present to account for the loss of internal energy which must be accompanied by the condensation of water vapour on to the casting solution. This term accounts for the fact that in the model, when a molar quantity of water vapour becomes condensed on the surface of our casting solution, it then assumes the same temperature as the casting solution

itself. In order for this to happen it must lose an amount of internal energy in correspondence with this loss of temperature. This energy must therefore be absorbed by the casting solution.

The starting point in working out this loss in internal energy is the fundamental thermodynamic relation, which is a combined statement of the first and second laws of thermodynamics.

$$dU = TdS - PdV \tag{3.41}$$

Where ds can be expressed as

$$dS = \left(\frac{dS}{dT}\,|_V\right) dT + \left(\frac{dS}{dV}\,|_T\right) dV \tag{3.42}$$

substituting this into equation 3.41 gives

$$dU = T\left(\frac{dS}{dT}\,|_V\right) dS + \left[T\left(\frac{dS}{dV}\,|_T\right) - P\right] dV \tag{3.43}$$

Again it is assumed that the vapour is an ideal gas such that the term on the right vanishes. $T\left(\frac{dS}{dT}\,|_V\right) dT$ is the specific heat capacity at constant volume C_v. This then gives

$$dU = C_v dt = C_v(T_{bulk} - T_{int}) \tag{3.44}$$

Or for a specific molar quantity of material $dU = \Delta M \widetilde{C_v}(T_{bulk} - T_{int})$ where $\widetilde{C_v}$ is the molar specific heat capacity and ΔM is the condensed or

evaporated mass in mols. This energy is then distributed through the volume of the casting solution to calculate the term Ψ in the source term.

Using the above method the spacial and temporal temperature distributions can be calculated in numerous situations, by prescribing different material properties thicknesses and boundary conditions. For example, perfect thermal contact at ambient temperature assuming a constant heat source at the bottom boundary. Or a constant heat sink at the bottom boundary $T_{bound} < T_{amb}$. These scenarios are depicted in figures 3.3 and 3.4.

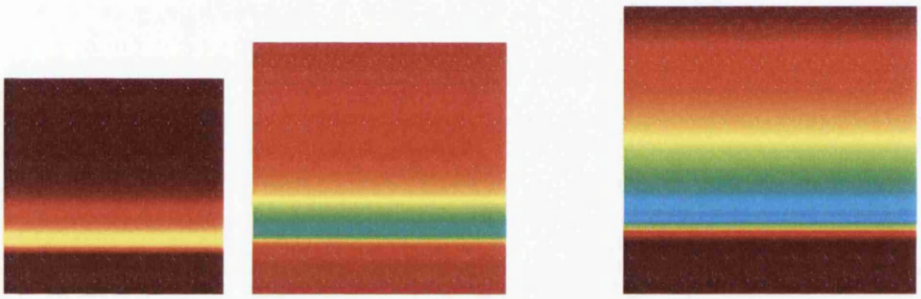

(a) t=1T (b) t=2T (c) t=3T

Figure 3.3: Contrast enhanced depiction of the spacial temperature profiles close to the evaporating interface for three arbitrary times after solution deposition with a perfect thermal contact boundary condition beneath the substrate maintained at ambient temperature and perfect insulation at the top of the chamber

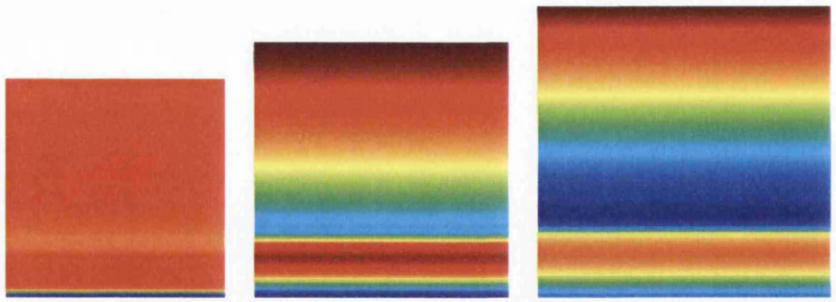

(a) t=1T (b) t=2T (c) t=3T

Figure 3.4: Contrast enhanced depiction of the spacial temperature profiles close to the evaporating interface for three arbitrary times after solution deposition with a perfect thermal contact boundary condition beneath the substrate, maintained below ambient temperature and perfect insulation at the top of the chamber

Figures 3.3 and 3.4 represent the general thermal system depicted in figure (3.5) the colours in the diagrams are representative of the temperature in the system, the general colour scale is also given. Direct application of a variety of these boundary conditions, then allows direct simulation of some of the experimental situations and possibilities that can be used for creation of breath figures materials. This then allows the spacial and temporal temperature distribution to be calculated which allows application to the mass transfer part of this work (figure 3.6).

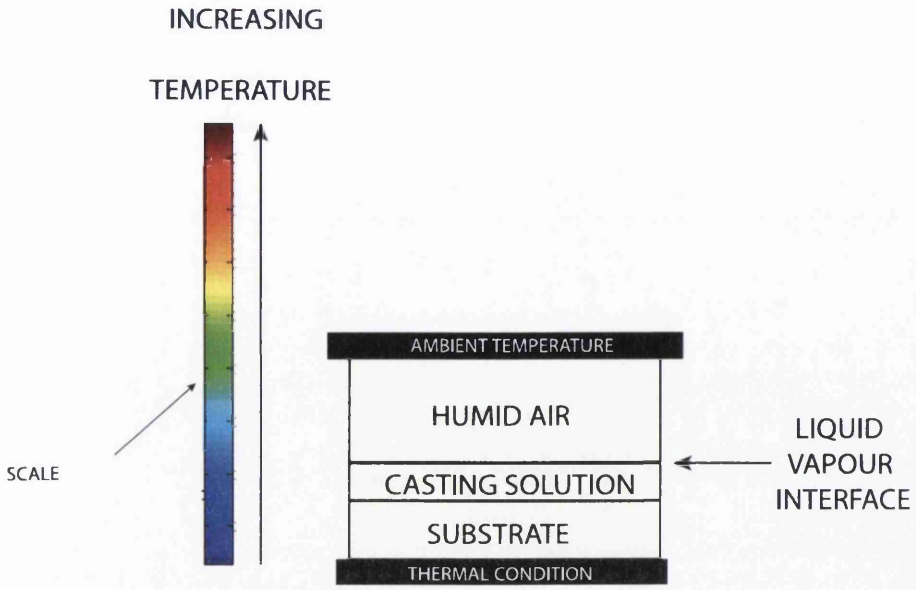

Figure 3.5: Pictorial representation of thermal system

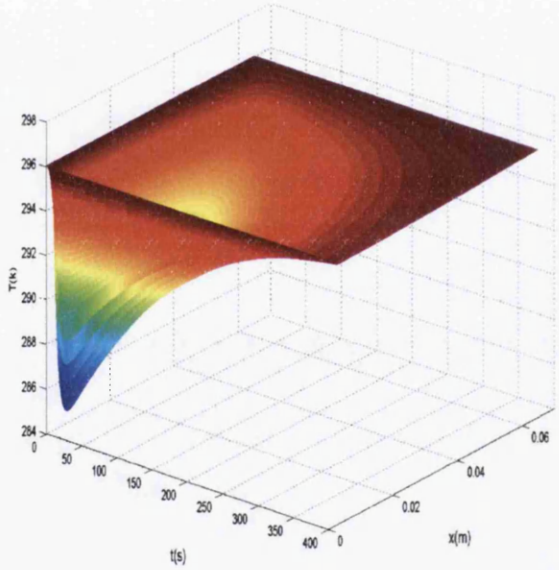

Figure 3.6: Spacial and temporal temperature distribution

3.2.1 Thermal Properties

The energy equation presented does not take into account temporal changes in thermal properties. Even so the thermal properties were initially set dependent on the ambient temperature.

For the liquid solvent phase an equation of the form

$$C_p = c1 + c2T + c3T^2 + c4T^3 + c5T^4 \tag{3.45}$$

was used to describe the specific heat capacity at a given temperature taken from table 2-196 in Perry's chemical engineering handbook; the parameters for the equation are summarized in table 3.3

Liquid	C1	C2	C3	C4	C5
CS_2	8.54×10^4	-1.2200×10^2	5.6650×10^{-1}	-1.4520×10^{-3}	2.0080×10^{-6}
$CHCL_3$	1.2485×10^5	-1.6634×10^2	4.3209×10^{-1}	0	0

Table 3.3: Data for calculating temperature dependent specific heat capacity

For the solvent liquid densities the modified Rackett equation was used

$$\rho(T) = \frac{\frac{P_c}{RT_c}}{ZRA(1 + [1 - \frac{T}{T_c}]^{\frac{2}{7}})} \tag{3.46}$$

which is summarized in Perry's chemical engineering handbook [42] in the form

$$\rho(T) = \frac{C_1}{C_2[1 + (1 - \frac{T}{C3})^{c4}]} \tag{3.47}$$

to be used with the parameters given in table 3.4

Liquid	C1	C2	C3	C4
CS_2	1.7968	0.28749	522	0.3226
$CHCL_3$	1.0841	0.2581	536.4	0.2741

Table 3.4: Data for calculating temperature dependent density

For calculating saturation vapour pressures, the equation

$$P_{vap} = exp[C1 + (\frac{C2}{T}) + C3 \times ln(T) + C4 \times T^{C5}] \tag{3.48}$$

was used with parameters given in table 3.5

Liquid	C1	C2	C3	C4	C5
CS_2	67.14	−4820.4	−7.5303	9.1695×10^{-3}	1
H_2O	73.649	−7258	−7.3037	4.1653×10^{-6}	2
$CHCL_3$	146.43	−7792.3	−20.614	2.4578×10^{-2}	1

Table 3.5: Data for calculating saturation vapour pressures

The function used for evaluating the latent heats for given temperatures is [42]

$$L(T) = \frac{\frac{1}{M_{mol}}}{1000}(C1(1 - \frac{T}{T_c})^{C2+C3\frac{T}{T_c}+C4\frac{T}{T_c}^2}) \tag{3.49}$$

Where $L(T)$ is the heat required for the relevant phase change, in units of Jkg^{-1}, M_{mol} is the molar mass of the species undergoing the phase change expressed in kg. T_c is the critical temperature and T is the temperature that the phase change is occurring at. The parameters are summarised in table 3.6.

Species	C1	C2	C3	C4	T_c
CS_2	3.4960×10^7	0.2986	0	0	552
H_2O	5.2053×10^7	0.3199	−0.212	0.25795	647.13
$CHCL_3$	4.1850×10^7	0.3584	0	0	536.4

Table 3.6: Data for calculating temperature dependant latent heat

This far we can calculate the dynamics of evaporation dependent on thermal changes in the liquid. The temperature changes in the system can now be evaluated. The next logical step in the formulation of the model is to calculate the rate of condensation dependent on the temperature distribution in the system.

3.2.2 Calculating Condensation Flux

Now that the rate of solvent evaporation and also the temperature distribution in the system can be determined a way of calculating the amount of any deposited condensate is considered. Figure 3.7 shows a pictorial representation of the physical system.

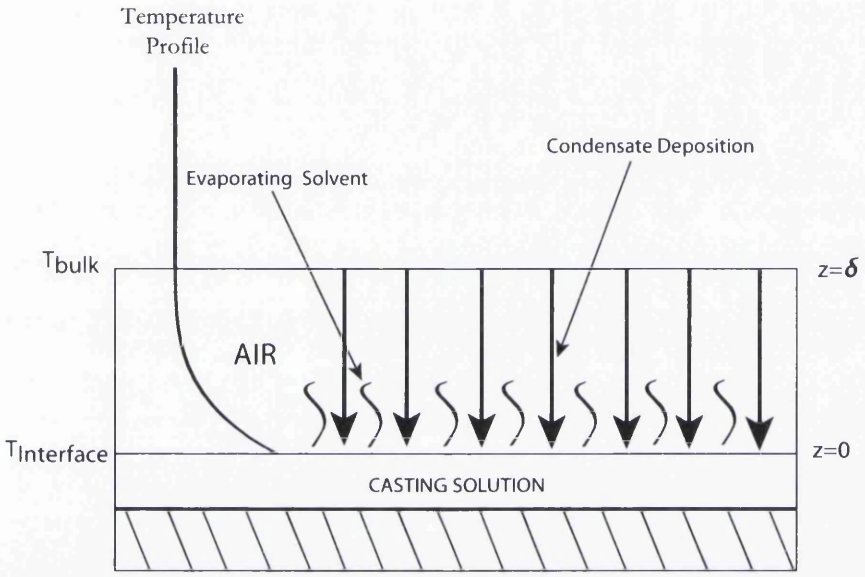

Figure 3.7: Condensation model diagram

A relationship describing the diffusion of each component is provided by considering the Maxwell Stefan equations for multiple species. The Maxwell Stefan equations are used so that the treatment in this thesis allows adaptability to future studies which will consider frictional effects between the evaporating solvent and water vapour created due to simultaneous evaporation of the casting solution solvent and condensation of water vapour manifested by

interaction between species.[1]

For the water vapour in the system the mole fraction gradient in the vertical coordinate with reference to the casting solution interface is given by

$$\frac{dx_w}{dz} = \frac{x_w x_s}{D_{ws}}(V_w - V_s) + \frac{x_w x_a}{D_{wc}}(V_w - V_a) \tag{3.50}$$

Where z is vertical position and D_{xy} is the diffusion coefficient for species x into species y. Subscript w represents water vapour, s solvent and a air. The air is considered as non-condensible and therefore having zero flux with respect to the vertical coordinate in vicinity of the surface so V_a is equated to zero. In this work any frictional effect due to the net flow of solvent produced by evaporation on the condensation flux is neglected, so V_s is also equated to zero.

The equations expressing the mole fraction gradients of non condensing-species in terms of the water vapor flux are given by

$$\frac{dx_s}{dz} = \frac{x_s x_w}{D_{ws}}(-V_w) \tag{3.51}$$

and

$$\frac{dx_a}{dz} = \frac{x_a x_w}{D_{wa}}(-V_w) \tag{3.52}$$

[1]The numerical simulations to which this thesis describes do not directly consider frictional effects between the evaporative and condensing fluxes

The negative signs for the water vapour flux are present because flux towards the casting solution is negative when regarding the positive z-axis as away from the solution. So the expressions for the average mole velocity of the condensing water vapour in terms of the non condensing mole fraction gradients are

$$V_{mol} = x_w V_w = -\frac{D_{ws}}{x_s}\frac{dx_s}{dy} \tag{3.53}$$

and

$$V_{mol} = x_w v_w = -\frac{D_{wa}}{x_a}\frac{dx_a}{dy} \tag{3.54}$$

or in general

$$V_{mol} = x_w v_w = -\frac{D_{wn}}{x_n}\frac{dx_n}{dy} \tag{3.55}$$

Integrating this equation between the liquid-vapour interface and some thickness δ gives

$$\int_0^{\delta} V_{mol} = -\int_0^{\delta} \frac{D_{wn}}{x_n}\frac{dx_n}{dy}dy \tag{3.56}$$

It should be mentioned that in this model the phase interface is placed at the top of the casting solution for ease of calculation. Thus it is assumed that there is jump from liquid to vapour phase, it is the temperature at this transition point on which the calculations of mass transfer to the liquid

water phase are based. In reality there may not be a discrete transition from liquid to vapour and a so called transition layer may exist where the proportions of the phases are mixed. It is extremely difficult to measure what the prevailing conditions are in this region experimentally. The prevailing conditions depend on surface chemistry, hydrodynamics and diffusion in the region. Some generalizations can be made but quantification is difficult in such situations. When observing the casting process regions at the surface display violent activity, which inevitably lead to an enhancement of mass and heat transfer rates with respect to equations based on stagnation of the liquid phase. Also as the proportion of the polymer in the casting solution rises, this material could get transported to the surface decelerating evaporation. A study of this behaviour is outside the scope of the present study and the present method is continued.

$$V_{mol}\delta = -\int_{y_{int}}^{y_\delta} \frac{D_{wn}}{x_n} dx_n \tag{3.57}$$

$$V_{mol} = -\frac{1}{\delta} D_{wn} \left[ln(x_n)\right]_{x_{int}}^{x_\delta} \tag{3.58}$$

so

$$V_{mol} = -\frac{1}{\delta} D_{wn} \left[ln(x_{n,\delta} - ln(x_{n,int}))\right] = -(\frac{1}{\delta}) D_{wn} ln(\frac{x_{n,\delta}}{x_{n,int}}) \tag{3.59}$$

defining

$x_{n,\delta} = x_{n,bulk}$

and

$$x_{n,ave} = \frac{x_{n,bulk} - x_{n,int}}{ln(\frac{x_{n,bulk}}{x_{n,int}})} \tag{3.60}$$

then

$$V_{mol} = -\frac{1}{\delta} D_{wn} \frac{x_{n,bulk} - x_{n,int}}{x_{n,ave}} \tag{3.61}$$

This is an equation therefore representing the average condensation flux, in terms of mole fractions for each non-condensible species.

For the solvent

$$V_{mol} x_{s,ave} = -\frac{1}{\delta} D_{ws} (x_{s,bulk} - x_{s,int}) \tag{3.62}$$

and for the air

$$V_{mol} x_{a,ave} = -\frac{1}{\delta} D_{wa} (x_{a,bulk} - x_{a,int}) \tag{3.63}$$

Summing these equations gives

$$V_{mol} x_{s,ave} + V_{mol} x_{a,ave} = -\frac{1}{\delta} (D_{ws} x_{s,bulk} - x_{s,int}) - \frac{1}{\delta} (D_{wa} x_{a,bulk} - x_{a,int}) \tag{3.64}$$

and defining that the sum of mol fractions of non condensing species at edge of the thickness δ as $x_{g,bulk}$ where;

$$x_{g,bulk} = \sum_{N}^{j=1} x_{j,bulk} \tag{3.65}$$

and at the interface using:[2]

*

$$x_{g,int} = \sum_{N}^{j=1} x_{j,int} = 1 - \frac{P_v(T_{int})}{P_{amb}} \tag{3.66}$$

$$V_{mol}(x_{s,ave} + x_{a,ave}) = -\frac{1}{\delta}\left\{\sum_{N}^{j=1} D_{wj}(x_{j,bulk} - x_{j,int})\right\} \tag{3.67}$$

Noting the definitions above, this gives the final expression for the condensation flux as

$$V_{mol} = -\frac{1}{\delta}\left[\frac{x_{g,ave}}{\sum_{N}^{j=1}\frac{x_{j,ave}}{D_{wj}}}\right]\frac{x_{g,bulk} - x_{g,int}}{x_{g,ave}} \tag{3.68}$$

This equation can also be expressed using saturation vapour pressures via equation 3.66. Inputting again $x_{n,ave}$

$$V_{mol} = \frac{1}{\delta}\left[\frac{x_{g,ave}}{\sum_{N}^{j=1}\frac{x_{j,ave}}{D_{wj}}}\right] ln\left(\frac{1 - \frac{P_{v,int}}{P_{amb}}}{x_{g,bulk}}\right) \tag{3.69}$$

the thickness δ is ascribed by assuming that the air concentration becomes that of the bulk at the same distance as the temperature becomes that of

[2]*It is noted here that equation 3.66 assumes a condition of phase equilibrium at the position of the interface and therefore in doing so it is also assumed that any positive water vapour flux that reaches the surface becomes liquid water. This assumption is dealt with shortly.

the bulk. How this distance is prescribed is explained shortly. In order to express V_{mol} as a mass flux, the expression must be multiplied by a molar concentration. In this work the molar concentration used is based on the absolute humidity in the air flow used in the growth process. The expression for the average mole velocity is then multiplied by this concentration and also the molar mass, to give a mass flux in units of kgm^2s^{-1}, this flux is then multiplied by the area of the film to give a quantity of mass deposited per second. In order to then evaluate the amount of water present at a given time the mass balance

$$M_w = \frac{dw_{cond}}{dt}\Delta t + \frac{dw_{evap}}{dt}\Delta t \tag{3.70}$$

is evaluated

$\frac{dw_{evap}}{dt}$ at present is only initiated when the solvent has fully evaporated. We allow the deposited condensate to evaporate as if the experiment has finished and dry air is blown over the sample.

The equivalent vapour flux equation for one non condensing species is

$$V_{mol} = \frac{D_{g,w}}{\delta} ln\left(\left[\frac{x_{g,bulk}}{x_{g,bulk}}\right]\right) \tag{3.71}$$

Comparing this to the general equation shows that when considering more than one non-condensing species an effective diffusivity can be identified as

$$D_{eff} = \left[\frac{x_{g,ave}}{\sum_{N}^{j=1} \frac{x_{j,ave}}{D_{wj}}} \right] \tag{3.72}$$

To evaluate this effective diffusivity, the binary gas diffusion coefficients for the individual species must also be known;

Using once again the method of Fuller *et al*

$$D_{ab}(T,P) = \frac{10^{-3} T^{1.75} (\frac{1}{M_a} + \frac{1}{M_b})^{\frac{1}{2}}}{P_a mb[(\sum V_a)^{\frac{1}{3}} + (\sum V - b)^{\frac{1}{3}}]^2} \tag{3.73}$$

The mole fractions of the individual non-condensing species at the interface, which are required in calculating $x_{j,ave}$ and for calculating the effective diffusivity, can be calculated when only considering air and solvent as non-condensable, by simply estimating the mole fraction of air at the interface using equation 3.66. In the bulk the non-condensing species mole fractions can be estimated according to the bulk absolute humidity and an ideal gas law.

That is, the molar concentration of air in the bulk is given as a function of ambient temperature by

$$C_{air} = \frac{N}{V} = \frac{P_{amb}}{RT_{amb}} \tag{3.74}$$

The molar concentration of water in the vapour phase in the bulk is given by the absolute humidity multiplied by the molar mass. Assuming equal mixing in the bulk then gives the air mole fraction as

$$x_{air,bulk} = \frac{C_{air}}{C_{air} + ABS \times M_{water}} \tag{3.75}$$

Where ABS is the absolute humidity of the input humid air and M_{water} is the molar mass of water.

This method for calculating the effective diffusivity considers just one carrier gas for the condensable vapour. For completeness, in order to make this method applicable to scenarios involving more than one carrier gas a method derived by Peterson can be employed [45].

This method, estimates the total non-condensable mole fraction at the interface $x_{g,int}$ using equation 3.66. Then, with knowledge of the mole fractions of the carrier gas in the bulk, initial estimates for the individual non-condensable carrier gas mole fractions can be obtained by assuming the same relative proportions between the interface and the bulk, as the whole of the carrier gas mixture. An initial estimate is therefore given by

$$x'_{j,int} = x_{j,bulk} \frac{x_{g,int}}{x_{g,bulk}} \tag{3.76}$$

This now allows an initial estimate for the effective diffusivity D'_{eff} via equation 3.72

Combining two of the previously derived expressions for the condensation flux

$$V_{mol} = -\frac{1}{\delta} D_{wn} \left[ln(x_{n,\delta} - ln(x_{n,int})) \right] = (\frac{1}{\delta}) D_{wn} ln(\frac{x_{n,\delta}}{x_{n,int}}) \tag{3.77}$$

and

$$V_{mol} = -\frac{1}{\delta} \left[\frac{x_{g,ave}}{\sum_N^{j=1} \frac{x_{j,ave}}{D_{wj}}} \right] \frac{x_{g,bulk} - x_{g,int}}{x_{g,ave}} \tag{3.78}$$

gives an equation

$$x''_{j,int} = exp \left[ln(x'_{j,bulk}) - \frac{D'_{eff}}{D_{jv}} \frac{x_{gb} - x_{gi}}{x_{g,ave}} \right] \tag{3.79}$$

Which can be used to gain a secondary estimate of $x_{j,int}$ for the non-condensing components. Apart from the evaporating solvent vapour phase concentration at the interface which is calculated from the phase equilibria relations. In order to calculate the effective diffusivity, the values of the secondary estimates for the interface mole fractions $x''_{j,int}$, are then normalized such as to sum to the total non condensing species mol fraction at the interface $x_{g,i}$

$$x'_{j,int} = x''_{j,int} \frac{x_{g,i}}{\sum_n^{j=1} x_{j,int}} \tag{3.80}$$

and give a new estimate for each mol fraction at the interface $x'_{j,int}$. This allows another estimate of the effective diffusivity. This procedure is then repeated until the effective diffusivity converges.

In order to avoid the constant saturation assumption which was mentioned previously, and is inherent in equation 3.66, an easy adaptation can be made to only initiate a vapour flux by diffusion when the interfacial temperature becomes sufficient to create a saturation condition i.e. $T_{int} \leq T_{crit}$.

This condition is characterized by the equation

$$\rho_{sat}(T_c) = \rho_{actual} \tag{3.81}$$

Where $\rho_{sat}(T_c)$ is the saturation vapour density at the critical temperature, and ρ_{actual} is the actual vapour density.

The above equation must be solved in order to calculate T_c. The actual vapour density can be directly calculated from the relative humidity in the input humid air and initial ambient temperature. The saturation vapour density can be calculated directly from the saturation vapour pressure using the ideal gas law.

$$P_{sat}(T_c)V = \frac{M}{m}RT_c \tag{3.82}$$

where

$\frac{M}{V} = \rho_{sat}$

so

$$\rho_{sat} = \frac{P_{sat}(T_c)}{RT_c} \tag{3.83}$$

Substituting into equation 3.81

$$\frac{P_{sat}(T_c)}{RT_c} = \rho_{actual} \tag{3.84}$$

The saturation vapour pressure as a function of temperature, can be calculated using

$$P_{vap} = e^{[C1+(\frac{C2}{T_c})+C3\times ln(T_c)+C4\times T_c^{C5}]} \tag{3.85}$$

with the relevant parameters. This gives an equation of the form:

$$\frac{e^{[C1+(\frac{C2}{T_c})+C3\times ln(T_c)+C4\times T_c^{C5}]}}{RT_c} = \rho_{actual} \tag{3.86}$$

which is solved for T_c at each time step using a root finding algorithm. If the interface temperature then drops below the calculated value of T_c the vapour flux is then initiated and all vapour passing onto the surface is then assumed to liquify.

3.2.3 Inclusion Of A Polymer

At present the role of the polymer in the process is only included in a basic manner in the numerical model. The mass of polymer present in the solution droplet is calculated via the assumption that sufficiently low concentrations of polymer are used, such that the density of the solution does not depart significantly from that of the solvent. The mass of the droplet can be calculated

via

$$M_{drop} = \rho_{solvent} V_{drop} \tag{3.87}$$

The molar quantity of polymer can then be estimated, using the knowledge of the weight for weight concentration of the polymer in the casting solution

.

$$\frac{C_{polymer} M_{drop}}{M_{polymer}} = n_{polymer} \tag{3.88}$$

where $C_{polymer}$ is the weight for weight concentration of polymer in the casting solution $M_{polymer}$, is the molar mass of the polymer, and $n_{polymer}$ is the molar quantity of polymer in the deposited drop. The inclusion of the polymer only serves to lower the liquid phase mole fraction of the solvent and in doing so only has an effect on the evaporation rate via equation 3.23. The polymer thus only has an indirect effect on the thermodynamics, that is the thermal properties of the polymer are not inherent in the numerical scheme.

When including a polymer in the casting solutions experimentally, it was noted that the solution area does not shrink as in the case of pure solvents. This simplifies matters considerably. A constant surface area is then used in the equation describing the evaporation flux instead of an experimentally determined time dependent surface area. This surface area at present though still has to be calculated via experimental methods. A program written to

analyse areas of objects in video footage however made this an easy task. (See experimental methods)

3.2.4 Inclusion Of Flow And The Derivation Of Flow Dependant Mass Transfer Coefficients

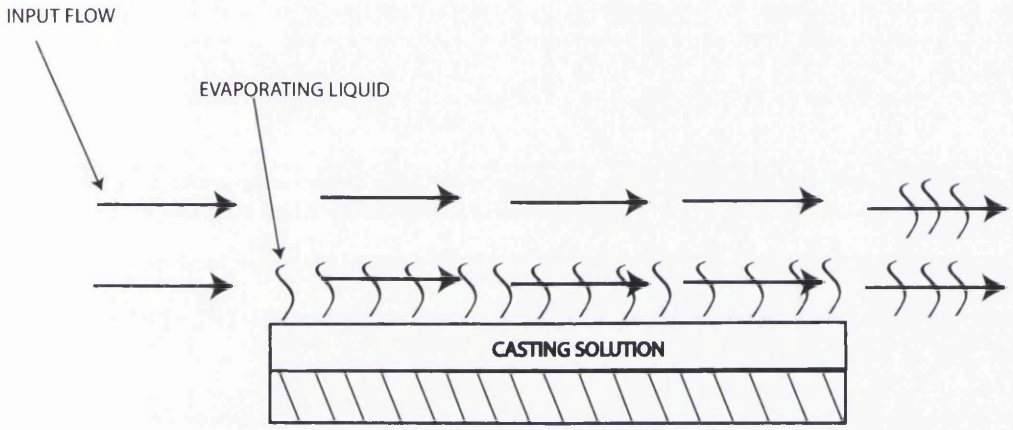

Figure 3.8: Diagrammatic depiction of flow assisted evaporation

In the vast majority of the work describing the production of breath figures, a flow of moist air is past over a substrate, onto which a polymer solvent solution is deposited. This flow essentially helps to clear away any evaporated solvent over the casting solution allowing for increased rates of evaporation (figure 3.8). In order to address the influence of this process on the production dynamics mass transfer is considered in a control volume with the presence of flow $V_{stream} = (u, v, w)$ see figure 3.9.

If liquid solvent vapour is present in this control volume how could we

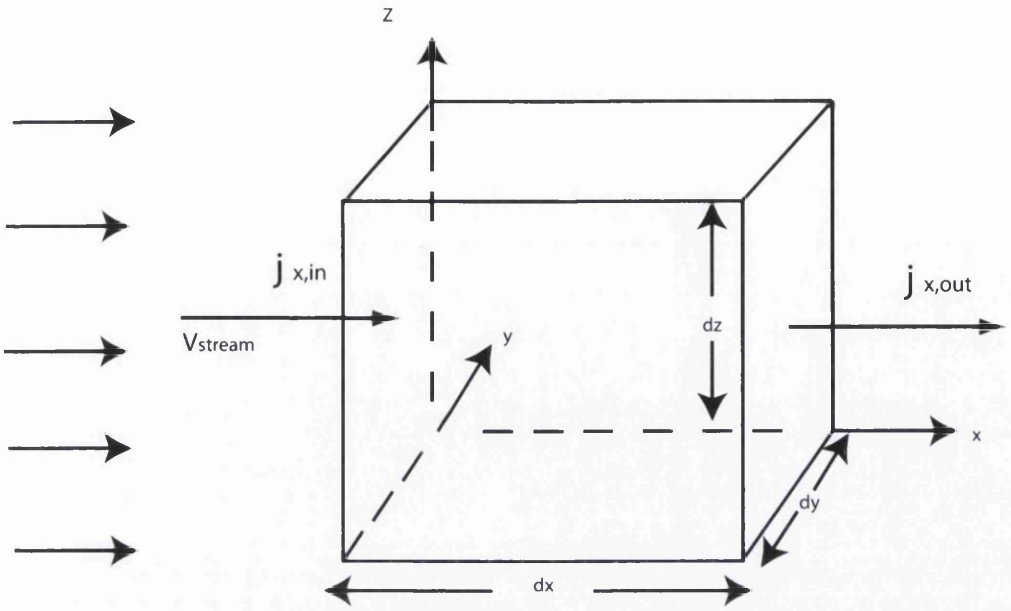

Figure 3.9: Diagrammatic representation of volume element for mass transfer

describe the net change in concentration due to both diffusive and forced convective influences (i.e. the flow of humid air). Each molecule in the volume should move a distance udt in the x direction due to the flow in this direction in a time dt if we assume the humid air flow is incompressible. The total mass of molecules therefore passing through the volume in unit time is given by the concentration multiplied by the effective volume that passes through the volume element. This volume is given by the area $dydz$ multiplied by the distance travelled in the x axis in unit time, which is the velocity in the x direction. The flux through the side of the volume due to the flow is therefore Cu. Considering that diffusion is then a separate independent

process the total movement of molecules is then given by adding the two effects

$$J_x = uC - D\frac{\delta C}{\delta x} \tag{3.89}$$

Using this principle to express a mass balance for the element as

$$\frac{dM}{dt} = \sum \frac{dm}{dt}_{in} - \sum \frac{dm}{dt}_{out} \tag{3.90}$$

in the x direction

$$\frac{\partial m}{dt}|_{\partial x} = (uC - D_{ab}\frac{\partial C}{\partial x})|_x \partial y \partial z - (uC - D_{ab}\frac{\partial C}{\partial x})|_{x+\partial x} \partial y \partial z \tag{3.91}$$

the flux term $((uC)|_x - (uC)|_{x+\partial x})\partial y \partial z$ is equivalent to a finite difference approximation for the derivative $-\frac{\partial uC}{\partial x}\partial x \partial y \partial z$

and the rest of the expression

$((-D\frac{\partial C}{\partial x})|_x - (-D\frac{\partial C}{\partial x})|_{x+\partial x})\partial y \partial z$ is a finite difference approximation of the derivative $D\frac{\partial^2 C}{\partial x^2}\partial x \partial y \partial z$

This gives

$$\frac{\partial m}{dt}|_x = -\frac{\partial uC}{\partial x}\partial x \partial y \partial z + D\frac{\partial^2 C}{\partial x^2}\partial x \partial y \partial z \tag{3.92}$$

and in the y and z directions similar expressions are obtained. Substituting these expressions back into the initial mass balance, and defining the mass in the element as, $M = C\partial x \partial y \partial z$, gives an equation

$$\frac{\partial C}{dt} + \nabla.(uC) = D\nabla^2 C \tag{3.93}$$

In the breath figure moist casting method, humid air is passed over the casting solution. This flow is considered in this work to be one dimensional and is expressed as U_x. From this assumption follows another; it is considered that any advective transport in the **x**-direction is far greater than diffusional transport, i.e. $u_x >> D$. Diffusive transport is then only assumed to occur in the z direction, which in this coordinate system is perpendicular to the plane of the casting solution interface and the flow. The purpose of using this approach is to derive a steady state average mass transfer coefficient to describe the evaporation of the liquid solvent in the casting solution. The time dependant term in equation 3.93 is equated to zero and we search for a steady state solution to the simpler partial differential equation

$$U_x \frac{\partial Cx, z}{\partial x} = D_z \frac{\partial^2 C(x, z)}{\partial z^2} \tag{3.94}$$

stipulating boundary conditions

$$C(0, z) = 0 \tag{3.95}$$

That is, no solvent airborne in the region above the start of casting solution and

$$C(x,0) = C_{int} \tag{3.96}$$

There is a constant vapour concentration at the casting solution surface.

Dividing equation 3.94 by D_z, the laplace transform of the RHS is then given by

$$\int_0^\infty e^{-px}\frac{\partial^2 C(x,z)}{\partial z^2} = \frac{\partial}{\partial z^2}\int_0^\infty C(x,z)e^{-px}dx = \frac{\partial^2 \tilde{C}}{\partial z^2} \tag{3.97}$$

where

$\tilde{C} = \int_0^\infty C(x,z)e^{-px}$ is the laplace transform of $C(x,z)$

the transform of the LHS is given by

$$\frac{U}{D_z}\int_0^\infty \frac{\partial C(x,z)}{\partial x}e^{-px} \tag{3.98}$$

performing an integration by parts then gives

$$\frac{U}{D_z}\left[(C(x,z)e^{-px})\,|_0^\infty - p\int_0^\infty C(x,z)e^{-px}dx\right] \tag{3.99}$$

Noting the boundary condition imposed on the concentration C(0,z)=0 then gives the whole of the above expression as $-p\frac{U}{D_z}\tilde{C}$

The transform of the original equation is then

$$\frac{\partial^2 \tilde{C}}{\partial z^2} - p\frac{U}{D_z}\tilde{C} = 0 \tag{3.100}$$

The transform of the boundary condition $C(x,0) = C_{int}$ is given by

$$C(\tilde{0},z) = \int_0^\infty C_{int} e^{-px} dx = \frac{-C_{int}}{p} e^{-px}|_0^\infty = \frac{C_{int}}{p} \tag{3.101}$$

The transformed differential equation is then simple to solve and has a solution

$$\tilde{C} = \frac{C_{int}}{p} e^{\pm\sqrt{\frac{Up}{D_z}}z} \tag{3.102}$$

Choosing the positive root, leads to an un-physical solution with the concentration profile growing away from the solution interface so the negative sign is chosen for the general transform solution.

Taking the inverse transform then gives the concentration profile as

$$c(x,z) = Cint\left[1 - erf(\frac{z}{2}\sqrt{\frac{U}{Dx}})\right] \tag{3.103}$$

or

$$c(x,z) = C_{int} erfc\left[\frac{z}{2}(\frac{U}{D_z x})^{\frac{1}{2}}\right] \tag{3.104}$$

where *erfc* is the complimentary error function given by

$$erfc[x] = 1 - erf[x] = 1 - \frac{2}{\pi^{\frac{1}{2}}}\int_0^x exp[-t^2]dx \tag{3.105}$$

where *erf* is the error function and t is a dummy integration variable.

Figure 3.10 above shows the steady state concentration profile derived. As can be seen the concentration decays away from $z = 0$ which is the surface

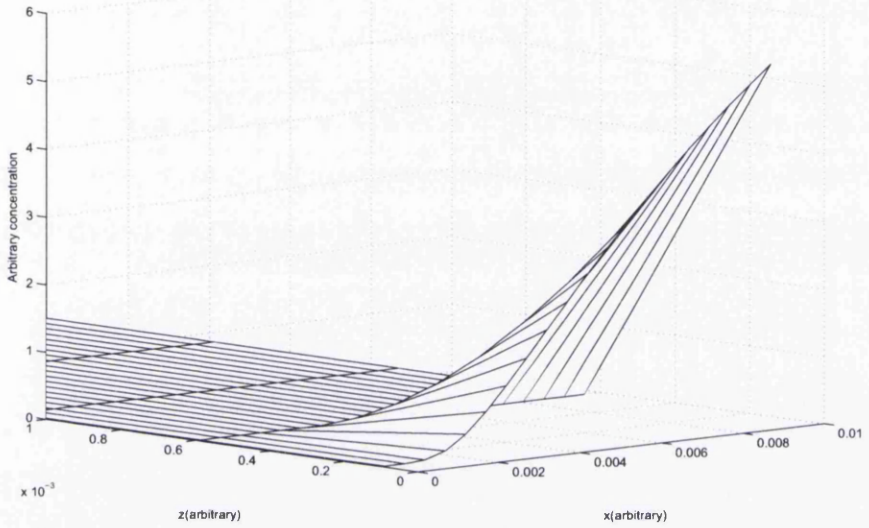

Figure 3.10: Plot of the derived steady state concentration profile for an arbitrary diffusion coefficient and stream velocity on arbitrary axis

of the casting solution and increases along the axis of the solution due to the flow U_x. It should now be expected that evaporation rates should lessen with increasing distance from the edge of the sample solution with respect to the x-axis due to the lowered concentration gradients. This should now be reflected in a lowering of the mass transfer coefficient along the x-axis.

Moving back now to equation 3.3, the evaporative flux was defined as

$$j_i = -D_i \left| \frac{dc_i}{dz} \right|_{lim\ z \to 0} = k^*_{av}(c_i^{int}) \tag{3.106}$$

Now that an expression for the concentration profile has been derived, the left hand side of this expression can be evaluated.

Setting $\frac{z}{2}(\frac{U}{D_z x})^{\frac{1}{2}} = \Theta$

gives

$$\frac{\partial c(x,z)}{\partial z} = \frac{\partial}{\partial z}[C_{int} - C_{int} erf[\Theta]] \tag{3.107}$$

noting that $\frac{\partial}{\partial z}[erf(z)] = \frac{2}{\sqrt{\pi}} exp[-z^2]$

gives

$$\frac{\partial c(x,z)}{\partial z} = -C_{int}\frac{2}{\sqrt{\pi}} exp[\Theta^2]\frac{\partial \Theta}{\partial z} = -\frac{C_{int}}{\sqrt{\pi}} exp[\frac{z}{2}(\frac{U}{D_z x})^{\frac{1}{2}}{}^2](\frac{U}{D_z x})^{\frac{1}{2}} \tag{3.108}$$

taking the limit as z goes to zero gives

$$\frac{dc_i}{dz} \mid_{lim\ z \to 0} = \frac{-C_{int}}{\sqrt{\pi}}(\frac{U}{D_z x})^{\frac{1}{2}} \tag{3.109}$$

once again returning to the expression for the evaporation flux

$$j_i = -D_i \frac{dc_i}{dz} \mid_{lim\ z \to 0} = k^*_{av}(C^{int}) \tag{3.110}$$

Inputting all the relevant parameters into equation 3.110 gives the mass transfer coefficient for a general stream flow rate, diffusion coefficient and length across the casting solution as

$$k(x, u, D) = \frac{1}{\sqrt{\pi}} (\frac{U_x D_z}{x})^{\frac{1}{2}} \tag{3.111}$$

Since the evaporation rate is considered as a singular entity for the casting solution it is necessary to account for the differing path lengths for flow over the solution and also the different mass-transfer coefficients with respect to the axis of the direction of flow.

In order to do this an averaging process is carried out over the casting solution surface. It is considered that the solution has a circular shape. The mass transfer coefficient has a general form $\delta(x) = a\sqrt{\frac{b}{x}}$, creating a coordinate axis with an origin at the centre of the casting solution

The path lengths for the humid air flow passing over the casting solution are given by the equation of a circle as a function of the y coordinate as $x_{path} = 2\sqrt{r^2 - y^2}$. In order to derive an average mass transfer coefficient over the casting solution, the mass transfer coefficients must be summed and averaged over these path lengths. This can be achieved by performing a

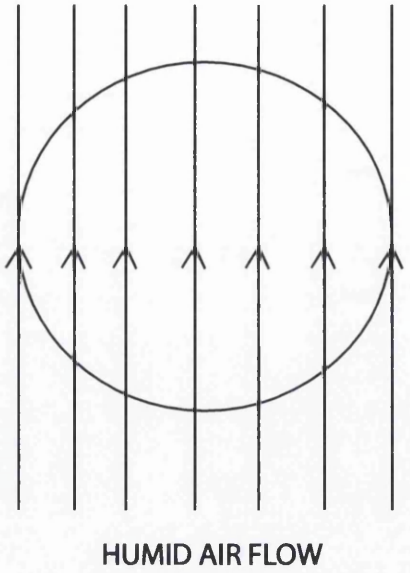

Figure 3.11: Humid air flow over casting solution

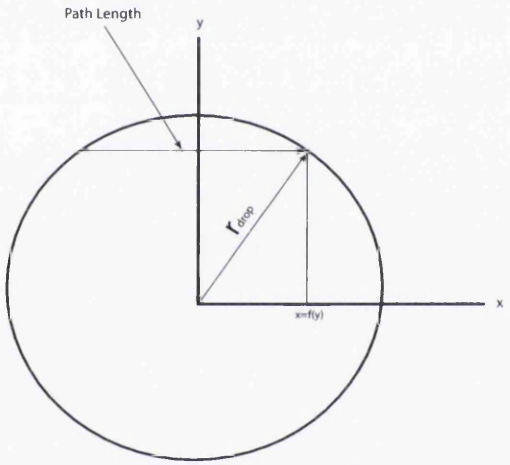

Figure 3.12: Coordinate axis

double integration summing and averaging the function derived for coefficients over all path lengths for the droplet. It is only necessary to do this from the centre outwards due to symmetry. The average boundary layer thicknesses

are then given by

$$\delta(x)_{ave} = \frac{2}{\pi r^2} \int_{y=0}^{y=r} \int_{0}^{2\sqrt{r^2-y^2}} a\sqrt{\frac{b}{x}} dx dy \tag{3.112}$$

performing the integration along the x axis firstly

$$\delta(x)_{ave} = \frac{2}{\pi r^2} \int_{y=0}^{y=r} \left[\frac{a}{\frac{1}{b}}(\frac{x}{b})^{1/2}\right]_0^{2\sqrt{r^2-y^2}} dy = \frac{2}{\pi r^2} \int_{y=0}^{y=r} [2^{\frac{3}{2}} a b^{\frac{1}{2}} (\sqrt{r^2-y^2})^{\frac{1}{2}} - 0] dy \tag{3.113}$$

this then leaves an integral of the form

$$\delta(x)_{ave} = \frac{2}{\pi r^2} \int_{y=0}^{y=r} D(r^2-y^2)^{1/4} dy \tag{3.114}$$

where $D = 2^{\frac{3}{2}} a b^{\frac{1}{2}}$

The appropriate values for the coefficients can then be substituted into the integrals and the integrals can be performed for the relevant diffusion coefficients and stream flow rates. This then gives the average values for the mass transfer coefficients over the solution surface.

Figure 3.13 shows plots of the mass transfer coefficients for three different flow rates.

To summarize the influence of flow on the evaporation rate has been estimated in the numerical model by derivation of the mass transfer coefficient. This was derived by considering a transport equation for the solvent when a one dimensional flow was present. Now we consider how the pubescence of

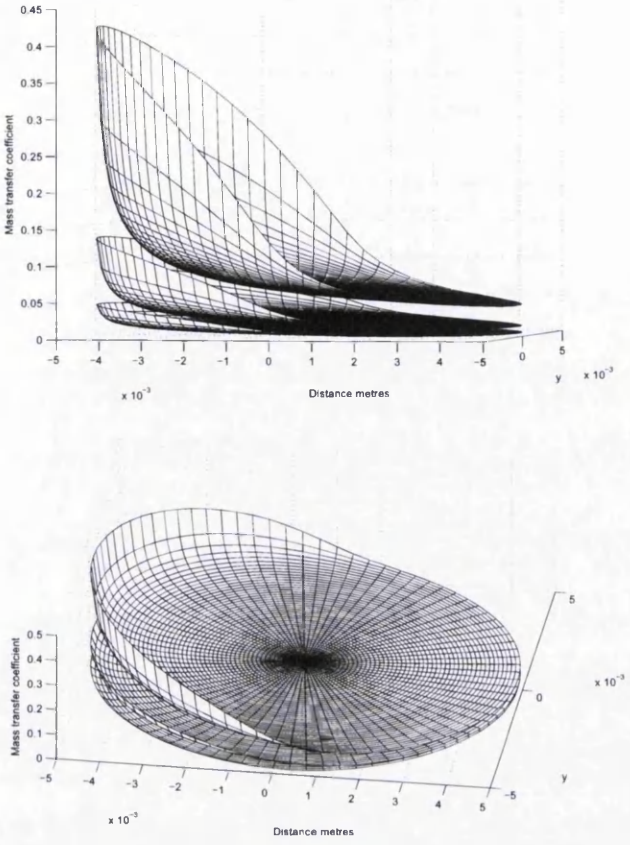

Figure 3.13: Mass transfer coefficients, over casting solution, for two different flow rates

flow could affect the thermodynamics.

In order to evaluate the influence of the presence of flow on the thermodynamics of the process the concept of thermodynamic and velocity boundary layers is introduced. It is well known that when a fluid flows over a surface the fluid velocity near the surface is retarded such that a velocity profile is induced normal to the surface. The boundary layer $\delta(x)$ is then usually defined as the height above the surface such that $\frac{v(x,y)}{V_{stream}} = 0.99$. i.e. the velocity of

the fluid is 99% of the stream velocity.

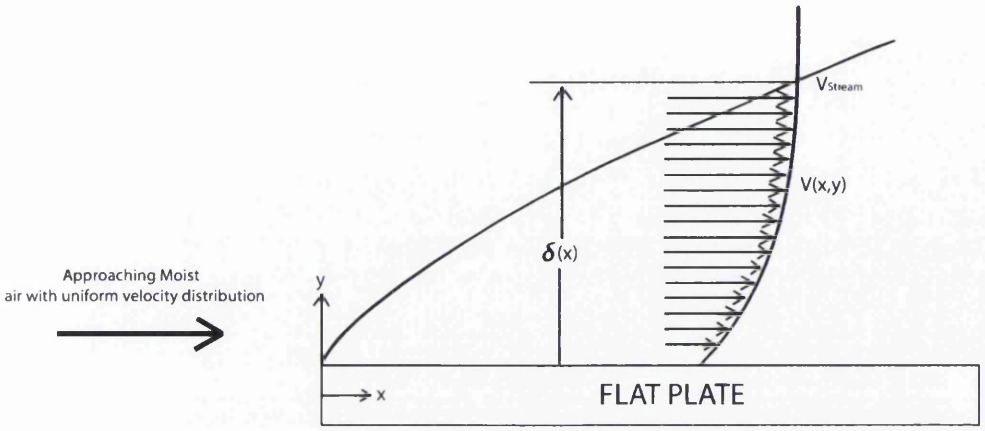

Figure 3.14: Diagrammatic representation of the generation of a velocity boundary layer when a fluid is incident on a flat plate

In order to describe the influence of flow on the production dynamics strictly the Navier Stokes equations should be solved for the exact experimental setup being used to yield profiles for the air/vapour velocity profiles. However there are some treatments available which allow estimation of the boundary layer thickness. One such treatment is the Blasius treatment for a laminar incompressible fluid on a flat plate at zero incidence in a 1-dimensional free stream. In this treatment it is assumed that any pressure gradient in the x direction is negligible and also that no body forces act on the fluid. By assuming that the plate is infinite in the direction into the page it then follows that the flow is only two dimensional. The governing equations

are then given by

$$u\frac{\partial u}{\partial x} + v\frac{\partial u}{\partial y} = v\frac{\partial^2 u}{\partial y^2} \tag{3.115}$$

$$\frac{\partial u}{\partial x} + \frac{\partial v}{\partial y} = 0 \tag{3.116}$$

where u and v are the x and y components of the fluid velocity vectors respectively.

The prediction made for the velocity boundary layer thickness from this treatment is given by

$$\partial(x) = 4.99\sqrt{\frac{\nu x}{V_{stream}}} \tag{3.117}$$

The thermodynamic boundary layer is defined as the distance above a flat plate (solution surface) which is at a different temperature from the bulk stream flow, for which the temperature reaches the fluid stream temperature. In order to derive this distance the situation below is considered.

Moist air that has an inlet temperature $T = T_{stream}$ is incident on a flat surface which is cooled for distances greater than $x = x_0$. By making some assumptions about the form of the temperature profiles it can be shown [46] that the ratio of the thermal boundary layer to the velocity boundary layer σ for distances greater than x_0 can be described in terms of the Prandtl number Pr as

$$\sigma = 0.976 Pr^{-\frac{1}{3}} \left[1 - \left(\frac{x_0}{x}\right)^{3/4}\right]^{1/3}$$

The Prandl number is defined as $Pr = \frac{\nu}{\alpha}$ where ν is the kinematic viscosity and α is the thermal diffusivity. The Prandl number therefore describes the relative ease of momentum to heat diffusion in a given system.

Substituting the equation for the velocity boundary layer developed from the Blasius treatment

$$\partial(x) = 4.99(\sqrt{\frac{\nu x}{V_{stream}}}) \tag{3.118}$$

gives

$$\partial_T(x) = 0.976 Pr^{-\frac{1}{3}} \left[1 - \left(\frac{x_0}{x}\right)^{3/4}\right]^{1/3} 4.99(\sqrt{\frac{\nu x}{V_{stream}}}) \tag{3.119}$$

This thermal boundary layer is now used as a tool in describing the influence of flow on heat transfer. The thermal boundary thickness calculation allows placement of a perfect thermal contact boundary condition above the evaporating solution. Once again the height of the thermal boundary layer must be averaged over the casting solution to account for differing flow path lengths.

The same averaging process must be carried out as for the evaporation mass transfer coefficients. A double integral is performed which results in a single integration which must be performed numerically, of the form

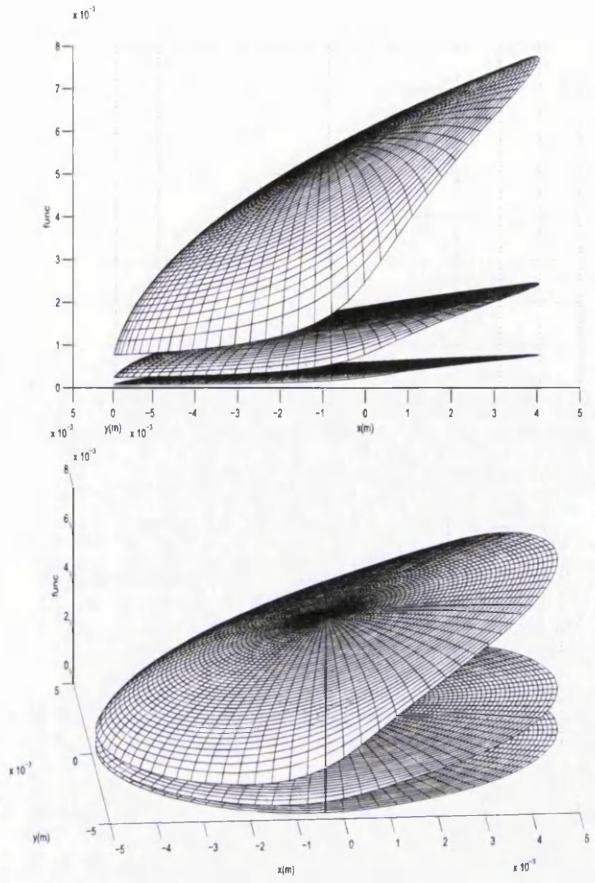

Figure 3.15: Thermal boundary layer thicknesses over casting solution for flow rates of 0.05, 0.5 and $5ms^{-1}$ respectively

$$\delta(x)_{ave} = \frac{2}{\pi r^2} \int_{y=0}^{y=r} D(r^2 - y^2)^{3/4} dy \tag{3.120}$$

Even though the velocity is reduced with respect to the stream velocity V_x below the velocity boundary layer becoming smaller closer to the surface of the casting solution, there will however still be some movement. This movement will also effect the transport of heat through the boundary layer and produce a net convective heating effect at the surface. In order to quantify this effect

strictly the Navier Stokes equations should be solved for the whole system. This cannot be achieved within the context of our one dimension model. There is however a way to overcome this problem by using non-dimensional groups as will now be shown.

The energy equation within the boundary layer is given by

$$U_x \frac{\partial T}{\partial x} + \nu \frac{\partial T}{\partial y} = \frac{k}{\rho C} \frac{\partial^2 T}{\partial y^2} \tag{3.121}$$

Non dimensionalising the spacial variables, using the length of the casting solution L as the characteristic length scale. i.e setting

$$x^* = \frac{x}{L} \tag{3.122}$$

and

$$y^* = \frac{y}{L} \tag{3.123}$$

and letting

$$U^* = \frac{U_x}{V_{stream}} \tag{3.124}$$

and

$$\nu^* = \frac{\nu}{V_{stream}} \tag{3.125}$$

where V_{stream} is the velocity at the edge of the velocity boundary layer.

Also setting

$$T^* = \frac{T - T_{int}}{T_{stream} - T_{int}} \tag{3.126}$$

These substitutions then give equation 3.121 as

$$U^* \frac{\partial T^*}{\partial x} + \nu^* \frac{\partial T^*}{\partial y} = \frac{k}{\rho C V_{stream} L} \frac{\partial^2 T}{\partial y^2} \tag{3.127}$$

The coefficient on the right hand side, $\frac{k}{\rho C V_{stream} L}$ can be expressed using the non-dimensional groups $Re = \frac{V_{stream} L}{\nu}$ and $Pr = \frac{\nu \rho C}{k}$

The local convective heat transfer coefficient is defined by

$$h_x = \frac{q'}{T_{int} - T_{stream}} \tag{3.128}$$

where $q'$is the local heat flux defined by

$$q' = \frac{\partial T}{\partial y} \mid_{y=0} \tag{3.129}$$

The heat flux can also be expressed in terms of the earlier substitutions T^* and y^* as

$$\frac{(\partial T^*(T_{stream} - T_{int}) + T_{int})}{\partial (Y^* L)} = \frac{T_{stream} - Tint}{L} \frac{\partial T^*}{\partial y^*} \mid_{y=0} \tag{3.130}$$

so the local convective heat transfer coefficient can be expressed as

$$h_x = \frac{k}{L} \frac{\partial T^*}{\partial y^*} \mid_{y=0} \tag{3.131}$$

The Nusselt number gives the ratio of convective to conductive heat fluxes, $N_u = \frac{h_x}{Lk}$, so the term $\frac{\partial T^*}{\partial y^*} |_{y=0}$ can be correlated in terms of known correlations of the Nusselt number for prescribed geometries. Such as the correlation developed by Dowdy and Karabash [47] which is frequently used in the literature regarding evaporative systems [48][49]

$$Nu = 0.10. \left(\frac{L_e}{L}\right)^{0.1} Re^{0.8} Pr^{1/3} \tag{3.132}$$

where Le is the volume to surface area ratio of the evaporating substance and L is the thickness.

Using this correlation the convective heat flux to the evaporating surface can be calculated via [3]

$$q_{surface} = Ah_x(T_{int} - T_{bulk}) \tag{3.133}$$

[3]The convective heat transfer coefficient method was not used in the simulation results in this thesis, since this idea conflicts with including conduction through the thermal boundary layer in the calculations. In order to use the convective heat transfer coefficient the air layer above the evaporating solvent does not need to be included explicitly in the domain, the boundary condition at the top of the domain is then set as a constant heat flux dependant on equation 3.133, this method is included just to demonstrate alternative methods considered

3.3 Influence Of Flow Rate On Condensation

The influence of the flow rate on deposited water seems conceptually simple. However is really very difficult to quantify. The most obvious effect that flow will have on condensation is the reduction of the time scales for the process to occur based on the increased rates of evaporation. In order to truly evaluate this effect nucleation and growth must be considered at the surface of the casting solution. Increased flow rate also means that any water vapour that diffuses onto the surface does so at increased velocity in the direction of flow. It therefore must lose a greater amount of energy to become condensed. On a molar basis this is equal to $\frac{1}{2}\Delta M_{cond}{V_x}^2$, which for a flow rate of $1ms^{-1}$ is therefore exactly 0.00225 of a joule per mol of deposited condensate. The heat of condensation is roughly $40kJ$ mol so clearly this effect is negligible in comparison. An effect which may not be negligible is viscous heating. To take this effect into account a term $\mu\left(\frac{\delta V_x}{dy}\right)$ must be included in the energy equation used to describe the heat transfer process where μ is the dynamic viscosity of the air, of course this term should be included above the sample solution within the thickness of the velocity boundary layer.

How could the effect of this term be estimated. In actuality once again the Navier Stokes equations should be solved for the system! But some headway can be made by guessing a velocity profile. If we consider a profile for the velocity of humid air $U_x(y)$ above casting solution as being a polynomial of

order three i.e.

$$U_x = ay - by^2 + cy^3 \tag{3.134}$$

Assuming a no slip boundary condition at the top of the casting solution, that is the humid air is brought to rest at the casting solution surface. Consequently the shear stress must approach a constant value. Another consequence of this is that $(\frac{\partial^2 U_x}{dy^2})_{y=0} = 0$. It follows that b=0. $V_x(y)$ is also defined as becoming that of the stream at $y = \delta$ where δ is the thickness of the velocity boundary layer therefore, $c = -\frac{U_s}{2\delta^3}$ and $a = -\frac{3}{U_s}2\delta$. The velocity profile is then given as

$$U_x = 3\frac{U_s}{2}\frac{y}{\delta} - \frac{U_s}{2}(\frac{y^3}{\delta}) \tag{3.135}$$

This equation corresponds closely to experimentally-determined velocity profiles in a laminar boundary layer [46]

This then gives the term in the energy equation for frictional heating as

$$3\frac{U_x}{\partial y} = \frac{U_s}{2}\frac{1}{\delta} - 3\frac{U_s}{2}(\frac{y^2}{\delta})\mu \tag{3.136}$$

This is once again a parameter which will vary over the casting solution due to the differing boundary layer thickness over the solution and must therefore be averaged in the same way using a double integration. This term can be included easily in the energy equation. The term can be calculated ac-

cording to the derived term at any height above the surface and incorporated within the source term used for internal energy generation.

After nucleation and growth of droplets has started apart from effecting diffusion of vapour to the droplets already created, the flow might gepadise the droplets structural integrity and adhesion to the casting solution surface thus effecting the ordering of the final film. The calculations that follow are intended to be thought provoking only and serve to promote discussion. This is because there is no generally excepted theory of how the droplets behave and interact with the surface.

Firstly what kind of force does a droplet experience when it is formed on the surface. As a first approximation, the droplets shape and orientation to the surface is neglected, so it follows that under this approximation the flow of humid air passing over the surface is unaffected. Once again treating the casting solution as a flat plate, with a no slip condition at the surface, this gives an approximation to the flow velocity profile as above.

$$U_x = 3\frac{U_s}{2}\frac{y}{\delta} - \frac{U_s}{2}(\frac{y^3}{\delta}) \tag{3.137}$$

In order to estimate the flow imparted on the surface by the flow we need to sum the contributions from the shear stress at each point on the surface. Which is effectively summing the momentum flux over the surface.

$$F_x = \int_{z=0}^{z=r} \int_{0}^{2\sqrt{r^2-z^2}} \mu \frac{\partial \nu_x}{\partial y} |_{y=0} \, dx dz \tag{3.138}$$

adding the Blasius solution for the boundary layer gives

$$\frac{V_x}{V_\infty} = \frac{3}{2}\left(y\sqrt{\frac{13V_\infty}{280\nu x}}\right) - \frac{1}{2}\left(y\sqrt{\frac{13V_\infty}{280\nu x}}\right)^3 \tag{3.139}$$

Differentiating with respect to y

$$\frac{\partial V_x}{\partial y} = V_\infty \mu \frac{3}{2}\left(\sqrt{\frac{13V_\infty}{280\nu x}}\right) - y^2 \frac{3}{2}\left(\sqrt{\frac{13V_\infty}{280\nu x}}\right)^3 \tag{3.140}$$

and equating y=0

$$\frac{\partial V_x}{\partial y} |_{y=0} = V_\infty \mu \frac{3}{2}\left(\frac{13V_\infty}{280\nu x}\right) \tag{3.141}$$

Firstly the integral is performed over the whole of the casting solution to get an idea of the magnitude of the force. Performing an integration in the x direction firstly

$$F_x = V_\infty \int_{z=0}^{z=r} \left[\mu.3\left[\sqrt{\frac{13V_\infty x}{280\nu V}}\right]\right]_0^{2\sqrt{r^2-y^2}} dz \tag{3.142}$$

This integration can then be performed numerically for a range of stream velocity's to gauge the magnitude of the force exerted parallel to the surface the results are given in **??**.

Now that the magnitude of the drag force across the surface of the casting solution has been gauged, the same principles can be applied to a drop on

Flow Speed ms^{-1}	0.06	.1	.2	.5	1
$F_x(N)$	1.519×10^{-9}	1.034×10^{-7}	$2.924 \times 10^{-}7$	1.156×10^{-6}	3.269×10^{-6}

Table 3.7: Sum of momentum flux on surface of casting solution

the surface. For this calculation an idealised situation is analysed where half of the droplet sits under the surface of the solution, such that only half of the droplet is exposed to the flow. In this calculation it is assumed that the droplet itself does not alter the flow in any way, such that the same velocity profile as used previously can be used in calculations. In order to work out how the airflow effects the droplets motion on the surface, the forces acting on the droplet are analysed. The forces which act on the droplet are the pressure ,shear force, fluid drag (due to the any motion of the droplet on the liquid surface) and also forces due to residual surface energy.

Firstly we shall discuss the pressure force on the drop. The ambient pressure is equal on both sides of the drop so there is no contribution to the force on the droplet. However we assume that the air is brought to rest at the droplets surface such that a stagnation pressure is imparted on the droplet due to the flow of magnitude $\frac{1}{2}\rho V_x(x,y)$. It is further assumed that this is only present on one side of the part of the droplet exposed to the flow. In order to perform this calculation the stagnation pressure at a point on the droplet surface is summed over half of the surface. This then gives a force imparted

on the droplet in the direction of the flow. In order to perform this calculation the droplet is played at the centre of an cartesian cordinate system, which is placed at the centre of the casting solution. In order to realise this situation the velocity profile x coordinate is changed to $x_s = x + \sqrt{R^2 - z^2}$ where the z coordinate is perpendicular to the flow direction on the surface of the casting solution and R is the radius of the casting solution drop. This transformation of coordinates ensures that the appropriate velocity profile is attained at the leading edge(the casting solution edge).

$$\frac{1}{2}\rho V_\infty \{ \int\int_{droplet} \frac{3}{2}\left(y\sqrt{\frac{13V_\infty}{280\nu x_s}}\right) - \frac{1}{2}\left(y\sqrt{\frac{13V_\infty}{280\nu x_s}}\right)^3 dxdydz \tag{3.143}$$

A hemispheric coordinate system as depicted in figure 3.16 is now appropriate and after some manipulation the force due to the stagnation pressure on the droplet is

$$\frac{1}{2}\rho V_\infty \{ \int_0^{\frac{pi}{2}}\int_0^{pi} \frac{3}{2}\alpha r cos\theta \left(rcos(\phi)sin(\theta) - \sqrt{(R^2 - r^2sin^2(\phi)sin^2(\theta))}\right)^{-\frac{1}{2}} d\theta d\phi -$$
$$\int_0^{\frac{pi}{2}}\int_0^{pi} \frac{1}{2}\alpha^3 r^3 cos^3\theta \left(rcos(\phi)sin(\theta) - \sqrt{(R^2 - r^2sin^2(\phi)sin^2(\theta))}\right)^{-\frac{3}{2}} d\theta d\phi \}$$

The force in the x-direction due to the shear stress is

$$\int\int_{droplet} \tau ds cos\theta dxdydz \tag{3.144}$$

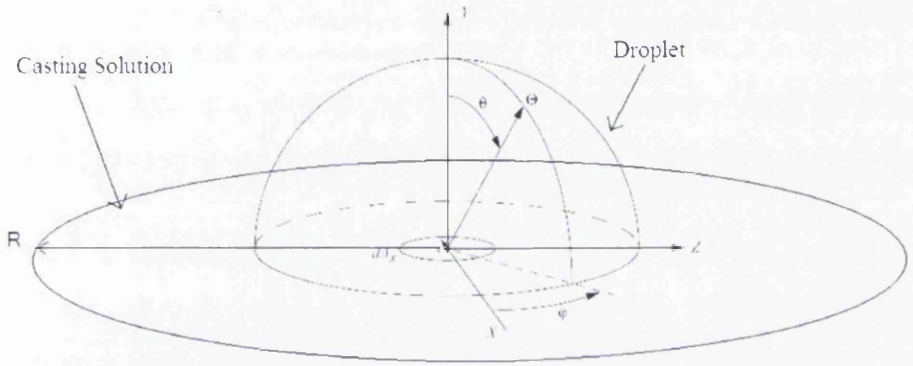

Figure 3.16: Coordinate system used in calculations

where ds is an infinitesimal area on the droplet and θ is the angle the surface makes with the x axis. The component of the shear stress in this direction is

$$\tau dscos\theta = \mu \frac{dV_x}{dy} \tag{3.145}$$

using the same velocity profile as previously gives

$$\mu V_\infty \{ \int \int_{droplet} \frac{3}{2} \left(\sqrt{\frac{13V_\infty}{280\nu x_s}} \right) - \frac{1}{2} \left(y^2 \sqrt{\frac{13V_\infty}{280\nu x_s}} \right)^3 dxdydz \tag{3.146}$$

In the same fashion after some manipulation the force component in the x-direction due to shear stress is .

$$\mu \{ \int_0^{\frac{pi}{2}} \int_0^{pi} \frac{3}{2} \alpha \left(rcos(\phi)sin(\theta) - \sqrt{(R^2 - r^2 sin^2(\phi) sin^2(\theta))} \right)^{-\frac{1}{2}} d\theta d\phi -$$
$$\int_0^{\frac{pi}{2}} \int_0^{pi} \frac{3}{2} \alpha^3 r^2 cos^2\theta \left(rcos(\phi)sin(\theta) - \sqrt{(R^2 - r^2 sin^2(\phi) sin^2(\theta))} \right)^{-\frac{3}{2}} d\theta d\phi \}$$

where $\alpha = \sqrt{\frac{13V_\infty}{280\nu}}$

These forces will induce motion of the droplet in the direction of the flow. In the opposite direction the droplet will experience a drag force due transfer of momentum to the casting solution. For low Reynolds number the drag force can be approximated using Stokes law which is given as

$$F_d = -3\pi\nu r V \tag{3.147}$$

for a hemisphere of radius r moving at speed V relative to the fluid with dynamic viscosity ν in which it is submerged. In the following calculations we ignore any retardation due to interfacial energy related effects. The two integrals described above were performed numerically for two droplet sizes and input velocities. Instead of analysing the dynamic behaviour of the droplet an upper bound to the droplet velocity is gauged by determining the terminal velocity of the drop based on the acceleration produced by the stream flow at the centre of the casting solution.

Flow Speed ms^{-1}	**0.06**	**.1**	**.2**	**.5**	**1**
$V_{terminal}$	2.39×10^{-11}	5.13×10^{-11}	1.45×10^{-10}	5.74×10^{-10}	1.62×10^{-9} **1**
F_p	1.99×10^{-21}	4.29×10^{-21}	1.23×10^{-20}	4.80×10^{-20}	1.36×10^{-19}
F_{shear}	7.89×10^{-20}	1.69×10^{-21}	4.80×10^{-19}	1.89×10^{-18}	5.39×10^{-18}

Table 3.8: Terminal velocity, shear and pressure force's for a droplet of radius 1 μm

Flow Speed ms^{-1}	0.06	.1	.2	.5	1
$V_{terminal}$	1.52×10^{-12}	3.27×10^{-12}	7.24×10^{-12}	3.65×10^{-11}	1.03×10^{-10} 1
F_p	1.07×10^{-19}	$\times 10^{-21}$	3.04×10^{-19}	1.99×10^{-18}	3.39×10^{-18}
F_{shear}	1.69×10^{-19}	$\times 10^{-21}$	$4.80 \times 10^{-}19$	1.89×10^{-18}	5.37×10^{-18}

Table 3.9: Terminal velocity, shear and pressure force's for a droplet of radius 25μm

Within the limits of this calculation the terminal velocity varies from a 100th of a nanometre per second up to around 2nano-metres's per second. The shear and pressure forces increase with increasing droplet size as expected, however so does the drag resistance resulting in a decreasing terminal velocity with droplet size. The purpose of this calculation is merely to gauge the sizes of the forces which are exerted on the droplet due to the applied airflow and should not serve as as a definitive assessment of the droplet behaviour since there are many effects not considered, such as thermal and surface tension related effects. If the droplet were to travel at its terminal velocity for the duration of the casting experiment even at considerable flow velocity's it would travel some hundreds of nanometres during its lifetime, due to the effects of the applied airflow. Since it takes at most 200s for the solvent in the solution to evaporate. In reality however a droplet will probably never reach a terminal velocity as the forces which it experiences are a function

of its position on the surface. It could be argued from these calculations that the applied airflow probably has negligible effect on the droplets surface motion compared to that induced by other effects related to evaporation and movement of the solvent, except perhaps however at the immediate point of contact between the airflow and the casting solution. Future discussion is left for future studies.

Other effects of flow on condensation will be related to diffusion towards the surface through the evaporating solution, increased rates of evaporation of the solvent in the casting solution could induce slower diffusion of water vapour through the surface due to frictional effects between the two species. Once again it must be emphasised that this effect was neglected in this model. Condensed water could also be transported away from the casting solution with the solvent. Greater rates of evaporation could enhance this effect.

The program for simulating the casting process can therefore be summarized in its entirety by (see figure 3.16)

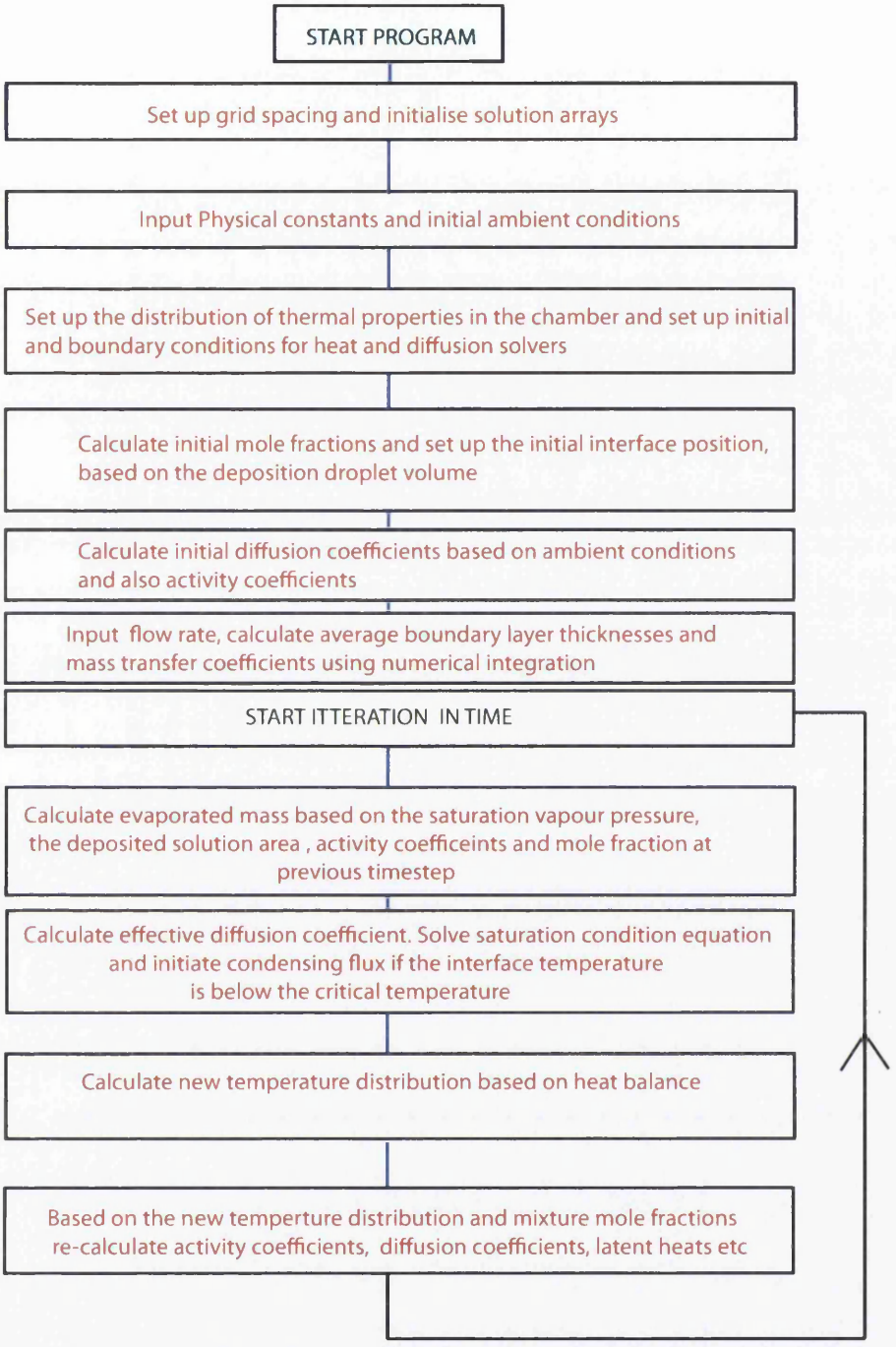

Figure 3.17: Flow diagram for evapotranspiration program

3.4 Testing And Validation

In order to check to the consistency of the solving methods for the energy equations involved in solving the entire problem. The solver was used to obtain a numerical solution to a problem for which the analytical solution could also be derived [50].

Consider an iron bar made of length 50cm, with specific heat capacity c=0.437 $\frac{J}{gK}$, density 7.88 $\frac{g}{cm^3}$ and thermal conductivity 0.836 $\frac{W}{cmK}$ that initially has the temperature distribution $\psi(x) = 5 - 1/5[x - 25]$ where $\psi(x)$ is given in degrees Celsius. We assume the sides of the bar are perfectly insulated. At t=0 the ends of the bar are placed in an ice bath (0 degrees Celsius). We can use the Crank-Nicholson solver described above to solve this problem and see how it compares to the analytical result.

The Problem

$$\frac{\partial T}{\partial t} = \alpha \frac{\partial^2 T}{\partial x^2}$$

$$0 < x < 50, t > 0$$

$$u(x, 0) = \psi(x)$$

$$u(0, t) = 0$$

$$u(50, t) = 0$$

This initial boundary value problem may be solved using a fourier series method

By representing the solution as a Fourier series

$u(x,t) = \sum_{n=1}^{\infty} a_n(t) sin(n\Pi x/50)$

it can be shown that the coefficients $a_n(t)$ satisfy the initial value problem

$\frac{da_n(t)}{dt} + \frac{kn^2\Pi^2}{50^2\rho c} a_n = 0$

$a_n(0) = b_n$

Solving the IVP this gives an approximate solution

$u_N(x,t) = \sum^N{}_{n=1} b_n e^{\frac{-kn^2\Pi^2}{50^2\rho c}} t sin\left(\frac{n\pi x}{50}\right)$

plotting the temperature distribution in the rod at various times using 1000 terms of the series (figure 3.17).

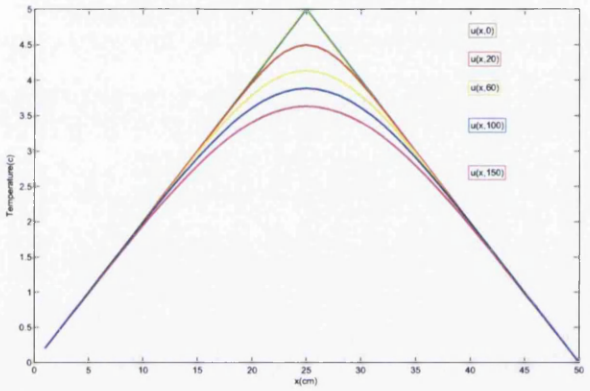

Figure 3.18: Snapshots of the temperature distributions at time t=0s, t=20s, t=60s, t=100s and t=150s using 1000 terms of the series solution

and plotting the results using the Crank Nicolson solver at the same points in time as for the analytical result a good agreement can be observed (figure 3.18).

The temperature distributions obviously seem the same. Now we consider the errors produced by using the Crank Nicolson Scheme. To do this we look

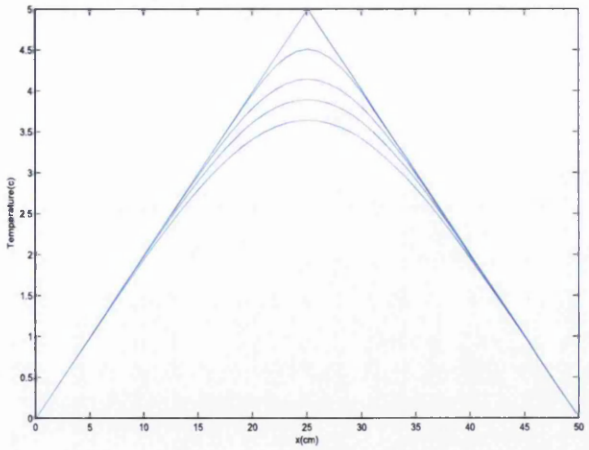

Figure 3.19: Plot of the temperature distributions at times t=0,t=20s, t=60s, t=100s, and t=150s

at the difference in the analytical and numerical results through the spacial and temporal domain .

A comparison is made between the results when using spacial and temporal steps of 1s and 1cm respectively and that when using steps of 0.1s and 0.1cm (Figure 3.19).

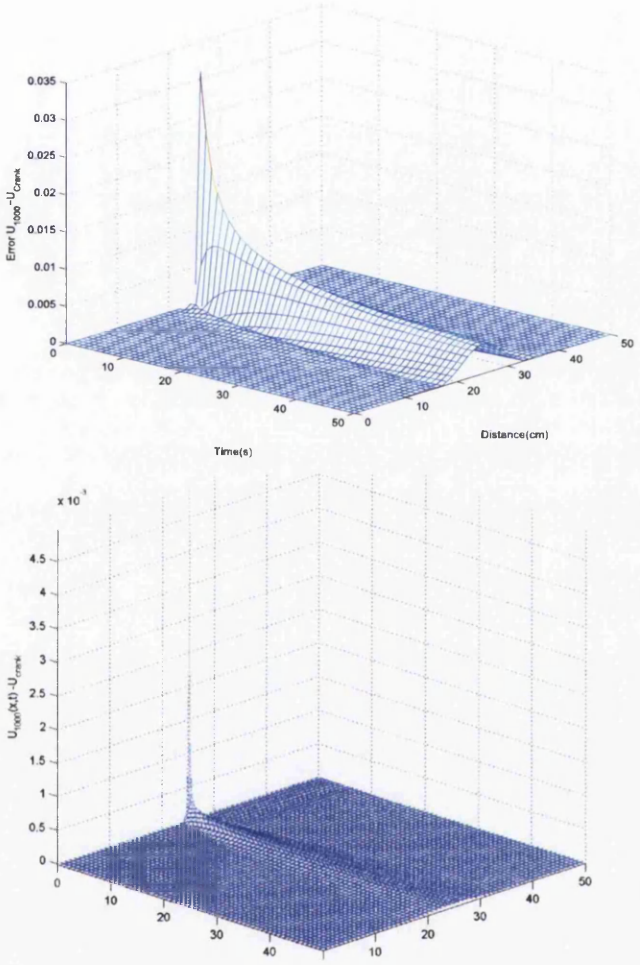

Figure 3.20: Difference in numerical and analytical results over the domain for spacial and temporal step sizes of 1s and 1cm and, 0.1s and 0.1cm respectively

The local truncation errors are clearly decreasing with decreased spacial and temporal steps. With a maximal truncation error of better than order h^2+k^2 , where h and k are the spacial and temporal grid spacings respectively, the errors are presumably only better than the expected order h^2+k^2 due to only using 1000 terms of the series solution.

In order to verify that the whole models behaviour is independent of the grid spacing the model is used to calculate some evaporation rates temperature drops and condensate masses using different grid spacings. The position of the interface of the casting solution sets the limit for the maximum allowed spacial grid-spacing since this interface lies when approximating the solution as a cylinder at a distance of about half a millimetre above the substrate. The maximum allowed grid-spacing we shall examine is therefore approximately 0.0001 metres in order to resolve the casting solution. Firstly we use this spacial grid-spacing and look at the behaviour of the system when changing the temporal spacing. In order to solve the series of matrix equations for the Crank Nicolson method a Conjugate Gradient Squared (CGS) method was used with a specified tollarence of 10^{-6}. This means that the matrix equations must be satisfied within a $\pm 10^{-6}$ for the solution to converge. In order for the (CGS) method to converge within the desired tollerance a maximum temporal grid spacing of 1s is observed.

Beyond 0.001s any change in the solutions is very small (figure 3.20).

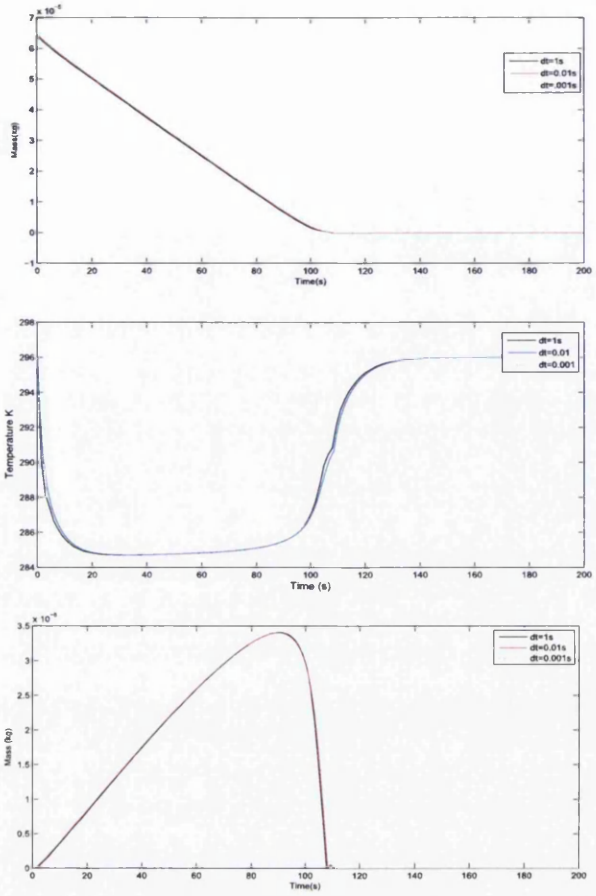

Figure 3.21: Effect of temporal grid-spacing on solutions

Now the spacial grid-spacing are changed and the effects on the solution are examined figure 3.21.

As can be seen the changes in the solution are negligible after the spacial gridspacings reach a 100^{th} of a mm. In order to decrease the number of iterations needed for the CGS method to converge on the solution of the matrix equations at a given time-step the time steps were reduced to 0.0002s. The spacial grid-spacing used were 0.00001m. In order to allow this kind of

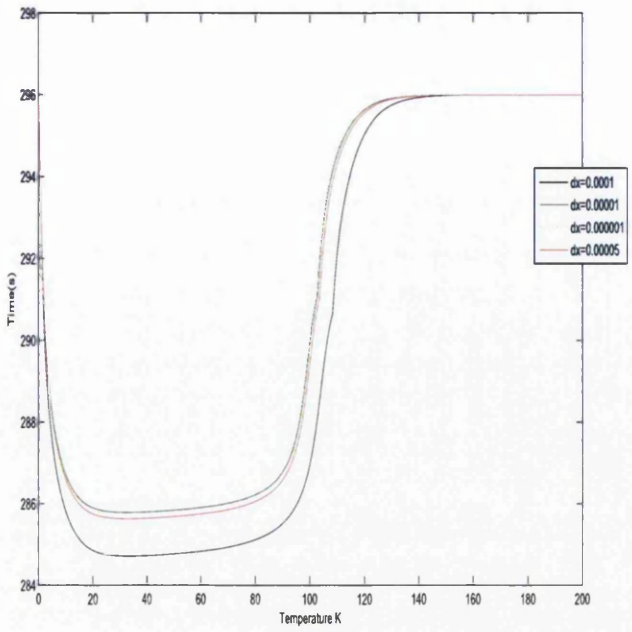

Figure 3.22: Temperature solutions with different spacial gridspacings

precision when working on a standard PC, data that was only needed to allow calculation of any required parameters at the next time-step was cleared from memory after being used.

Chapter 4

Experimental Methods

This chapter aims to gives an overview, of how the experimental part of the work was carried out. During this work access to an automated environmental chamber was not available, this meant that a chamber had to be built in house. This chamber must allow access to instruments for recording and viewing the ambient conditions and the temperature close to the sample. The chamber obviously had to allow access to a sample slide for depositing sample solution. Inlet and outlet valves were also incorporated to allow input of humid air to create the desired conditions. The size of the chamber would also have to be adequate such that it could fit into a mass balance which is used for recording evaporation data. This resulted in the production of the chamber shown in figure 4.1.

In order to create the casting conditions within the chamber, the relative humidity and temperature in the chamber needed to be recorded and

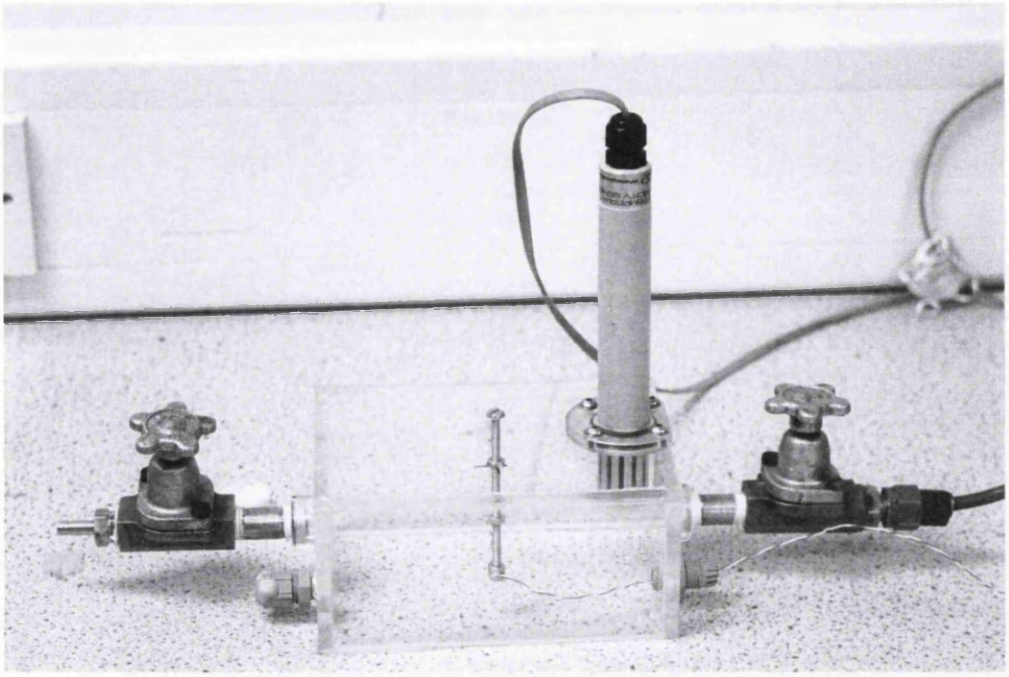

Figure 4.1: Casting chamber

monitored. For the recording of these variables, a Pico-Technology hygrometer was used, in conjunction with an a/d converter. This could then be directly interfaced with National Instruments Labview. A program was written for Labview in order to achieve communication with the device. This provided a graphical display for the ambient temperature and humidity inside the chamber (figure 4.2). The versatility of Labwiew, also meant that formulas could be used in order to relate these parameters to water vapor densities and corresponding dew point temperatures. These can be a more useful way of expressing and monitoring the environmental conditions in some circumstances. A program was written to record these variables at a given

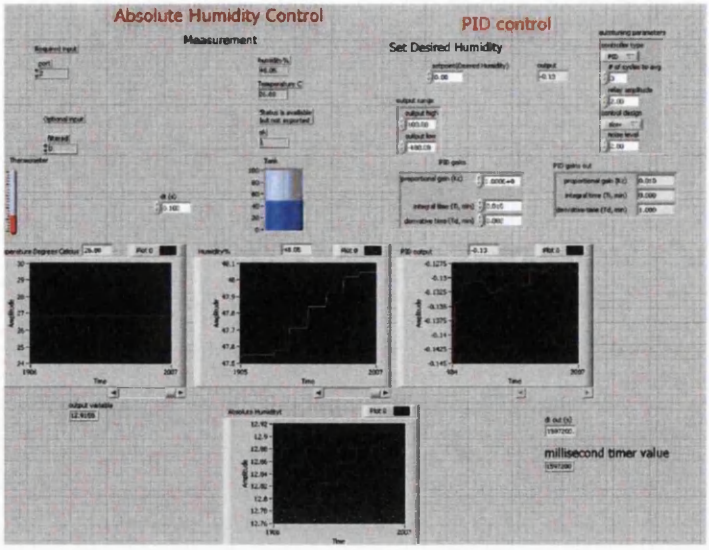

Figure 4.2: Environmental variable display

rate and output to a data file when the experiment was over. In order to record temperature data at specific locations in the chamber, a thermocouple signal was recorded via the use of a National Instruments BNC-2120 A/D converter and a data acquisition card. This information was then recorded in a similar fashion to the ambient conditions.

For casting experiments, manocarboxy-terminated polystyrene with approximate molecular weight 50,000 gm was purchased from Scientific Polymer Inc. Pure carbon disulphide and chloroform were purchased from Sigma Aldrich.

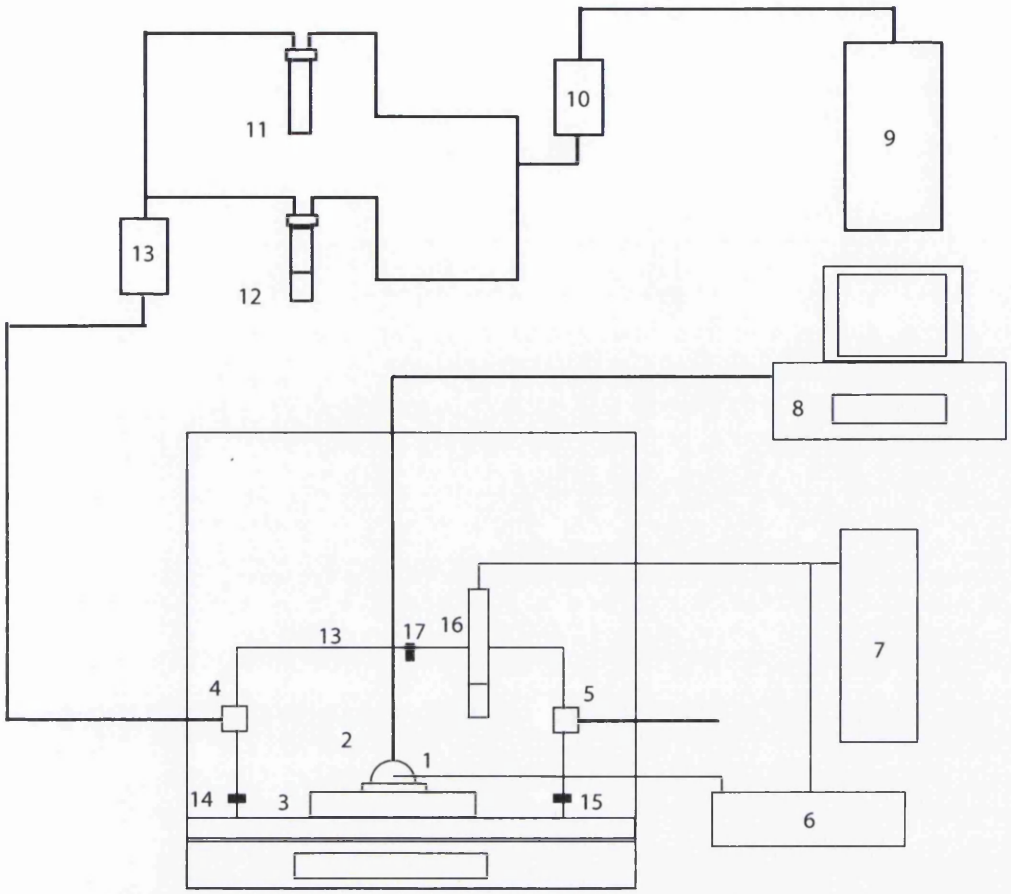

Figure 4.3: Experimental setup

4.0.1 Growth Apparatus

Figure 4.3 shows an overview of the apparatus used in the casting experiments, that will be described. In some experiments only part of the apparatus is used. Environmental conditions are created inside a purpose built chamber (2). The chamber has inlet (4) and outlet (5) valves, for flushing the system with dry or humidified air. There are also grommets (14,15), on the sides of the chamber into which a thermocouple (1) can be fed to record

temperatures above the sample; the thermocouple can be positioned with the aid of a CCD camera and display. At the top of the chamber there are two further grommets, one into which a Pico Technology thermo-hygrometer (16) is fastened and one for injection of sample solution (17). To create the desired environmental conditions, dry air (9) is split, and passed through a chamber containing wire wool (10), and then through two flasks one which is dry (11) and another which contains some de-ionised water (12); the splitting ratio can be altered by the opening or closing of two valves. The air that has passed through the flasks is then recombined and once again passed through a chamber with wire wool in order to remove any large particulates in the stream. This air is then passed into the main chamber. The chamber is also housed over the pan of a mass balance in order to measure evaporation rates during experiments. Temperature and humidity data is then fed back to the PC through ad-converters.

4.0.2 Experimental Procedure

When recording solvent evaporation rates the chamber is first flushed with dry air until the humidity in the chamber is as low as possible; this is so that condensation of water vapour does not affect the results significantly. This can also be verified by ensuring that the temperature in the chamber is always well above the corresponding dew point temperature. Unfortunately

the most accurate mass balance available (A Mettler Toledo AE163) could not be interfaced with Labview, so in order to record the mass of evaporating solution, a camera had to be positioned, in front of the balance display during experiments. The evaporation profile was then determined by frame by frame data entry from recorded movies of the balance display. This gave a time resolution of 0.08(s) and a mass resolution of $\pm 5 \times 10^{-5} g$.

In recording temperature profiles during evaporation, a k-type thermocouple was positioned at the centre of the deposited solution. In performing this type of experiment cavity slides were used in order that the solution drop could be predictably centralised with respect to the thermocouple. A CCD camera and display were used to aid the setup. The thermocouple head was placed such as to become submerged inside the deposited liquid droplet.

This method then allowed the approximate liquid temperature to be recorded. It is noted that placing the thermocouple at the interface could have affected the dynamics of the process, but this was the most accurate method available within the context of available equipment. The thermocouple temperature data was then logged using Laview and the BNC-2120 AD-converter which gave a time resolution of 0.01s and a temperature resolution of $\pm 0.5°C$. During these experiments, when looking at perfect thermal contact conditions beneath the sample slide, water at the ambient temperature was pumped through a Lytron CP-25 cold plate, to ensure that the cold plate remained

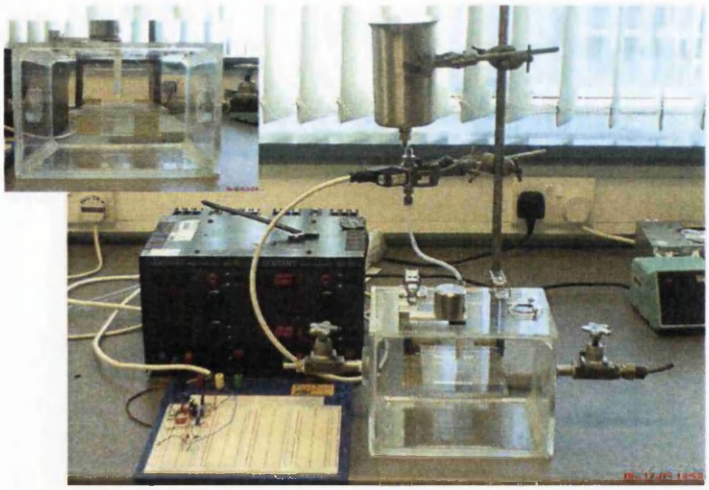

Figure 4.4: Solution deposition apparatus

at ambient temperature.

During casting experiments, the chamber conditions were created by introducing humid air into the chamber created by passing dry air through the bubbler system already described. Conditions in the chamber were then carefully monitored until the desired conditions were reached. The valves of the chamber were then sealed and the casting solution injected onto a sample slide.

Depositing the casting solution onto the chamber in the most accurate and repeatable way possible, was very important. For this reason, a method of depositing the solution that could eliminate human error was developed. This method uses a solenoid valve to allow the casting solution to flow from a reservoir onto the sample slide for a set amount of time. The time could be regulated using a simple circuit.

This method improved the reliability of depositing the casting solution greatly, however, the system would become congested with polymer from the casting solution after just one run which indicated that the concentration of the solutions could be compromised by using this method. Instead micro-pipettes were used to deposit the solution. This allowed small quantities of solution ($50\mu L$) to be deposited with reasonable accuracy. However, a point should be made that a method of deposition which does not necitate human intervention would be vastly preferable. This can be demonstrated by looking at progression of the deposited areas of ($50\mu L$) drops of carbon disulphide figure 4.5, the starting areas are quite different each time.It was not thought wise to spend a large amount of time developing the deposition method but this will hopefully achieve completion in the future.

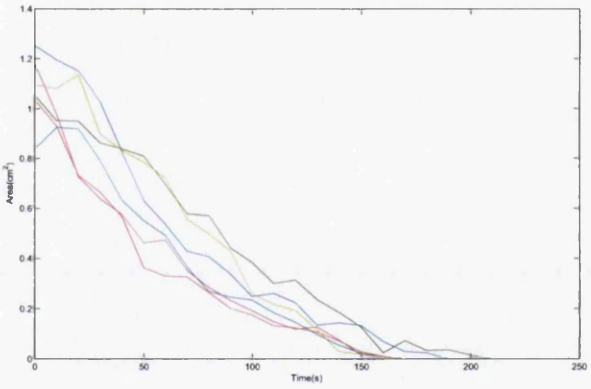

Figure 4.5: CS_2 droplet areas

4.0.3 Film Analysis

It is as important to analyse the produced porous films reliably and thoroughly, as it is to gain information about the physical factors which affected the growth of the structures themselves. In order to retrieve useful data from casting experiments large regions of the polymer films should be examined. In the majority of the literature the extent of information available on the ordering or pore size of a film is normally constrained to that available from a single image of the whole film. For applications which would require large areas of uniform pores information is needed spanning larger distances. Also when developing apparatus for a casting method, it can be difficult do determine whether changes to your setup are having beneficial effects on the experimental outcome. This can be become a subjective process if some kind of quantitative analysis is not adopted. It is for these reasons and also to allow comparison betwen experiments and the numerical model, that an image analysis program was created. The ordering and pore size distributions can then be assessed with ease, over large physical areas. This also enables many consecutive images to be interpreted with a lesser time consumption allowing studies to be carried out that focus on larger areas of the film. In order to image the whole of the produced films a Singer MSM system (micromanipulator) unit is used in conjunction with a standard optical microscope.

4.0.4 Image Analysis Program

The following section gives a condensed description of the methods used for image analysis.

A program is written using Matlab to perform the desired task. Firstly a JPEG image is read into Matlab using the imread function. The image data is now represented as a 2 dimensional array. The corresponding monochrome luminance of each pixel of the original image is calculated by combining the original RGB values according to the NTSC standard. Weights of 0.2989, 0.5870 and 0.1140 for red, green and blue channels respectively.

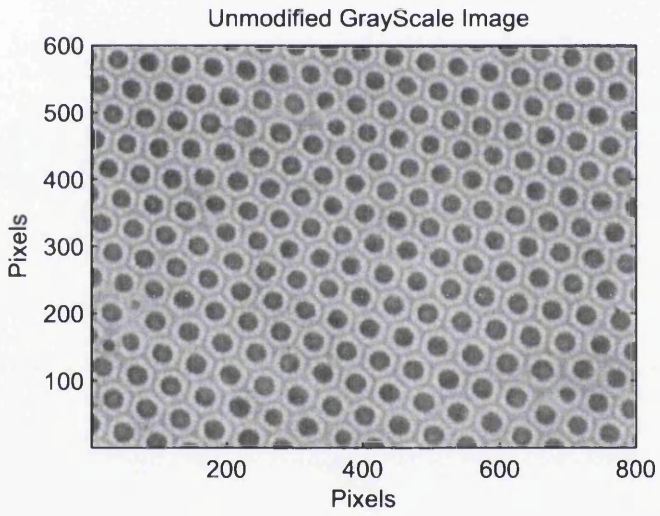

Figure 4.6: An original grey scale image

Each pixel in the image is now represented in the array, as a number between 0 and 256, representing brightness. 0 being black and 256 being white. Next, the pores must be distinguished from the background surface. Since there may be a change in topography over the whole image, and therefore changes in contrast, the image must be split into sections. The distribution of brightness in each section is then analysed.

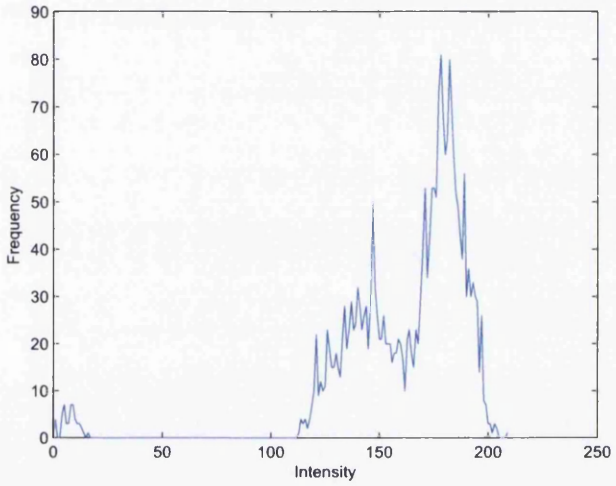

Figure 4.7: Plot of the frequency of occurrence of brightnesses in an image section

In most sections two distinct noisy peaks are observed in the intensity distribution. One is representative of the pore, the other the background. In order to distinguish the cut-off brightness that represents a pore from the background, a double Gaussian function is fitted to the distribution data 4.1.

$$f(x) = a1.exp-((x - b1)/c1)^2 + a2.exp-((x - b2)/c2)^2 \qquad (4.1)$$

The cut-off between the brightness of a pore and the background is then calculated from the minima in the fitted function.

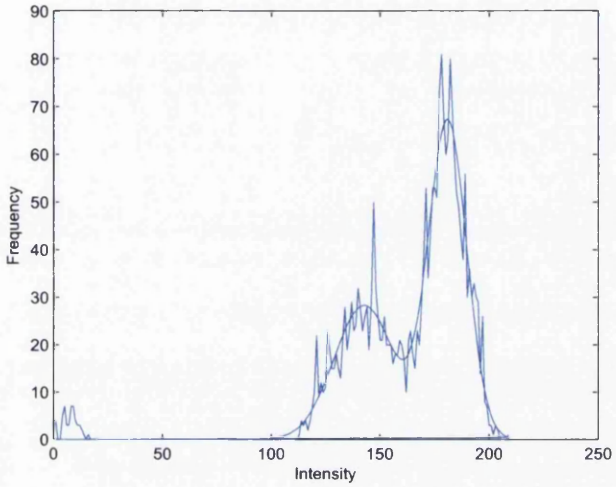

Figure 4.8: Double Gaussian fit

In some sections of the image, the fitting algorithm doesn't fit the data correctly (see figure 4.9) and a cut off point cannot be created from the fit. This situation is distinguished by the inability to find a turning point in the fit.

In this situation, an alternate route must be taken, to finding the turning point. Firstly the un-correct fit, is subtracted from the original data. This should leave behind, the peak that was not fitted successfully (figure 4.10). Which can now be fitted (figure 4.11). A single Gaussian function is then

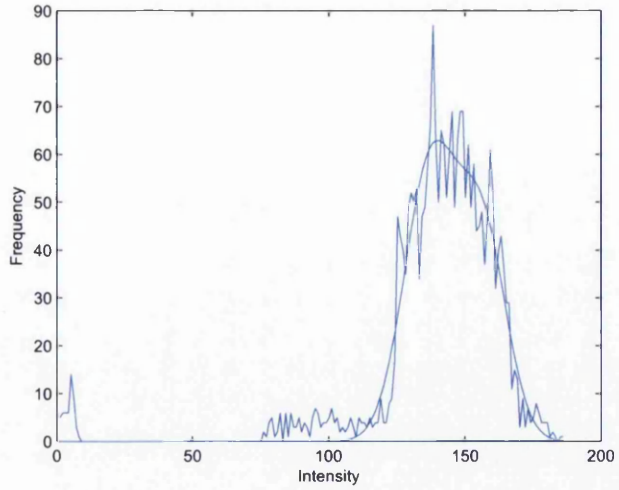

Figure 4.9: Least squares resolving only one peak

fitted to this new data. The overall fitted function is then the sum of both of these functions and a turning point and hence a cut-off intensity can now be found in this function.

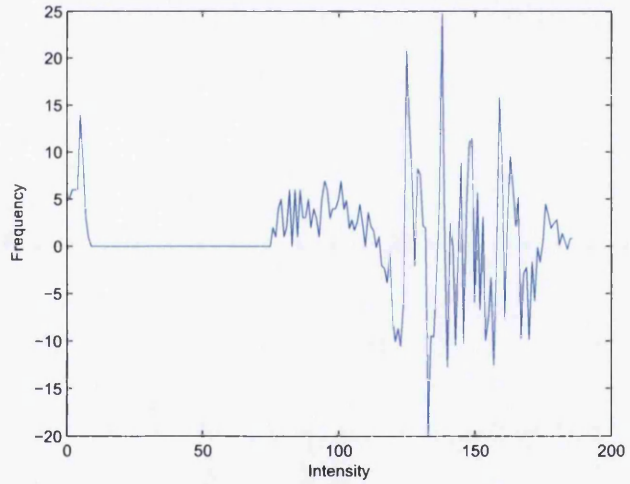

Figure 4.10: Remaining peak previously fitted unsuccessfully

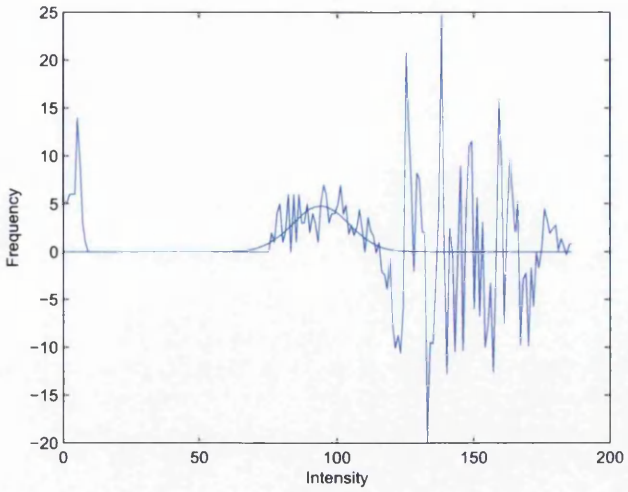

Figure 4.11: Fit to the subtracted data

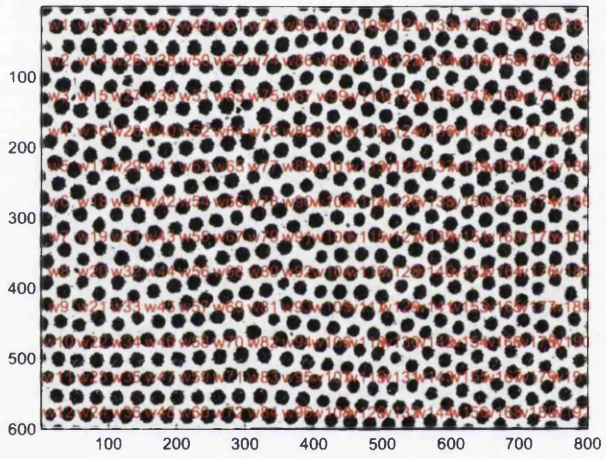

Figure 4.12: Black and white interpretation of image with each window labeled for analysis

If after applying the above technique to a section a cutoff intensity still cannot be found then this error is logged. When an attempt has been made

to calculate a cutoff for all sections of an image, an algorithm is set up to search for sections surrounding the sections with errors. The cutoff of the sections with errors is now approximated as the average of the cutoffs of the surrounding sections. This is obviously less accurate at the boundaries where a section has less neighbours. An error threshold is also set such that if the number of errors per image exceeds this threshold value the image is logged as void.

4.0.5 Finding Pores

The next stage of the algorithm uses the cutoff points found in each section previously to distinguish pores within the image from the backgrounds. Each section is searched for points with brightnesses lesser than those calculated for that image section in the previous function. A pore is distinguished from noise by categorizing a pore as part of the section with a number of successive intensities, below the cutoff intensity, in greater propensity than a critical value.

4.0.6 Location Of Pore Centres

A boundary finding algorithm is now employed to trace the boundaries of the pores. In order to assess the order of the film, the location of the pore centres must be known. Since the pores are not perfectly hemispheric, approximate

circle equations must be used for each pore. A least squares approach is adopted to fit best fit circles to the pore boundaries. Approximate circle centres and diameters can then be assigned to each pore in an image.

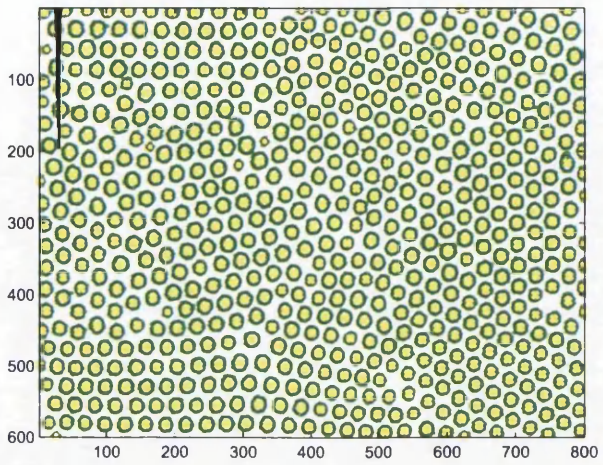

Figure 4.13: Interpretation of an image with pores approximated as circles

4.0.7 Voronoi Constructions

A Veronoi polygon construction can now be constructed by drawing bisectors though all of the lines that connect one pore centre to another. The polygons that this procedure produces are then the smallest convex polygons surrounding any given pore.

The Voronoi diagram allows an analysis of the ordering in a structure to be obtained. The number of sides of each polygon or 'conformation', is

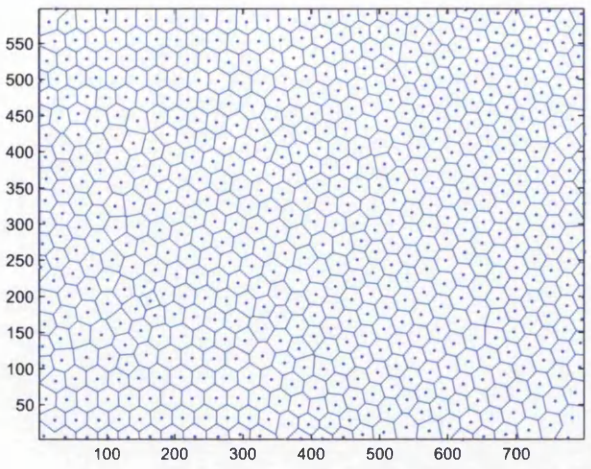

Figure 4.14: A Voronoi Polygon construction of the same image

the number of nearest neighbours the circle centre and therefore pore has. In a perfect hexagonal pattern every point will have six nearest neighbours, hence the probability of a conformation of 6, or P_6 is equal to 1. Thus, by extracting the probabilities of all present conformations from the image, an order parameter can be extracted by means of calculating the conformational entropy.

$S_{con} = -Pn \sum ln(P_n)$

In a perfect hexagonal structure $P_6 = 1$ and therefore $S_{con} = 0$. The higher the deviation from a conformational entropy of 0 the less ordered a structure, i.e. a bigger spread in possible conformations.

The whole image analysis routine is summarized by

The image analysis routine can also be used to gather an estimate of

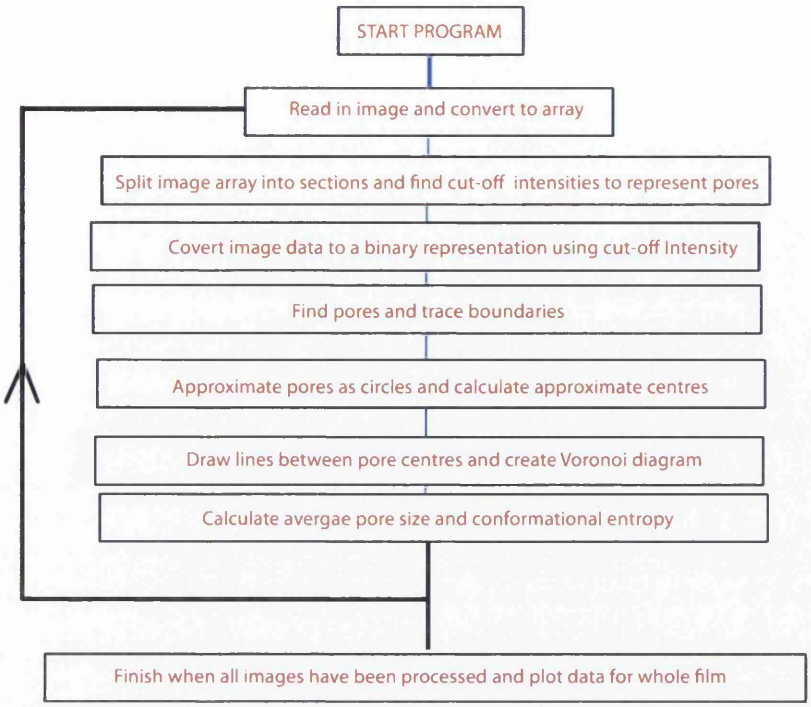

Figure 4.15: Flow chart for image analysis routine

the total deposited condensate during a growth experiment. This can be achieved by counting the pores in each image. From here an estimate of the density of condensate can be arrived at by assuming that the pore sizes in the film resulted from the deposited water droplets(condensate), when they had their maximal size, so from the average pore size an average radius of the deposited droplets can be ascribed. In order to then calculate the total deposited condensate, radial symmetry can be assumed. That is, in an annulus whose thickness is given by the size of the image the condensate density is constant. The total deposited mass is then given by summing through all of these from the edge inwards, and can easily be calculated at

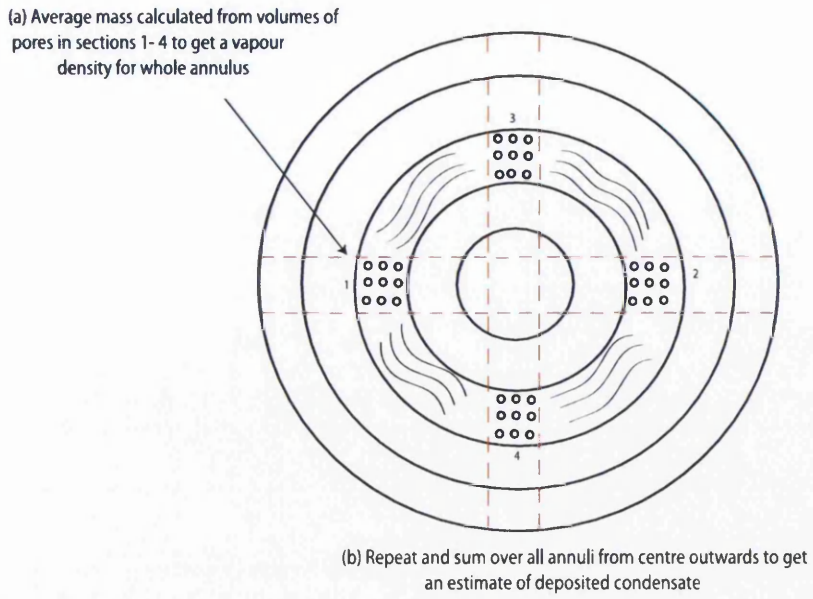

Figure 4.16: Pictorial representation of method to determine deposited condensate mass

the end of running through all the data. This then allows some comparisons to be made between results from the numerical modelling and experiments. The method described is depicted in figure 4.16.

4.1 Area Analysis

In order to make assessments of the evolution of the area of a solution drop during experiments, a program was written in Matlab, to analyse a movie of the solution area. This was achieved via the use of a Graphical User Interface (GUI) in conjunction with user interface controls (ui-control graphics objects). Put simply, this facilitated an analysis of a movie of an evaporating droplet, in a frame by frame manner. In the recorded movie, a length scale was inherent, such as to then create a length scale in images created from the movies. The length scale could be set just by defining the distance in pixels, between a 1cm spacing in the length scale object.

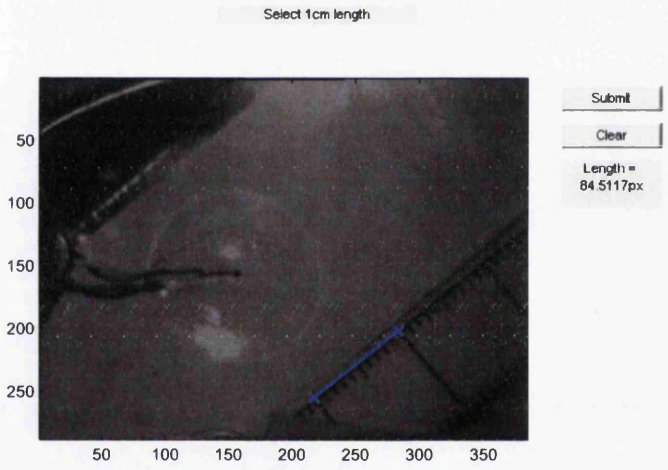

Figure 4.17: Using GUI to find areas of evaporating solution

With the length scale now specified (figure 4.17), the perimeter of the solution drop is then traced by the user.

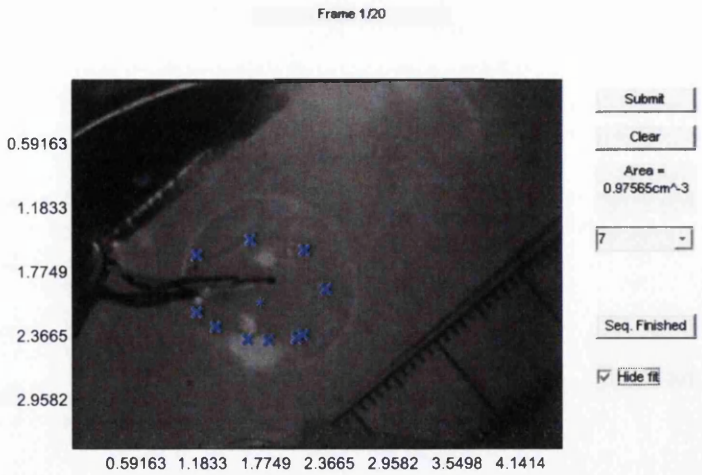

An average of the perimeter coordinates, is then calculated, in order to assume an origin coordinate for an r, θ axes. A plot is then made for the size of a radial vector, between the origin and the perimeter points, inputted for the relevant angles, relative to an arbitrary axes. A radial fit is then used to give a function $r(\theta)$ to represent the solution drop.

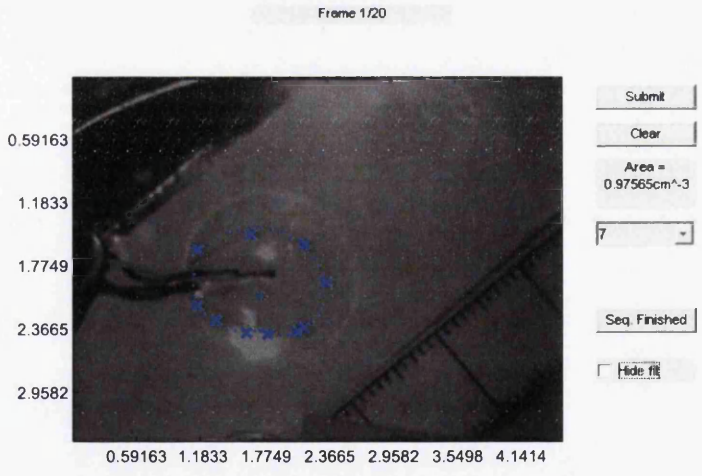

The function can then be integrated from 0 to 2π radians, to deduce the

area of the solution in the given frame.

Chapter 5

Experimental Results

This chapter presents the experimental results obtained, which will be discussed in subsequent chapters. Data which has been repeated is summarised in order to present it in a concise manner. Results concerning the use of the image analysis technique, previously described, to assess radial order and pore size distributions shall be presented firstly.

5.1 Order Analysis

Breath figure structures were cast in stagnant conditions at different relative humidities, using the technique previously described. Images of the produced film's surface structure were obtained using an optical microscope in conjunction with a micromanipulator unit and CCD camera. Sets of four films were analysed at each humidity in order to assess reproducibility. Each film was

analysed in two radial directions, backwards and forth from the approximate film centre. Each new image corresponds to a step of approximately 263 μm across the sample. Using the image analysis techniques previously described approximately one thousand images were analysed in total.

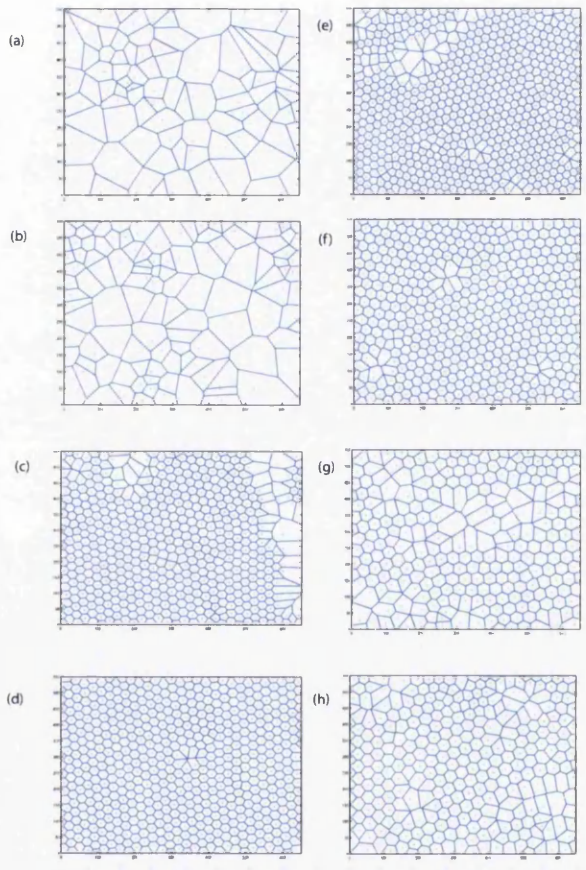

Figure 5.1: Distances relative to centre of sample (a)5mm,(b)4.72mm, (c)4mm,(d)2.6mm,(e)1.8mm,(f)1.2mm,(g)236μm

From the voronoi constructions for each sample (figure 5.1) the conformational entropy at radial distances from the centre can be plotted and a

map of the order across the film can be developed. The plots show the average conformational entropy at the given radial distances from scans across the film in two radial directions .i.e. the average four calculations. The Films created are arbitrarily labelled 1-4, further plots of the corresponding Veronoi diagrams are not included, as they would take up a large amount of space and really only serve as a visual aid. Other plots show the variation of average pore size, and the hexagonal order parameter p6.

5.2 80% Relative Humidity

Firstly results concerning films made when the casting conditions were maintained at ambient temperature and 80% relative humidity are presented. Figures 5.2 and 5.3 show how the average conformational entropy varies from the film centre outwards for each film. The error bars are representative of the spread in the values calculated at each position in each of the four directions across the film.

As can be seen in figure 5.2 the conformational entropy is highest at the edges of the films as expected (the edges of the film often contain visible deposits of polymer (figure 5.3) which seem to perturb ordering of droplets). The profiles across the films however show different behavior in each case. The conformational entropy rises at the centre in the case of film 1 and reaches a minima in the case of film 2. Possible causes of this behavior will be discussed

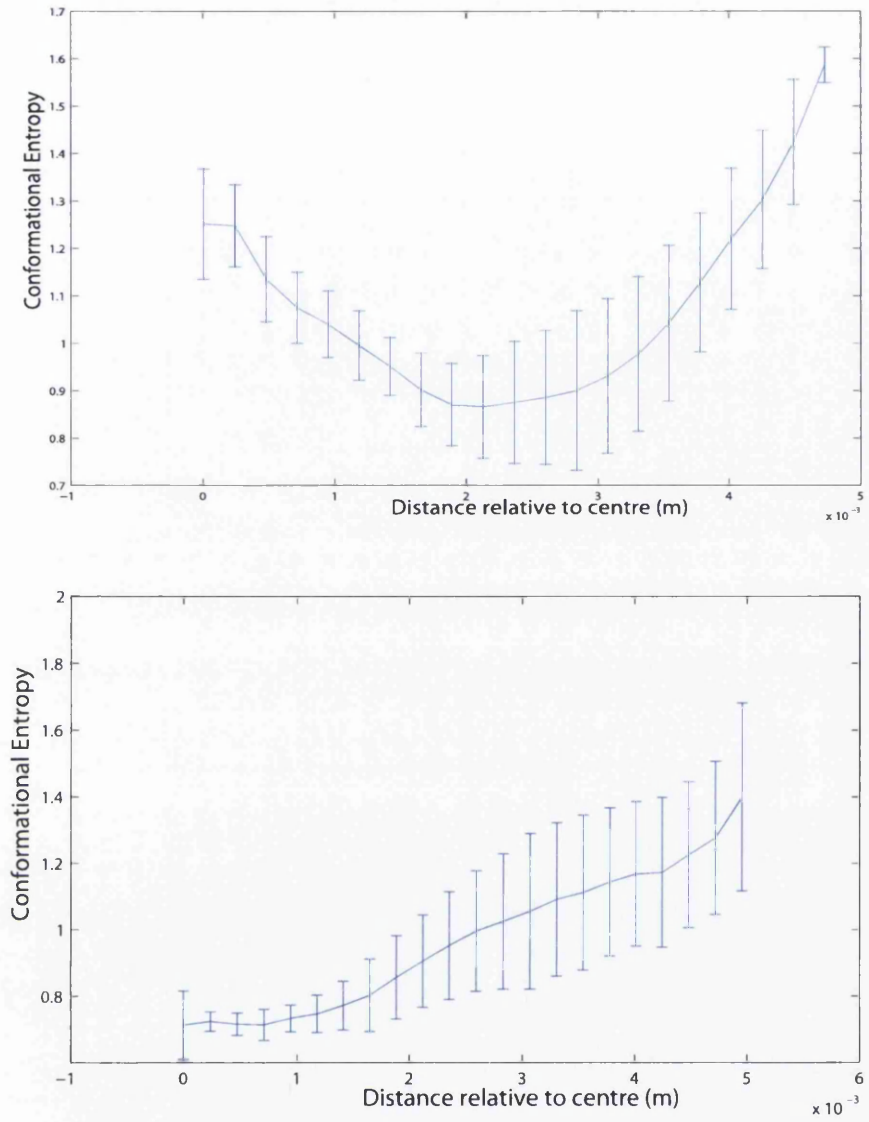

Figure 5.2: Conformational entropy as a function of radial distance for films 1 and 2

in the next chapter. Looking forward to figures 5.4 and 5.5, once again two differing trends can be observed. One profile decays towards the centre of the film and one profile reaches a minima about half way between the edge and

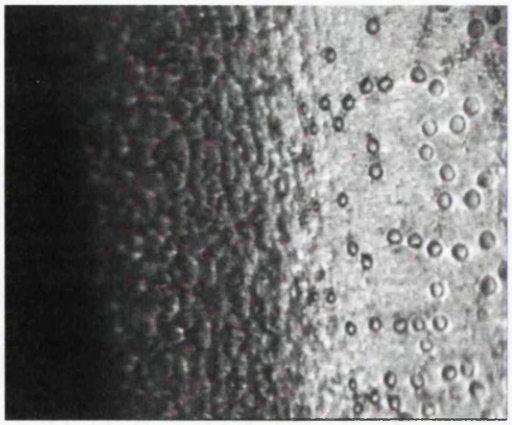

Figure 5.3: Microscope image at edge of film

the centre with a relative increase towards the centre.

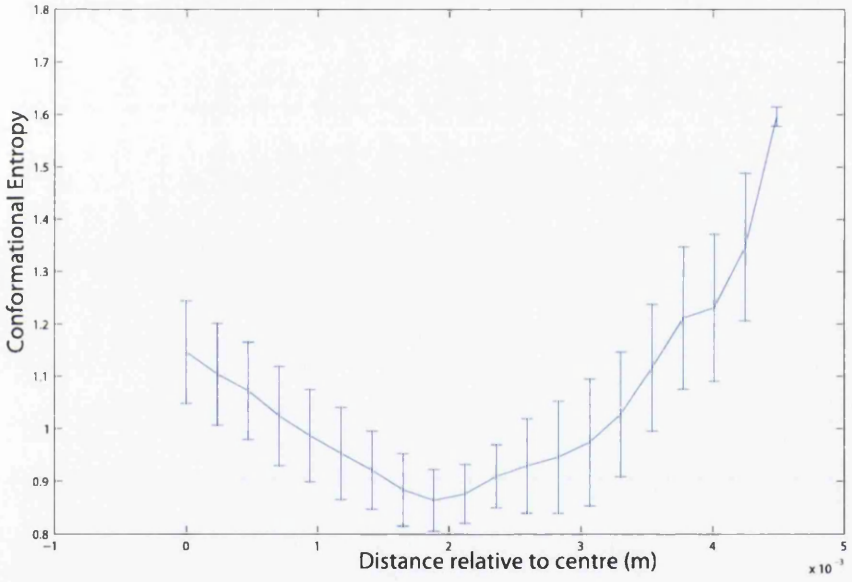

Figure 5.4: Conformational entropy as a function of radial distance for film 3

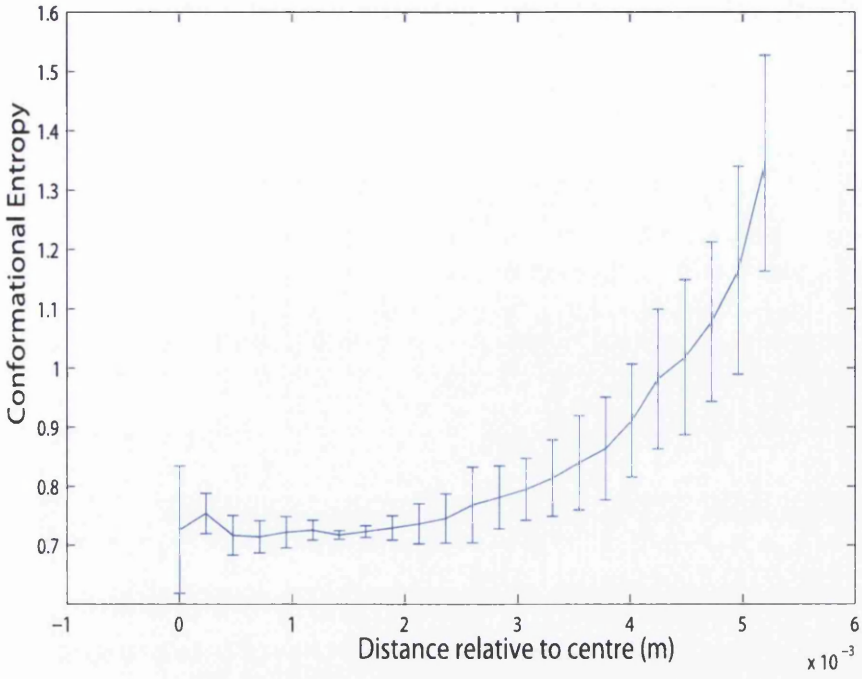

Figure 5.5: Conformational entropy as a function of radial distance for film 4

In figures 5.6 and 5.7 we look at the average pore size profiles across the films obtained from circular fits to the pore boundaries.

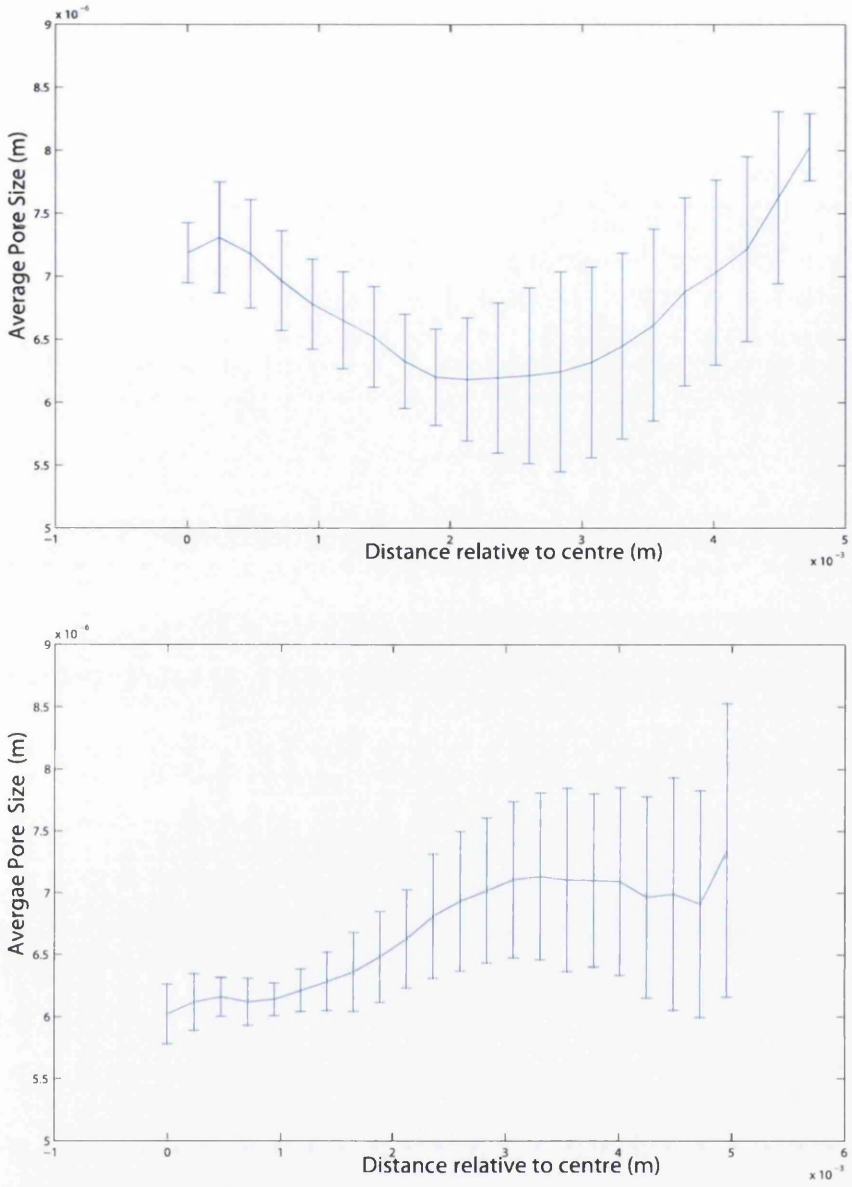

Figure 5.6: Average pore size as a function of radial distance for films 1 and 2

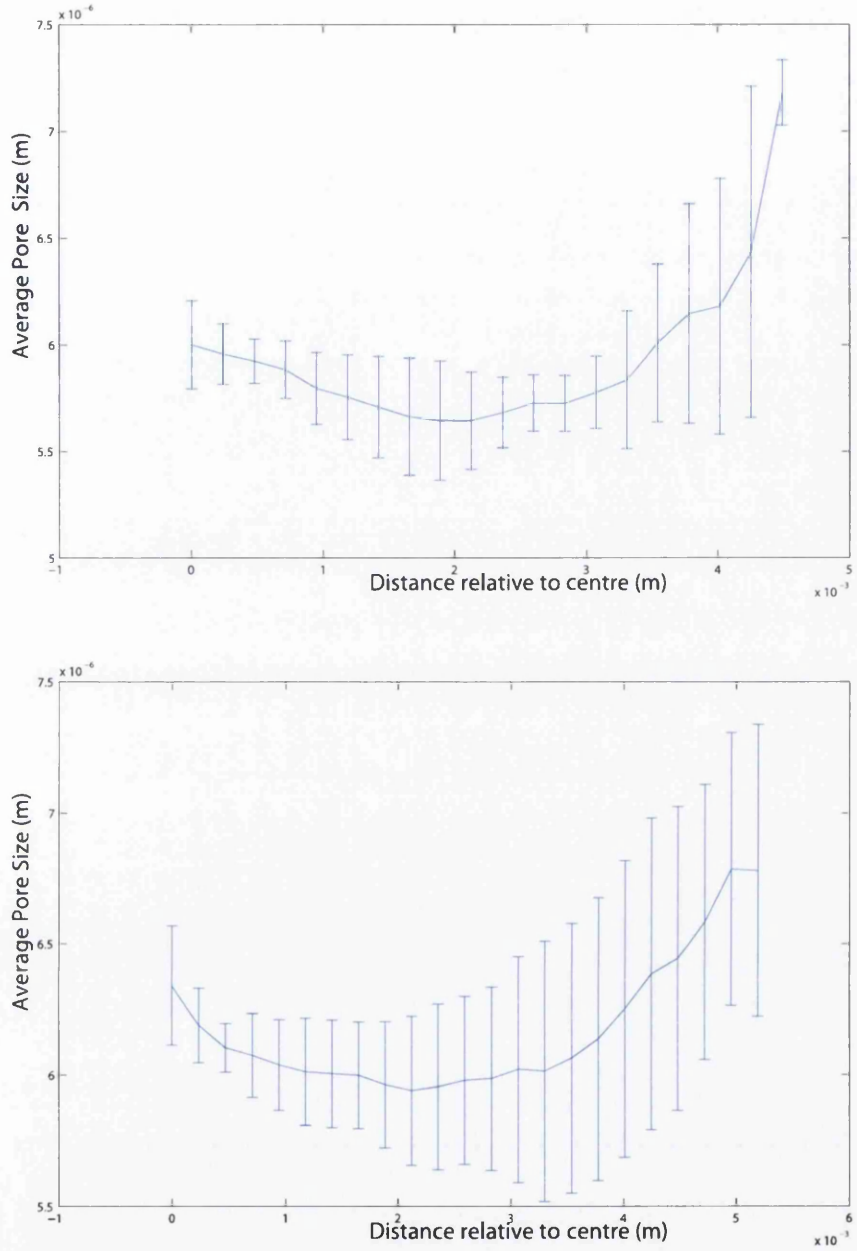

Figure 5.7: Average pore size as a function of radial distance for films 3 and 4

The pore size at the centre of the films is roughly 6 micron for films 2, 3 and 4. The average pore size in the case of film 1 passes through a minima about half way from the edge to the centre which is also roughly six micron however this size increases towards the centre reaching roughly 7 micron. It seems in the case of film 1 that there is a possible correlation between the minima in conformational entropy and also the minimum pore size in the film. The increase in conformational entropy at the film centre is most dramatic in this film and so is the increase in average pore size.

Figures 5.8 and 5.9 display the profiles of the parameter P_6 across the film. This parameter is calculated in order to evaluate the degree of hexagonal ordering. The parameter p_6 generally displays the inverse behaviour of the conformational entropy. Once again films 1 and 3 show a maxima in the degree of hexagonal ordering at the same points as their minima in conformational entropy.

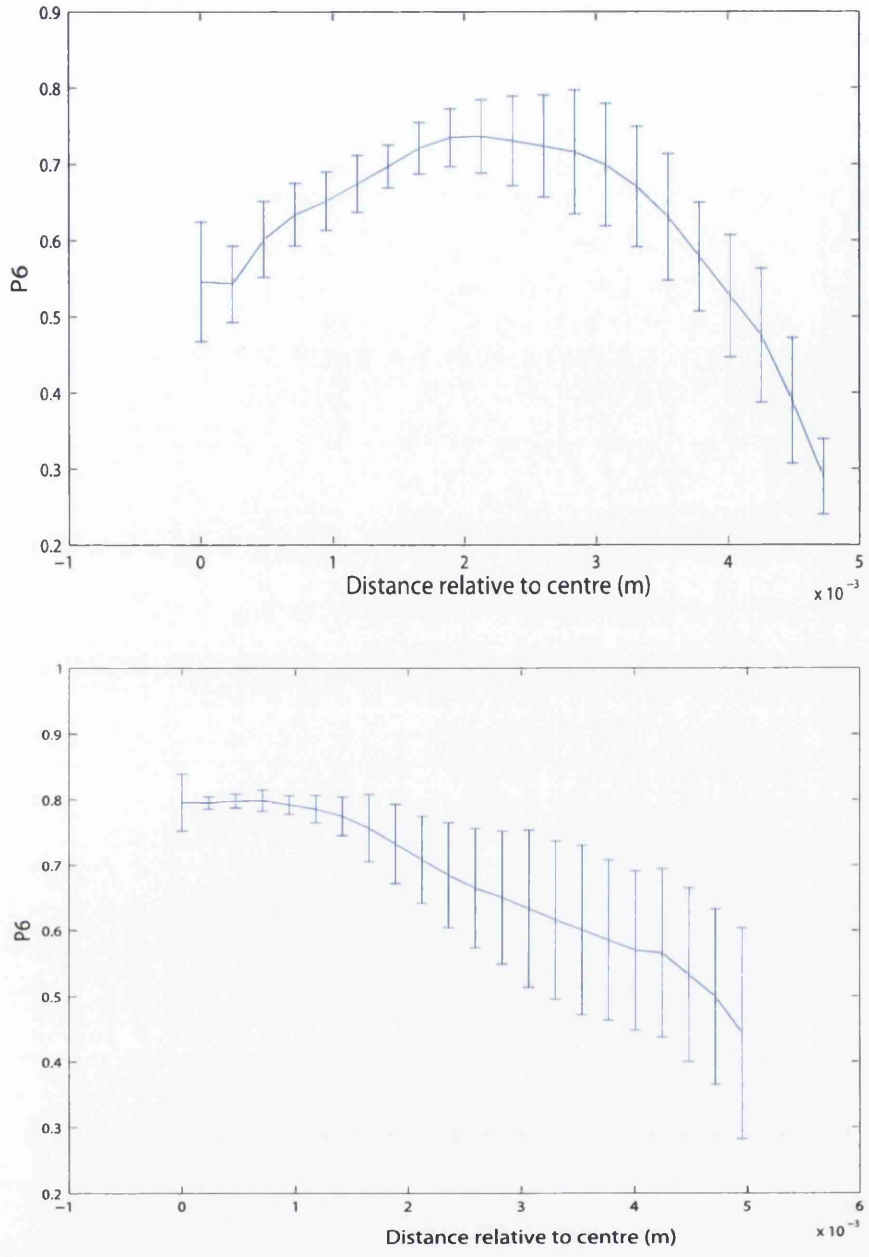

Figure 5.8: Hexagonal order as a function of radial distance for films 1 and 2

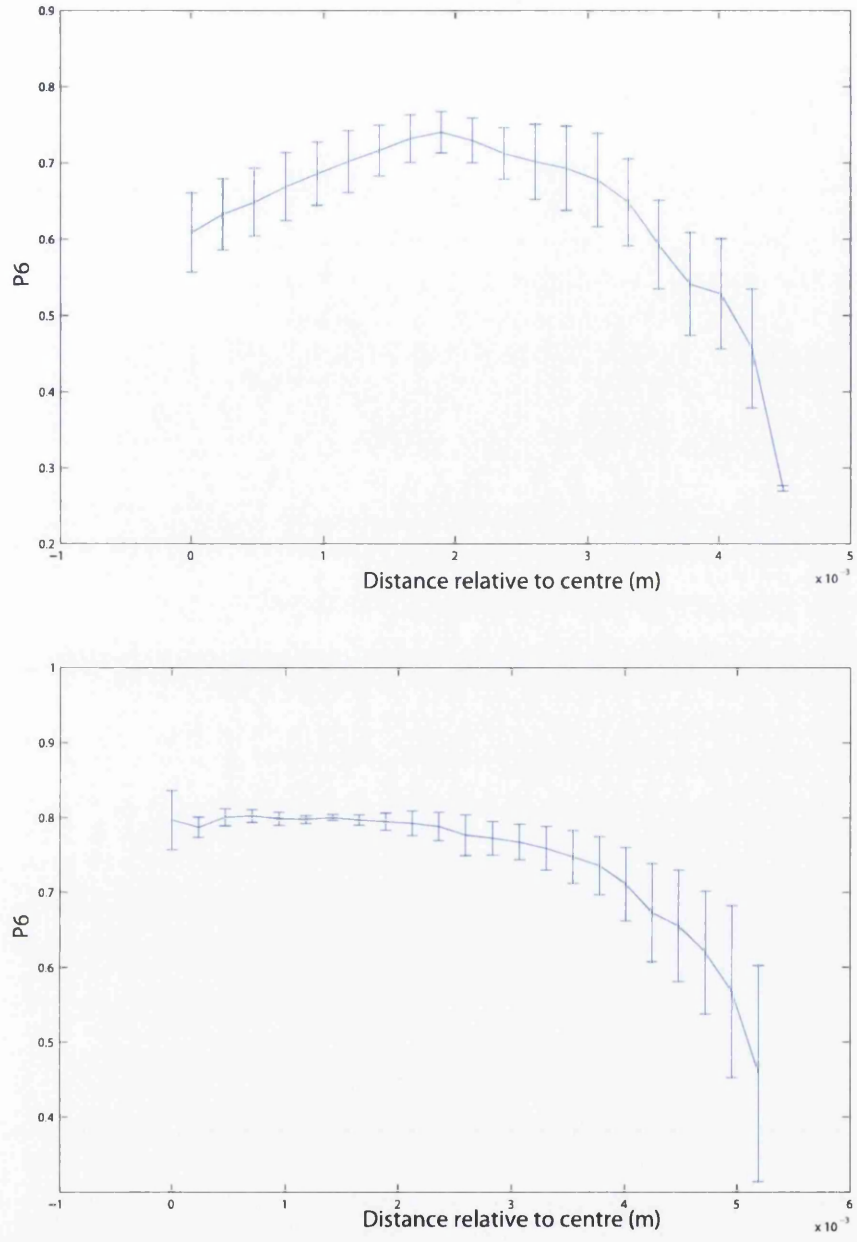

Figure 5.9: Hexagonal order as a function of radial distance for films 3 and 4

5.3 Relative Humidity 85%

The chamber relative humidity is now adjusted to 85% and we look at how this affects the same parameters. It must be noted that during the period in which these experiments took place the average ambient temperature was approximately 3 degrees cooler than the previous experiments. Figures 5.10 and 5.11 show the conformational entropy profiles across the films.

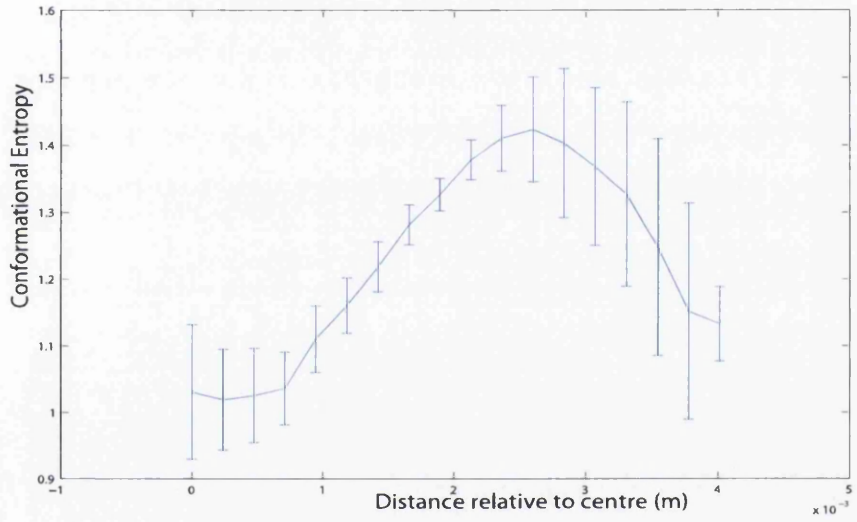

Figure 5.10: Conformational entropy as a function of radial distance for film 1

In film 1 the maxima in average conformational entropy is not at the film edge, this is the first instance of this behaviour so far. The maxima is reached just over half way through the film, this subsequently decreases towards the film centre where the parameter reaches a minima.

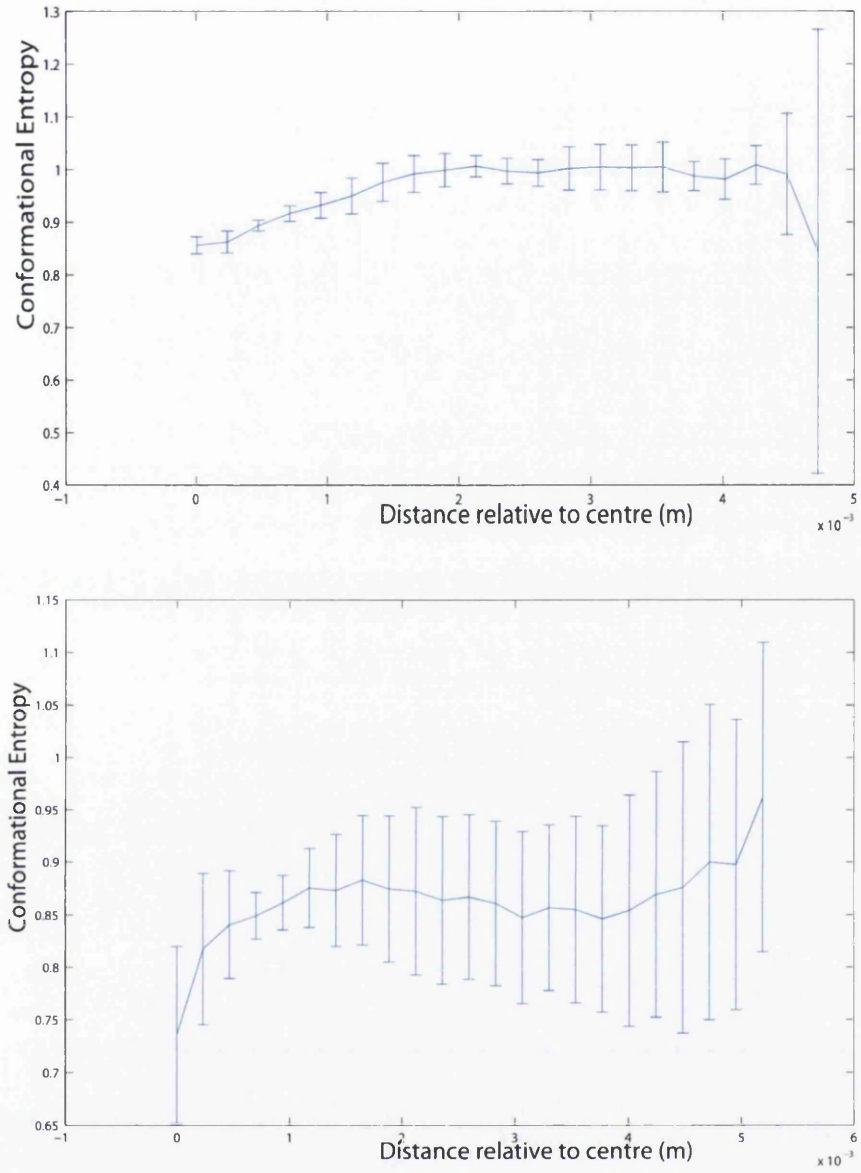

Figure 5.11: Conformational entropy as a function of radial distance for films 2 and 3

In figure 5.11 it can be seen that films 2 and 3 show the most even spreads in conformational entropy across the film surface so far. The error bars are also smaller indicating that the similarity in these parameters radially is also greater.

Next we look at how this increase in relative humidity affects the average pore size. Figures 5.12, 5.13 and 5.14 show the profiles of average pore size across the films.

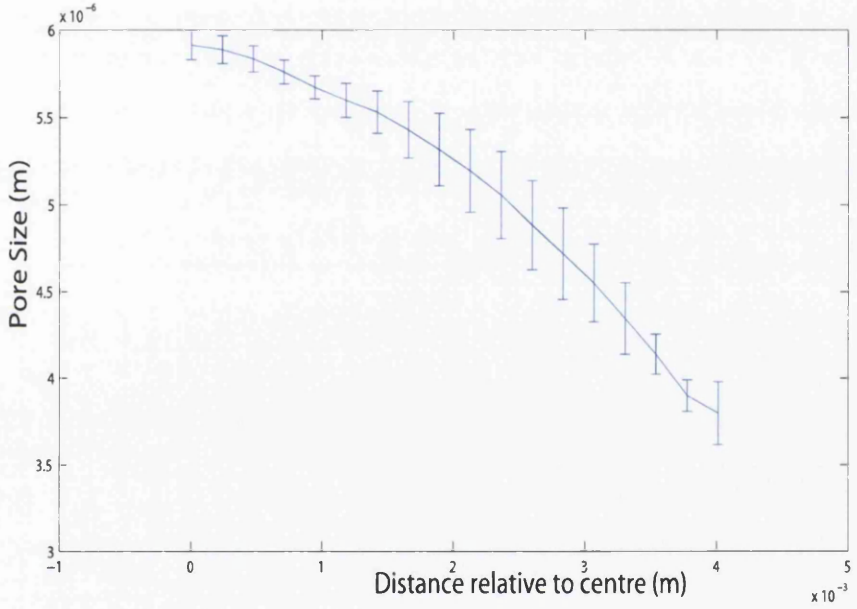

Figure 5.12: Average pore size as a function of radial distance for film 1

It can be seen that at this humidity, the pore size generally increases towards the centre of the films. The pore size directly at the centre of the films is quite different in each film ranging between 4 and 6 micron. The

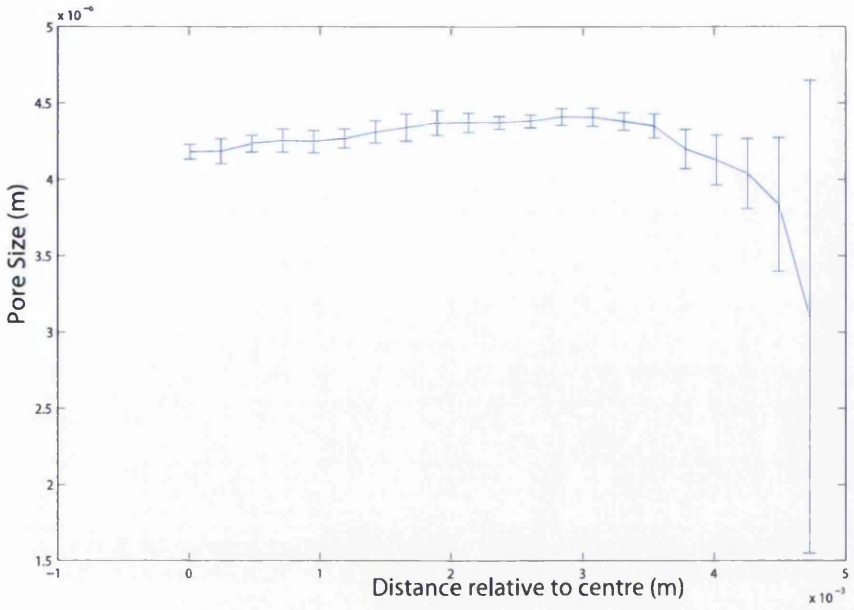

Figure 5.13: Average pore size as a function of radial distance for film 2

average pore size profile for film 2 is the flattest of all and also has the smallest error bars once again indicating that the average pore size at each location is reflected in the film radially. This film also displays the smallest pores at the centre. The profile of pore size is extremely similar to the profile for conformational entropy of the film which could indicate a deposition related ordering effects. Film 3 (figure 5.14) shows a larger spread in average pore size across the film despite having a flat profile in conformational entropy akin to film 2.

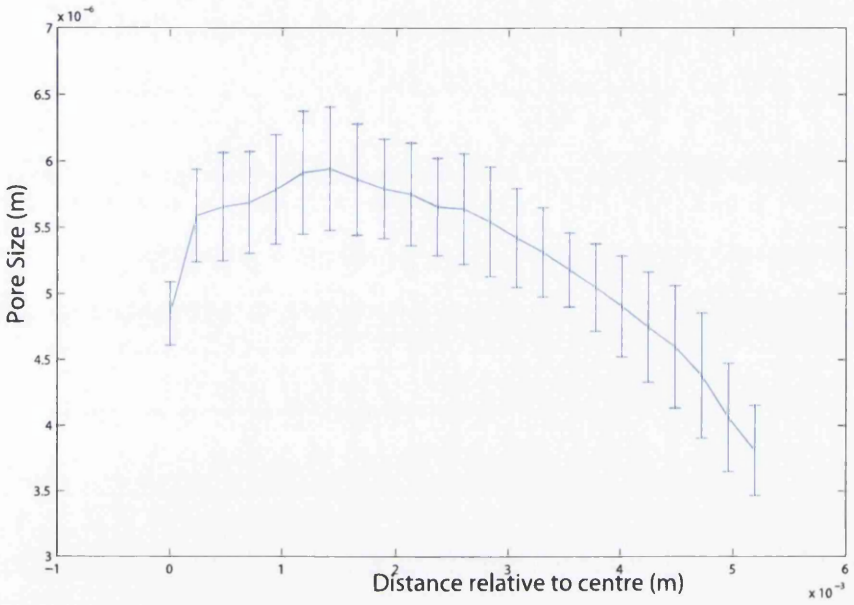

Figure 5.14: Average pore size as a function of radial distance for film 3

Next the results for the hexagonal order parameter P_6 are displayed in figures 5.15 and 5.16.

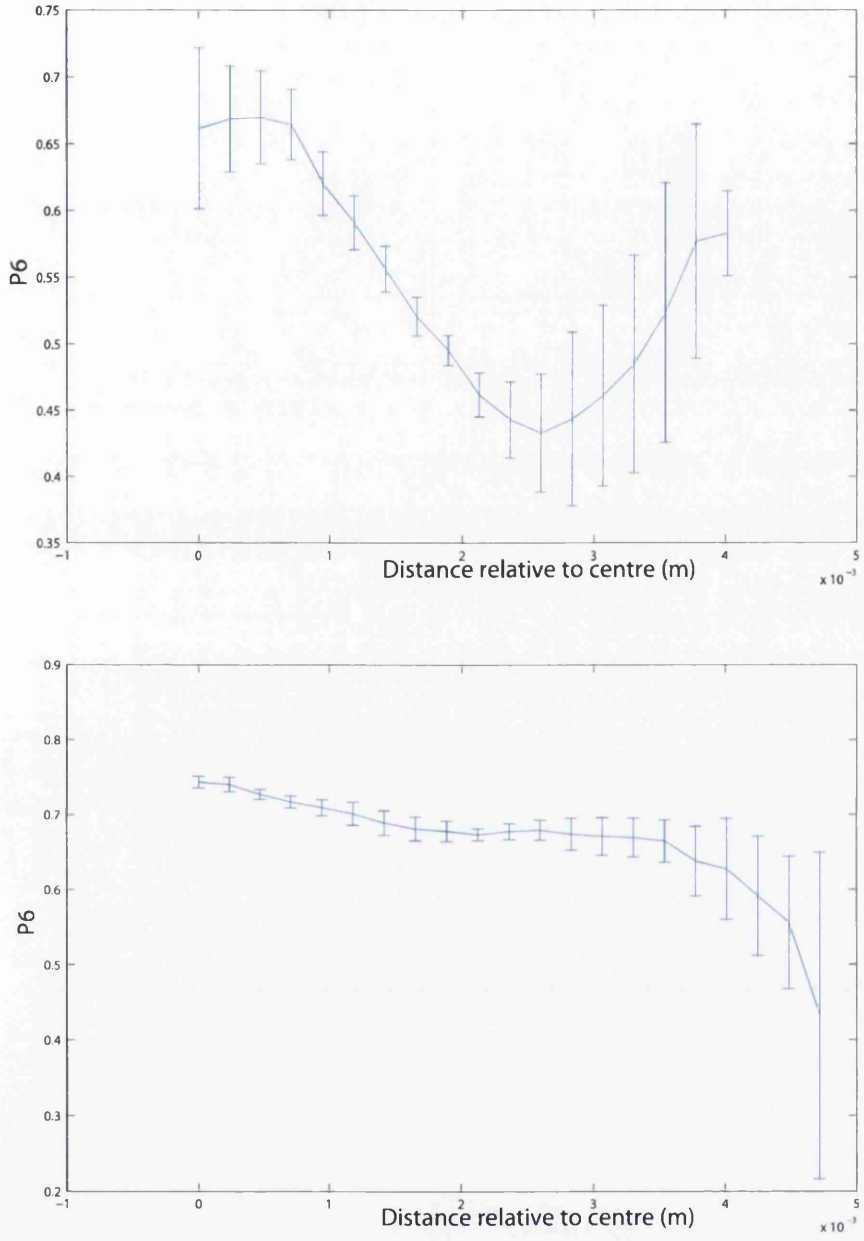

Figure 5.15: P6 as a function of radial distance for films 1 and 2

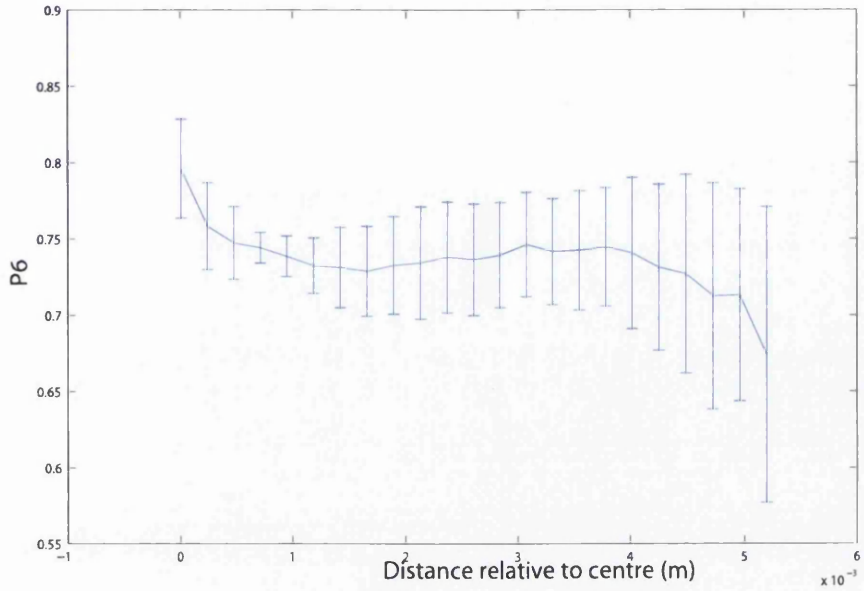

Figure 5.16: P6 as a function of radial distance for films 3

Once again it can be seen that the parameter p_6 follows approximately the inverse behavior of the conformational entropy.

5.4 Relative Humidity 75%

Now we look at the effect of lowering the relative humidity on the profiles for the same parameters. The average ambient temperature for these experiments was approximately the same as that at 85% relative humidity. Figures 5.17, 5.18 and 5.19 show the conformational entropy at given distances across the films.

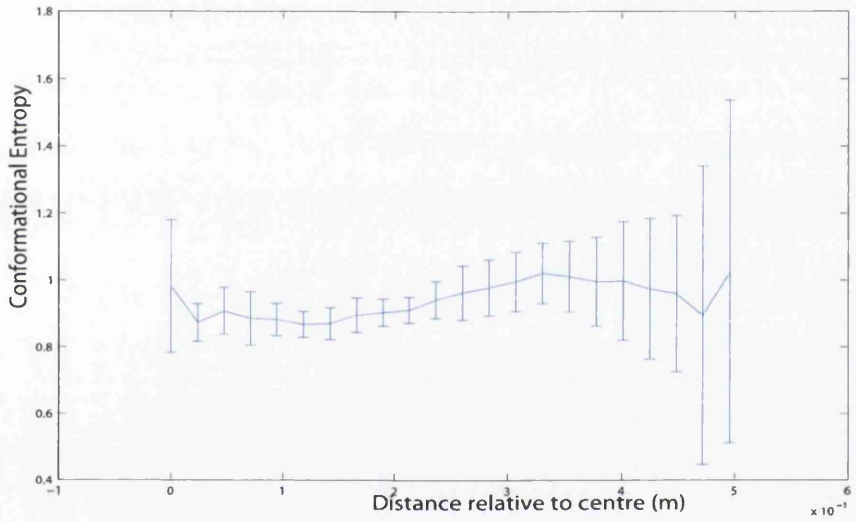

Figure 5.17: Conformational entropy as a function of radial distance for film 1

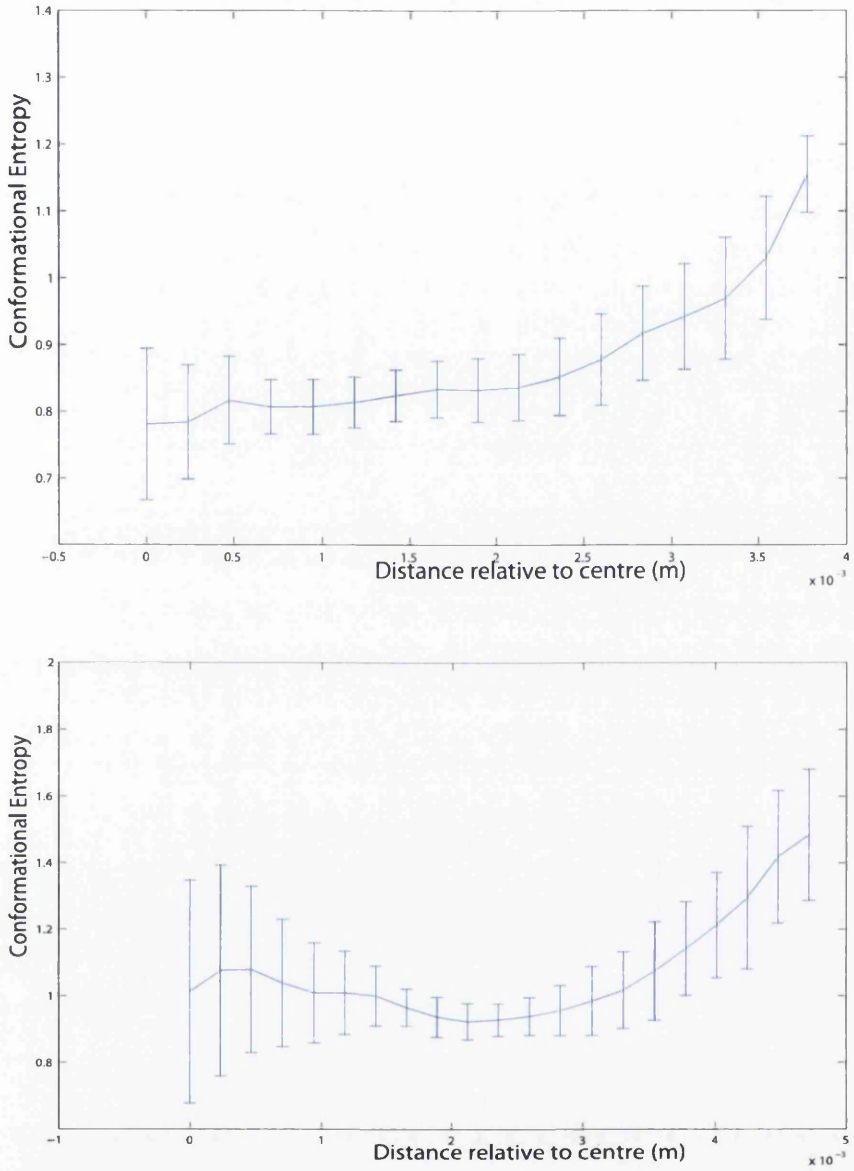

Figure 5.18: Conformational entropy as a function of radial distance for films 2 and 3

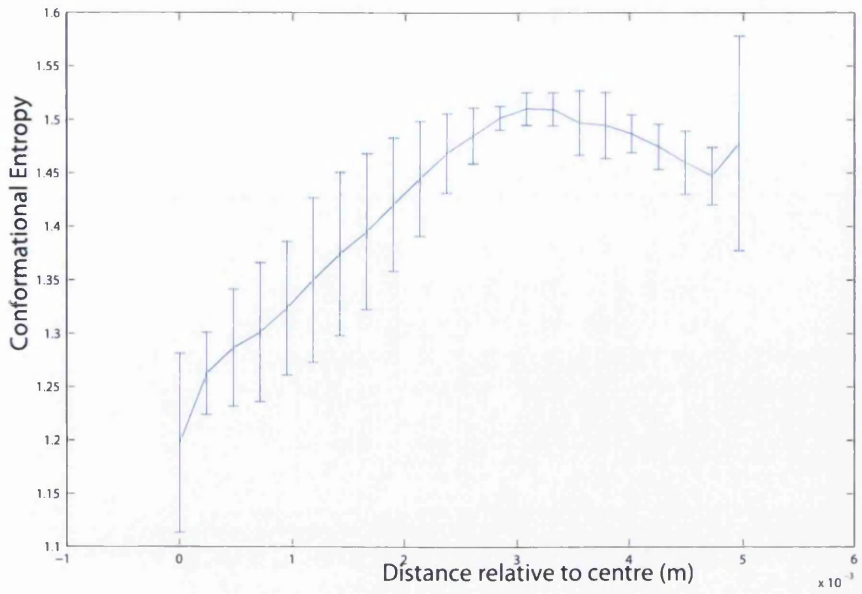

Figure 5.19: Conformational entropy as a function of radial distance for film 4

At this humidity it can be seen that generally the highest conformational entropy occurs at the edges of the films. Film 1 has the flattest profile of all with films 2 and 4 having minima and maxima roughly half way from the edge and the centre. The error bars at these minima and maxima are also the smallest with respect to the others in each film, this could possibly indicate the occurrence of some radial ordering effect.

Now we look at the effect of lowering the relative humidity on the average pore size. Figures 5.20 and 5.21 display the average pore size in each film cast at this relative humidity.

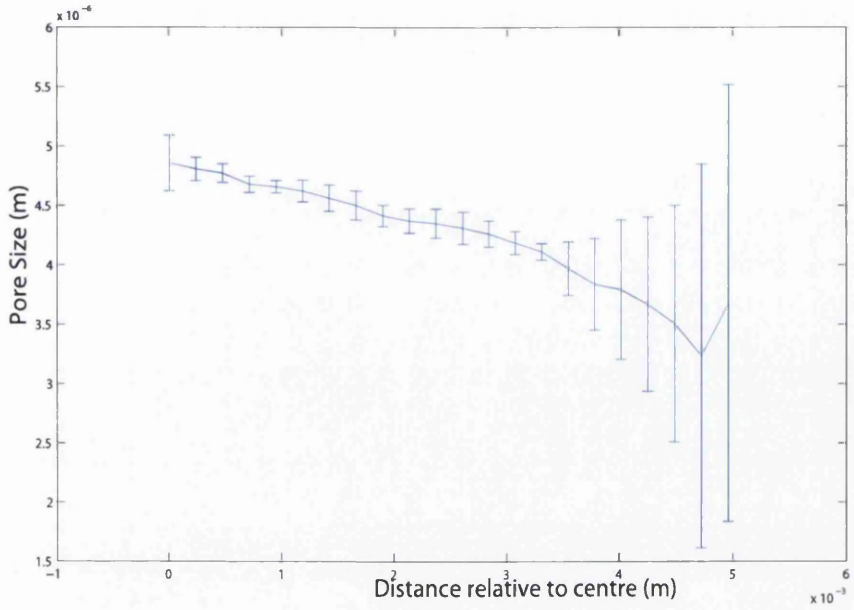

Figure 5.20: Average pore size as a function of radial distance for film 1

It can be seen that at this relative humidity the average pore size at the film centre is the lowest of all the films generally between 4 and 5 micron. There is not a general trend in this case for the average pore size radially, sometimes the pore size decreases towards the edge and sometimes it increases. However at the position of minima in conformational entropy observed in film 2, a minima in pore size is also observed and also a minima in the error bars indicating that this is a radial phenomenon.

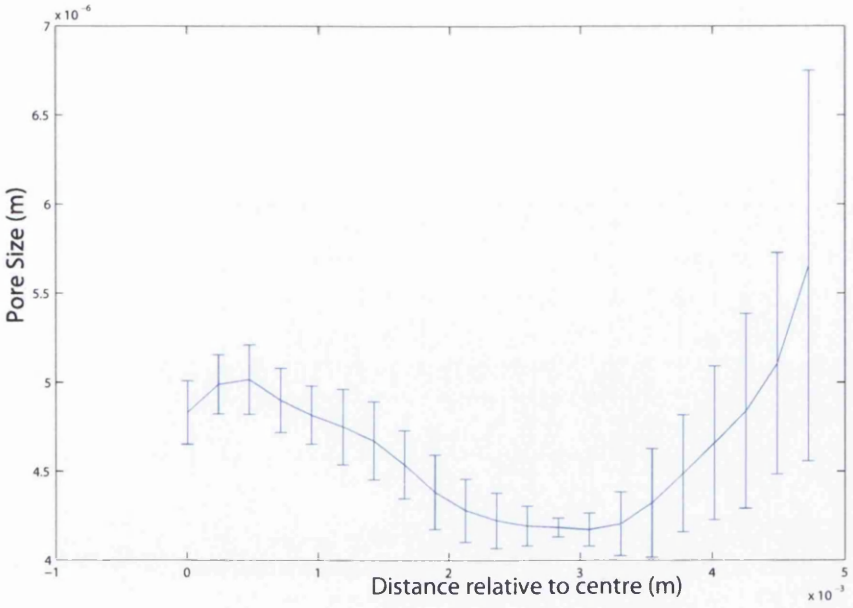

Figure 5.21: Average pore size as a function of radial distance for film 2

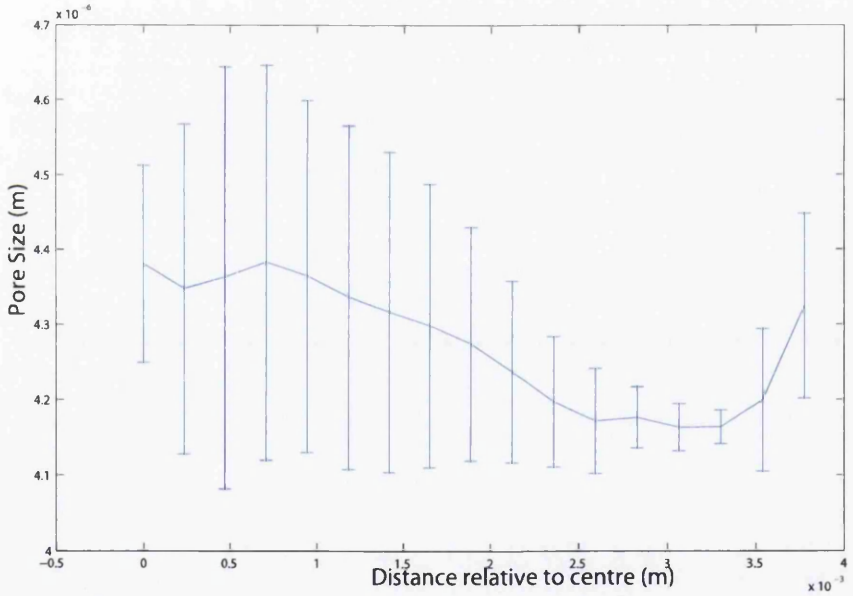

Figure 5.22: Average pore size as a function of radial distance for film 3

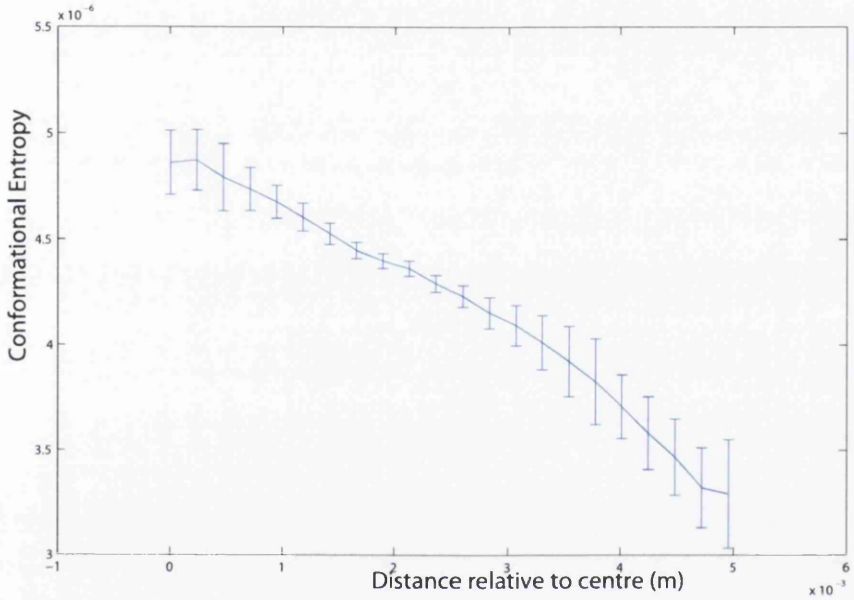

Figure 5.23: Average pore size as a function of radial distance for film 4

Figures 5.19 and 5.20 show the variation of the parameter P_6.

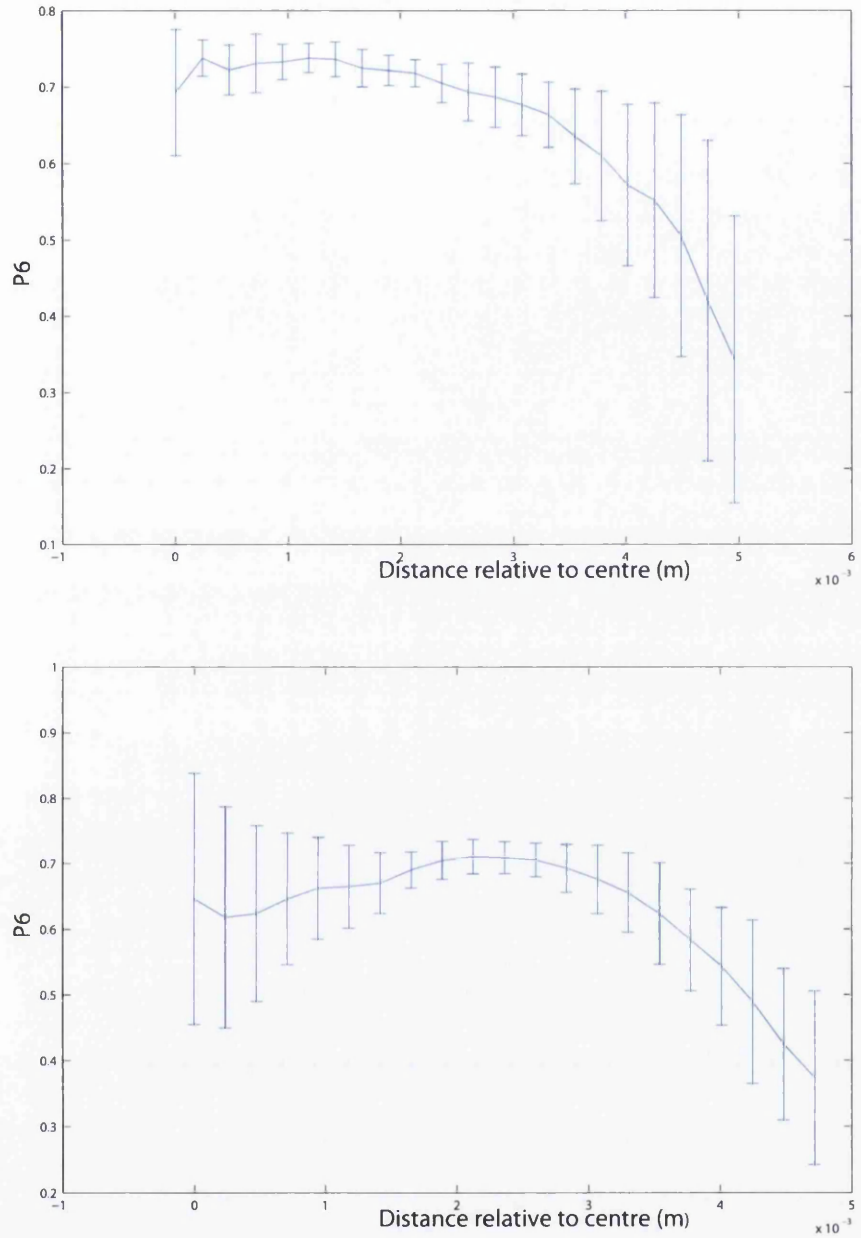

Figure 5.24: P6 as a function of radial distance for films 1 and 2

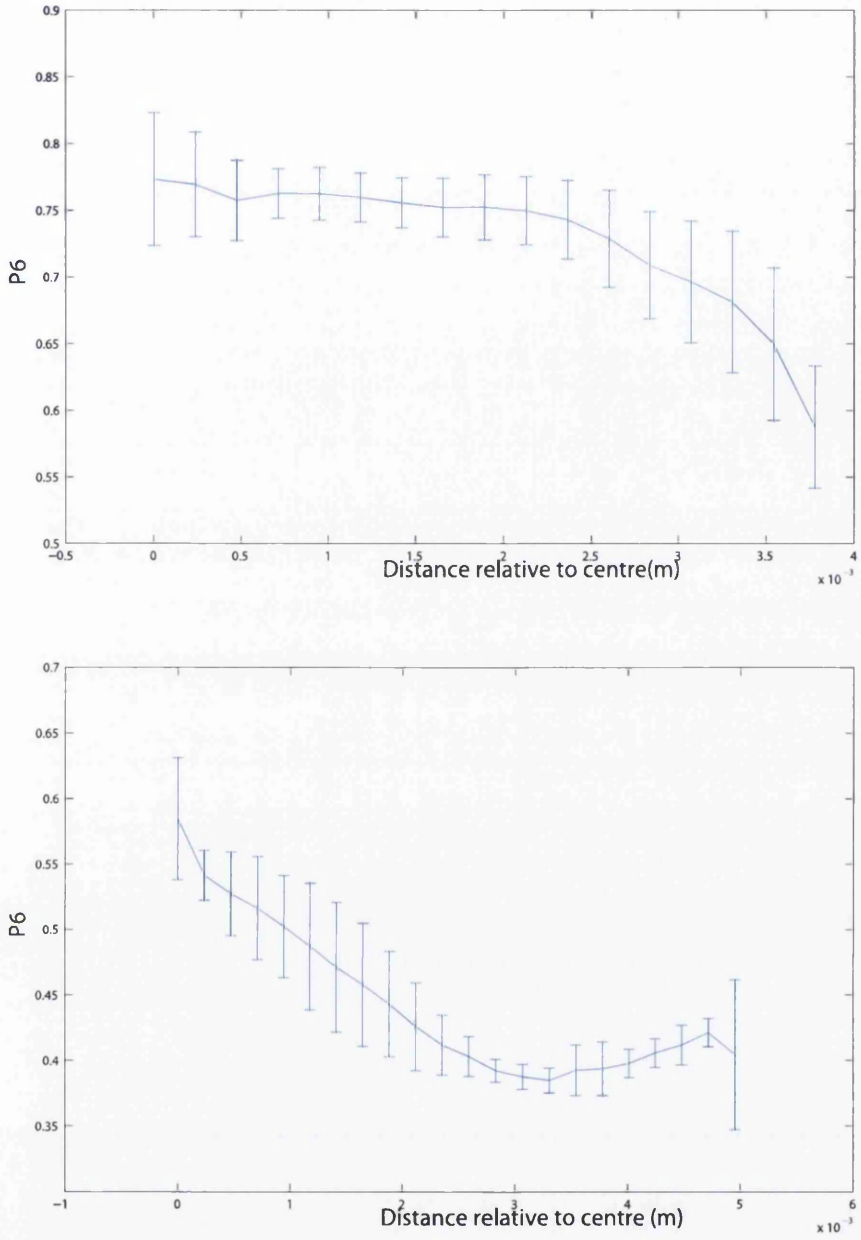

Figure 5.25: P6 as a function of radial distance for films 3 and 4

The parameter P_6 once again shows the inverse behaviour of the conformational entropy.

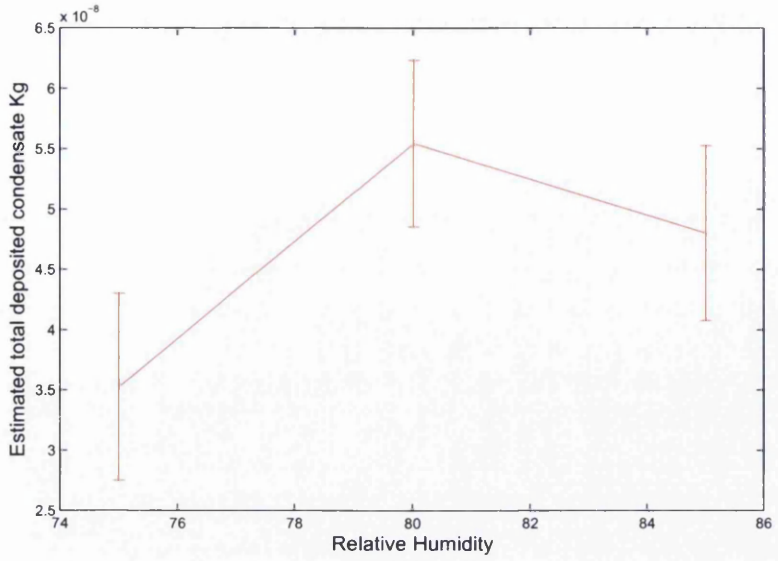

Figure 5.26: An estimate of total deposited condensate at each relative humidity

Lastly using the technique described in the experimental methods section the image analysis program is used to obtain an estimate of the total deposited condensate at each relative humidity, this is shown in figure 5.26. The total deposited condensate is seen to have a maxima at 80% relative humidity, this was actually expected since the ambient temperature was notably higher when carrying out these experiments. This would have inferred a maximal chamber vapour density at 80%.

5.5 Temperature Measurements

In order to provide some justification of the dynamics predicted by the numerical model, temperature profiles were recorded for pure evaporating carbon disulphide and chloroform.

Firstly a 50 μL drop of carbon disulphide was evaporated inside the casting chamber already described. The humidity in the chamber was reduced to below 10%. In this experiment the substrate which is a glass slide is positioned on some ceramic supports positioned on the pan of the mass balance (situation a in figure 5.27). The ambient temperature in this experiment was $23°C$. Figure 5.28 shows the temperature profiles.

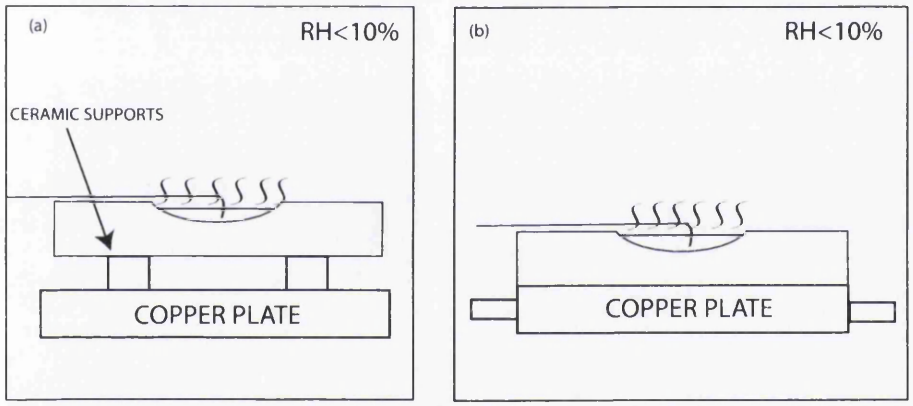

Figure 5.27: Temperature measurements

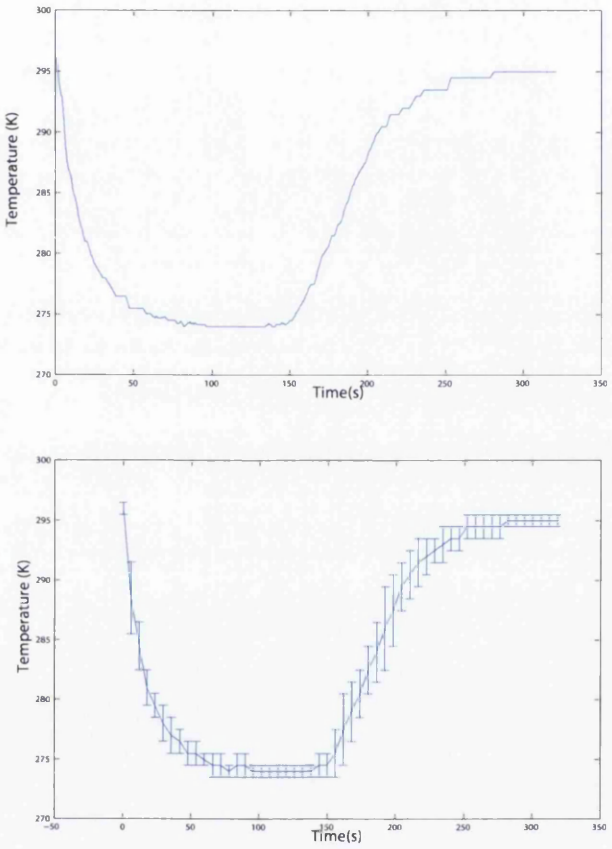

Figure 5.28: Temperature profile for a 50μL liquid drop of carbon disulphide 50μL evaporating in a dry environment with thermocouple in drop and ceramic supports

The same experiment is now conducted with the sample slide placed directly on a cold plate (situation b in figure 5.27) which is maintained at ambient temperature (figure 5.29).

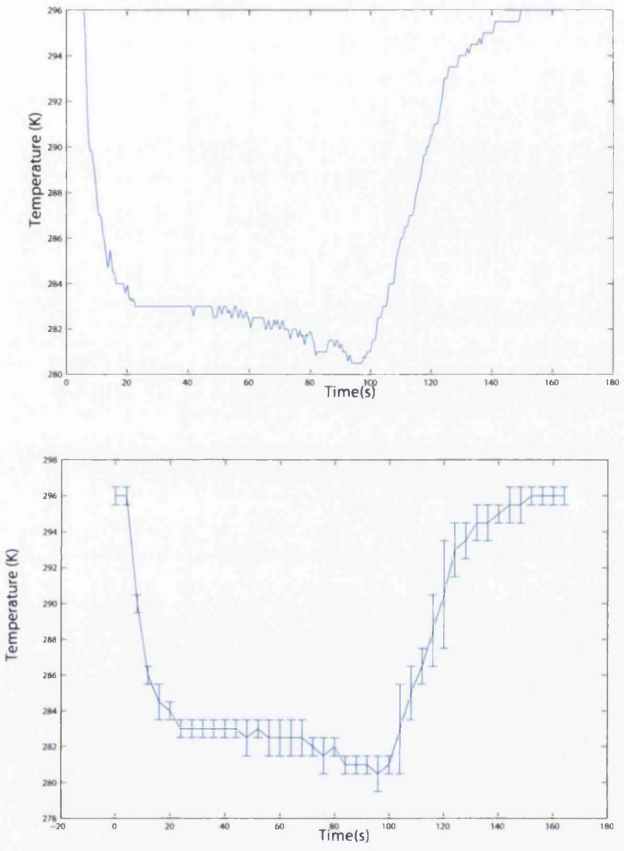

Figure 5.29: Temperature profile for a 50μL liquid drop of carbon disulphide 50μL evaporating in a dry environment with thermocouple in drop with the substrate directly placed on plate

As can be seen the extra conductive heat transfer from the plate has altered the temperature drop significantly. Now the experiments are repeated for Chloroform. Figure 5.30 shows the profiles obtained when performing the experiments with the glass slide directly placed on the cold plate.

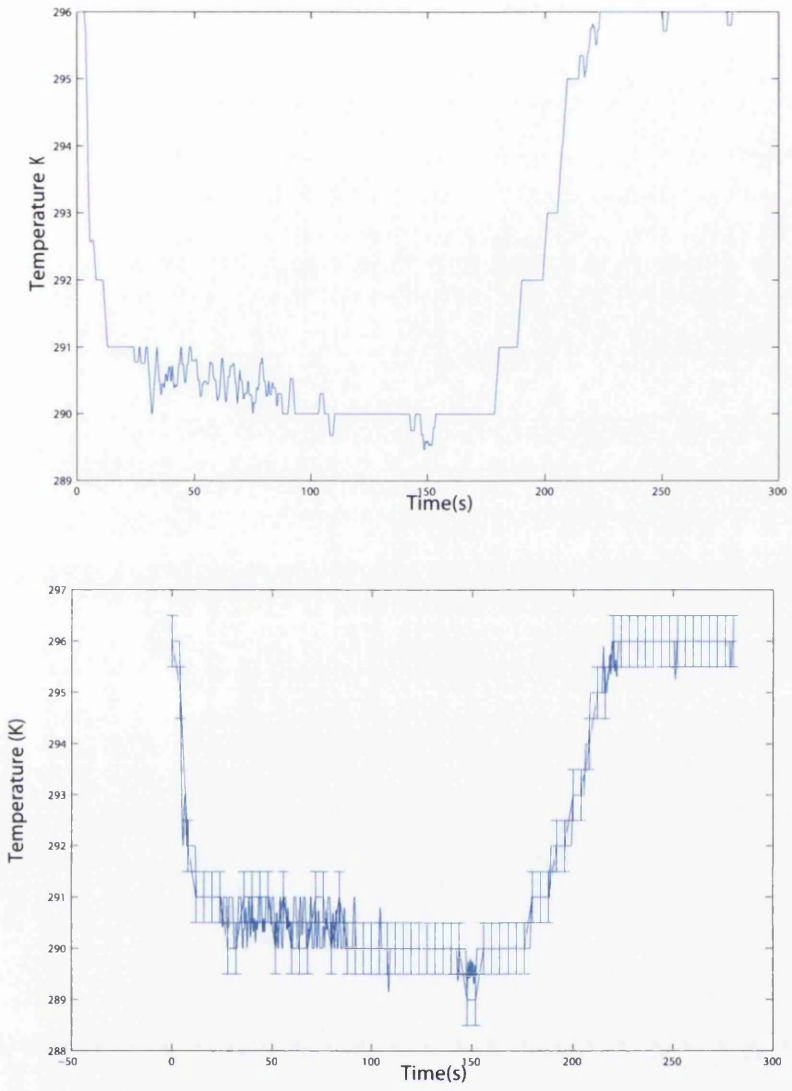

Figure 5.30: Temperature profile for a 50μL liquid drop of Chloroform 50μL evaporating in a dry environment with substrate placed directly on cold plate

And figure 5.31 the profile with the slide placed on ceramic supports.

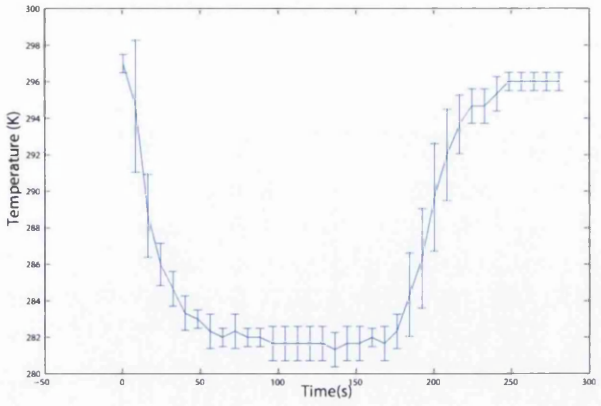

Figure 5.31: Temperature profile for a 50μL liquid drop of chloroform evaporating in a dry environment with ceramic supports

Once again the profiles have been dramatically altered.

5.6 Evaporation rate measurements

Now we look at evaporation profiles for the pure substances. In these experiments the sample slide was placed directly on the plate maintained at ambient temperature, firstly figure 5.32 shows the evaporation profile for chloroform.

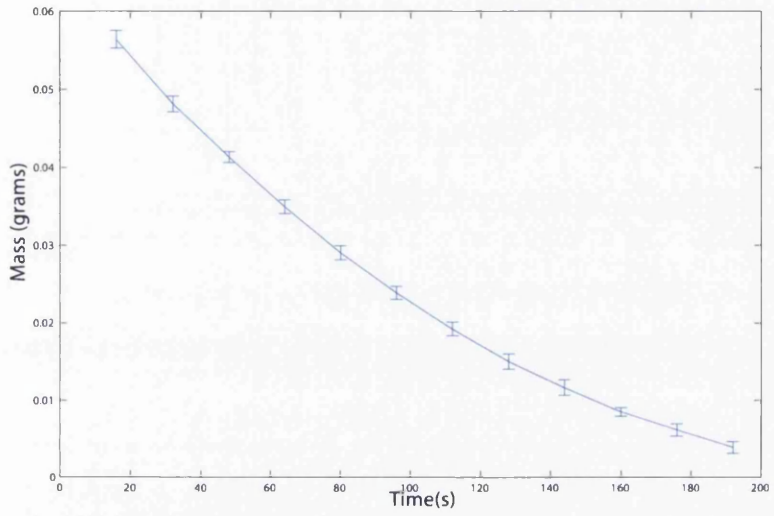

Figure 5.32: Evaporating mass of chloroform with substrate on cold plate

and figure 5.33 the profile for carbon disulphide.

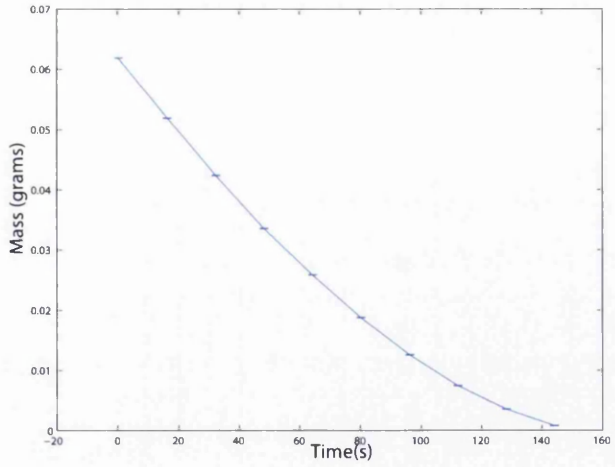

Figure 5.33: Evaporating mass of carbon disulphide with substrate on cold plate

A significantly higher rate of evaporation for carbon disulphide can be observed which is expected owing to carbon disulphide's larger saturation vapour pressure.

Figures 5.34 and 5.35 show the evaporation profiles when introducing 5% w/w concentration of polystyrene to chloroform and carbon disulphide respectively. An increase in evaporation can be observed in both cases and also a linearization of the profile. This increase in evaporation rate due to the inclusion of polymer is far more dramatic for chloroform.

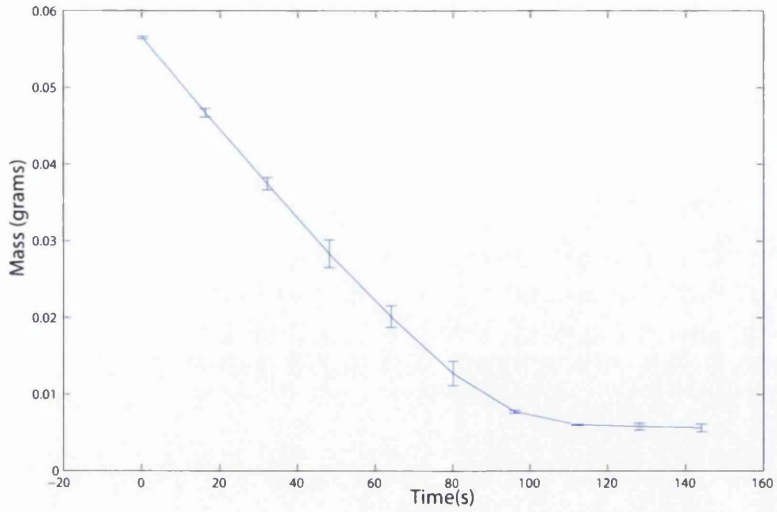

Figure 5.34: Evaporating Mass chloroform with 5% w/w concentration of polystyrene

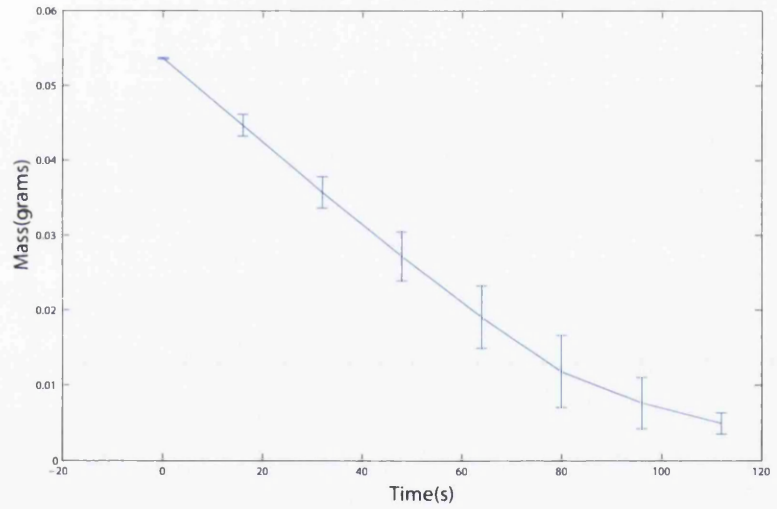

Figure 5.35: Evaporating Mass carbon disulphide with 5% w/w concentration of polystyrene

Chapter 6

Experimental Results

Discussion

Firstly the results concerning radial order assessment shall be considered.

The conformational entropy is generally seen to increase towards the edges of the films for the films cast at 75% and 85% relative humidity, a result which was expected. The edges of the film should in general dry faster leading to lesser times for growth and re-arrangement of condensed vapor. However in the films cast at 80% some unexpected behaviour can be observed. The emergence of two general patterns for the conformational entropy are inherent within the films. In the case of film two and film four the highest conformational entropy and therefore disorder are at the edge of the film, which subsequently decreases towards the centre as expected. However for films one and

three the conformational entropy passes through a minima about two fifths distance from the edge and subsequently increases towards the film centre. It is thought that this behaviour is more likely to be due to some unconscious change in how the casting solution was deposited between the experiments rather than any slight climatic changes. Changes in this deposition could be reflected in many different ways. Unequal masses of deposited solution for instance. It can also be seen that the two films which show this behaviour are the films which have the smallest radii, this difference however is only approximately .3mm. At 85% relative humidity, the film with the smallest radii once again has a drastically different profile of conformational entropy with distance from the centre of the film compared to the other films at this humidity.

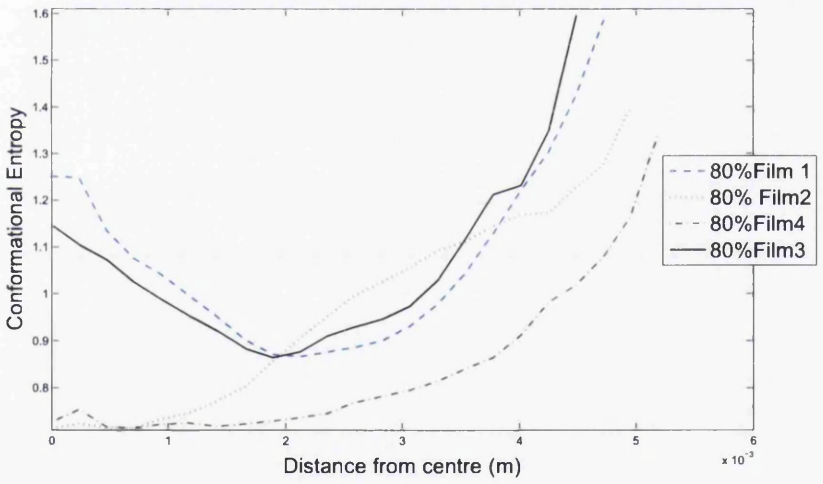

Figure 6.1: Conformational entropy plots at 80% relative Humidity

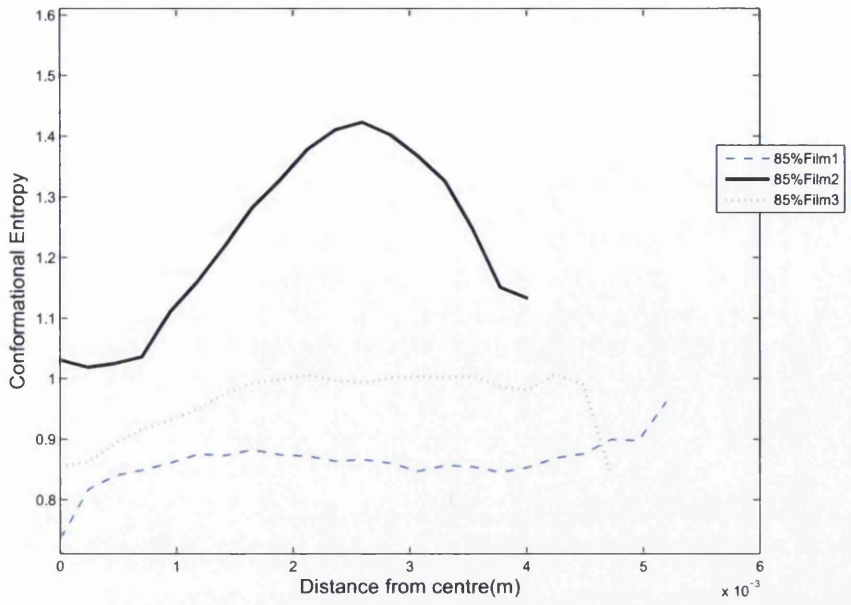

Figure 6.2: Conformational entropy and p_6 plots at 85% relative Humidity

It could be suggested that there is a surface area to volume effect apparent which somehow influences the ordering over the film surface. However at 75% relative humidity, the film with the smallest radii shows the lowest value of conformational entropy and an expected pattern is observed for the profile, in fact at this humidity the smallest film shows the lowest conformational entropy. This is not however enough evidence to rule out surface area to volume effects because although the final film has the smallest size, this does not necessarily reflect the volume of the deposited droplet. It could be that the droplet was just deposited in a more centralized manner. This theory could only be put to test by depositing the casting solution in a more predictable

manner using some kind of mechanistic approach as mentioned in the experimental methods section of this thesis. Improvements on the regularity of the volume of deposited condensate could be improved with the use of a digital micro pipette for instance, however this would still really be insufficient as a steady arm is needed to insure a consistent deposition area. Other possible explanations for the profiles could be based upon differences in polymer concentration throughout the casting solution. At the end of the micro-pipette it was sometimes observed that in the time between drawing the casting solution from its container and just before deposition, the solution could become evaporated at the end of the pipette, leading to an observable concentration gradient at the edge of the pipette. The formation of this concentration gradient is obviously dependant on the time that the solution is exposed to the air between being drawn from the container and being deposited. Although this time was always intended to be as short as possible, differences will have inevitably occurred. This could have resulted in irregularities in polymer concentration within the solution once deposited and therefore irregularities in the final surface. It is well known that preferential evaporation at the edges of a liquid drop can draw solute to the edges if the contact line is pinned, this is now known as the 'Coffee stain effect' after this phenomena was explained by a team at Chicago Materials Research Centre [51] in terms of capillary flow. In fact this phenomena was often noticed after our casting procedure.

It could clearly be seen that large deposits of polymer were being made at the edges of the film, it could be suggested that irregularities of polymer concentration in the casting solution could influence this transport and maybe produce regions in the casting solution where the polymer concentration is insufficient to inhibit coalescence of condensed droplets.

In general it is expected that pore size should increase towards the centre of the films in stagnant conditions. Faster evaporation at the edges of the deposited solution should lead to smaller pores in these areas based on lesser timescales for water to condense fuelled by the evaporative cooling effect. This was not always observed . At 80% relative humidity the general trend was in fact to the contrary (figure 6.3).

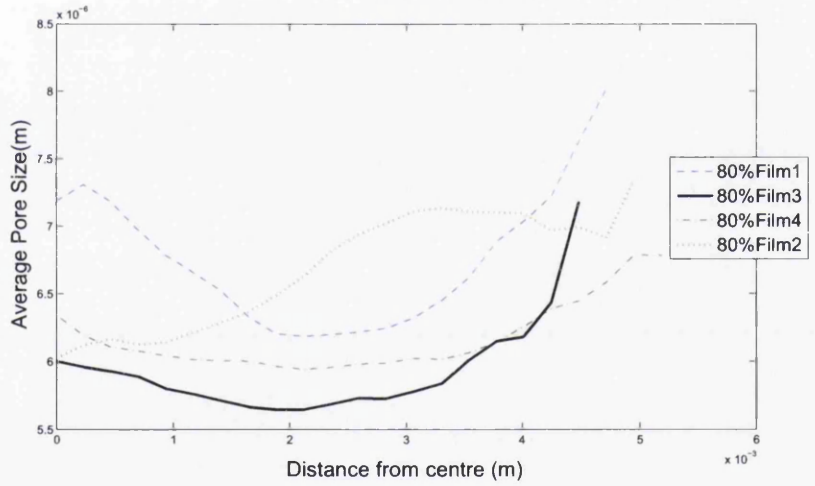

Figure 6.3: Average pore size plots at 80% relative Humidity

As can be seen the pore size in this case always reaches its maxima at

the edges of the film. At 85% the opposite trend is apparent for two of the films with the other showing a relatively flat profile in pore-size from the centre outwards, at 75% we see two films with decrease towards the edges and one film with an increase. The argument that smaller pores are likely to be found at the edges in films created in stagnant conditions though is really only based on the relative times of evaporation for the liquid solvent from the centre inwards, and not really on any thermodynamic considerations. Although the timescale for evaporation may be lesser at the edges, an increase in cooling efficiency resulting from the increased evaporation rates could be sufficient to increase the flux of vapour to the surface enough to deposit more condensate per unit area over the course of the casting experiment despite the timescale for evaporation at the edges being lesser. This said if the solvent at the edges is continually replaced by capillary flow this process could continue as long solvent is available to evaporate and the time scale for evaporation at the edges might not be drastically different. Despite there being rather large profiles in average pore size throughout the majority of the films, sometimes $\pm$ 2 micron. Some films show very even pore size distributions over the radial distance, showing that large areas of uniformity are achievable. The problem now is working out what is the cause in the differences of the observed radial ordering from film to film in our experiments. It is thought that this once again could be due simply to inaccuracies in depositing the casting solution.

Looking back now at the results obtained in the chamber at 85% for the average pore size.

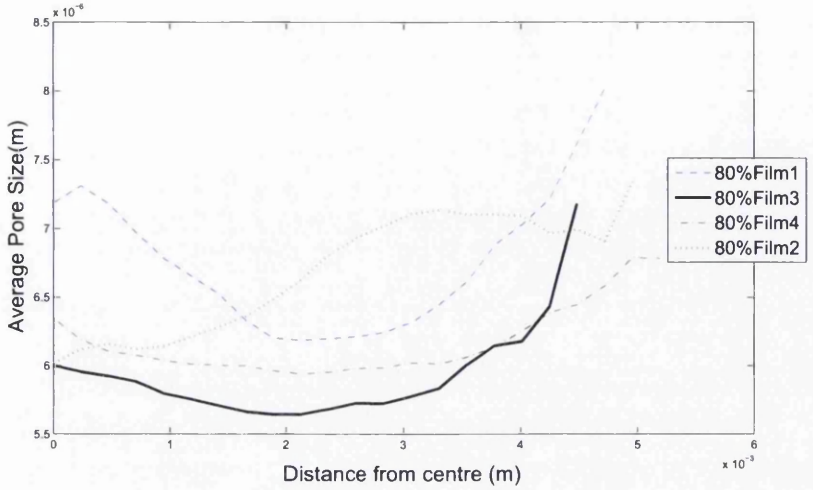

Figure 6.4: Average pore size plots at 80% relative Humidity

Film 2 shows the most uniform distribution in average pore size across the film, whilst also having the lowest average pore size in general. The conformational entropy profile is also the most uniform for this film. The volume to surface area ratio of the casting solution when initially deposited in creating this film could allow the solvent to evaporate quickly enough such that the size of droplets on the surface were limited to this smaller size. In films one and three the casting solution took perhaps longer to evaporate leading to larger pores and also a process that disorders the system. Maybe perfecting these timescales is key in producing reliable long range order. Hopefully increased accuracy in providing the initial conditions for growth experiments

could resolve this issue and prove that the system is not a chaotic dynamical system. That is that the final outcome to the experiment is not hyper sensitive to the initial conditions. That said many researchers claim to be able to control the pore size using flows of humid air and claim repeatable results. As far as we are aware this remains to be proven by a study over large areas such as the this one.

The pore size at the centre of the films increased between 70% and 85% relative humidity, the largest pore sizes at the centre of the films were however observed at 80%. When analysing the chamber data for the experiments at 80% it was noted that the period when these films were prepared was warmer with respect to the times when the other films were prepared, by approximately three degrees. The absolute humidity therefore would have been ≈ 16 grams per cubic metre on the colder day at 85% relative humidity and ≈ 19.4 grams per cubic metre on the warmer day at 80% hence the increased pore size. This trend is also reflected in the total deposited condensate mass for each relative humidity.

The hexagonal order of the films is characterized by the parameter p6 which is the probability of a conformation of 6 at a given location, this parameter reflects the measurements of the conformational entropy in the expected fashion. That is the parameter p6 displays the inverse behavior. Higher regions of conformational entropy have higher spreads in conformation, thus

the probability of a conformation of 6 is decreased and therefore the degree hexagonal ordering.

Next the results concerning evaporation and temperature drops shall be discussed. The rate of evaporation of the $50\mu L$ droplet of carbon disulphide is evidently greater than the case of Chloroform owing to the greater saturation vapour pressure of carbon disulphide. However the differences in latent heats of vaporization also play a role in the observed profiles. The temperature drops experienced for the liquid are much lower in the case of carbon disulphide than that of chloroform, which would have resulted in a higher relative decrease in saturation vapour pressure in the case of carbon disulphide. The temperature drops are in fact observed to be this way in the experiments. The differences in temperature drops when performing the evaporation experiments with the glass substrate directly in contact with the copper plate and when performing the experiment on the ceramic supports are quite apparent. With the ceramics, the minimum temperature drop changes by roughly 8 degrees relative to when the substrate is placed directly on the copper plate. This result clearly demonstrates the extent to which the conduction of heat through the substrate can influence the dynamics of the process. This could even be used as a tool in attempting to control the process in stagnant conditions. By placing the substrate on materials with different thermal properties one could seek to control the interface tempera-

ture, evaporation rate and hopefully deposition. This result also shows the importance of quoting the nature of the surface used on which to place the substrate in publishing results.

When adding a 5% weight for weight concentration of polymer to the pure solvents, the evaporation rate clearly increases for both substances due to the now constant surface area. This increase is much more dramatic in the case of chloroform and in fact with the contact lines now pinned the profiles for both substances are very similar. This larger relative increase could be explained in terms of larger decreases in temperature for Carbon disulphide resulting in a larger relative decreases in saturation vapour pressure.

Chapter 7

Modelling Results

This chapter will describe results obtained using the numerical model

7.1 Evaporation Rates For Pure Solvents

The numerical methods described previously are now used to look at solvent evaporation rates under differing conditions.

Firstly the model is used to look at the mass of pure solvents over time at different ambient temperatures for an initial volume of $50\mu L$. In modelling the evaporation rates a perfect thermal contact boundary condition is used below the substrate in solving for the temperature distribution. A glass slide thickness of 2mm is used which separates the evaporating solvent from the boundary. Elsewhere perfect insulation boundary conditions are used. The areas used in calculating these evaporation rates were calculated with knowl-

edge of the cavity sizes in the cavity slides used in experiments. The solvent was always assumed to have the shape of a spherical cap and the surface area could be calculated at a given time step using the equation of spherical cap from the updated droplet volume. The relative humidity is set to 10% so the influence of water on the process is eliminated. Unless otherwise stated the flow rate used in calculating the mass transfer coefficient and thermal boundary layer thickness is $0.06ms^{-1}$.

Figure 7.1 and 7.2 show the evaporation profiles for carbon disulphide and chloroform respectively.

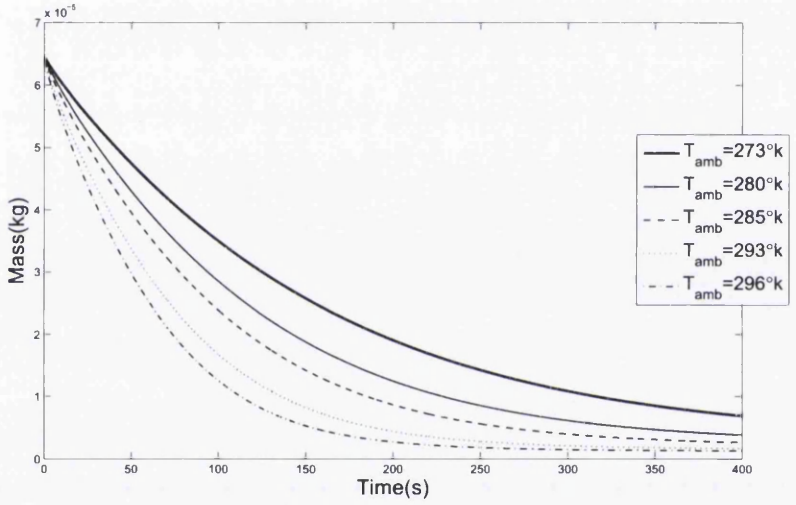

Figure 7.1: Evaporation profiles for temperatures between 273K and 296K for carbon disulphide

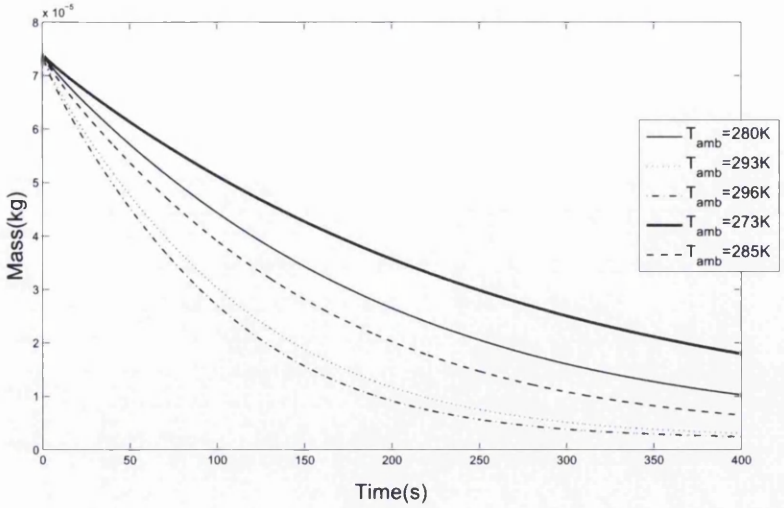

Figure 7.2: Evaporation profiles for temperatures between 273K and 296K for chloroform

Figures 7.3 and 7.4 show the corresponding interface temperature drops.

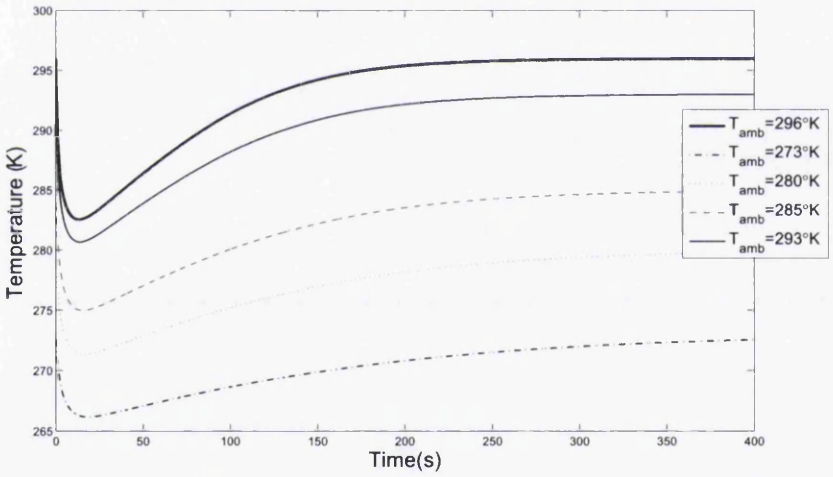

Figure 7.3: Interface temperature drops for ambient temperatures between 273K and 296K for carbon disulphide

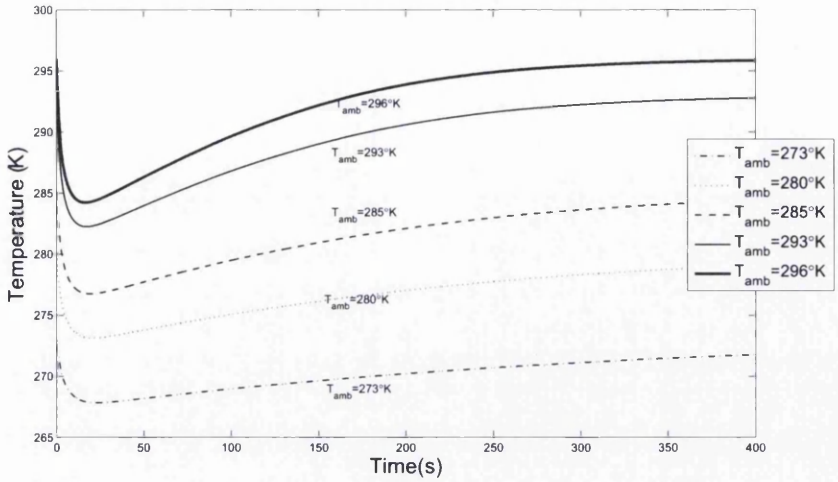

Figure 7.4: Interface temperature drops for ambient temperatures between 273K and 296K for chloroform

As can be seen the interface temperature drops are larger in the case of carbon disulphide owing to the differing thermal properties.

Now for an ambient temperature of 293K looking at the influence of flow on the evaporation rates. A perfect thermal contact boundary condition is used beneath the substrate and at the edge of the thermal boundary layer assuming constant replenishment from the stream. Figure 7.5 and 7.6 show the simulated evaporation rates and temperature drops respectively for flow rates of 0.1, 0.5 and 1 ms^{-1}.

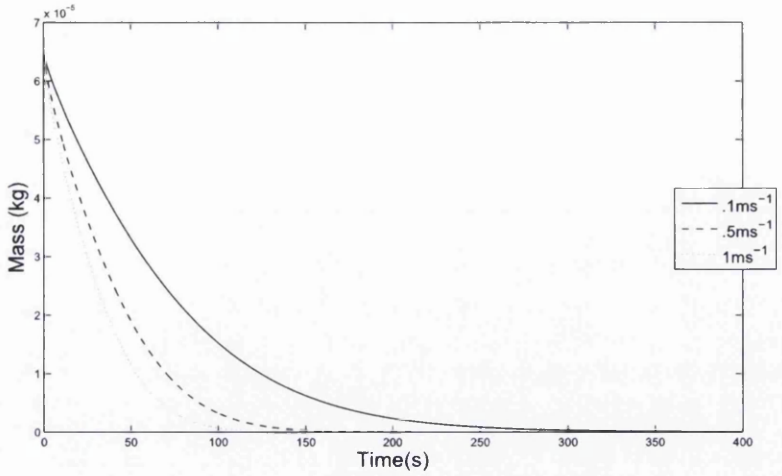

Figure 7.5: Carbon disulphide evaporation rates for laminar flow rates of 0.1, 0.5 and 1ms^{-1}

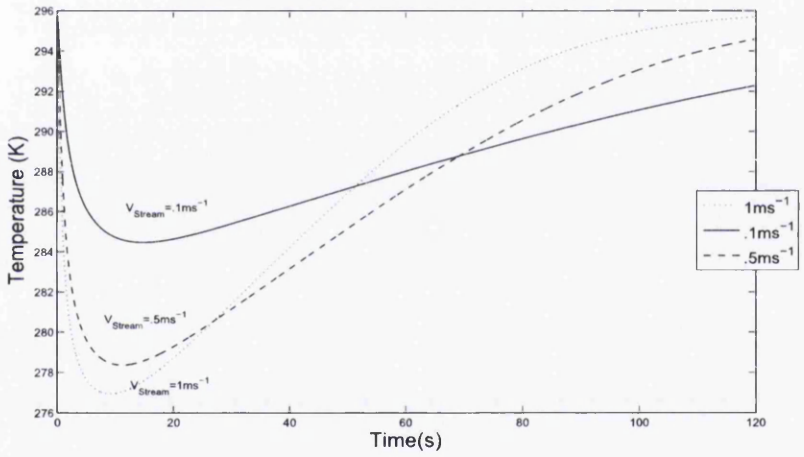

Figure 7.6: Carbon disulphide interface temperature for laminar flow rates of 0.1, 0.5 and 1ms^{-1}

7.2 Growth Experiment Simulations

Now some simulations are considered concerning growth experiments. Firstly a series of experiments where a laminar stream is passed over casting solution on a sample slide of thickness 2mm. The sample is a $50\mu L$ drop of carbon disulphide with a diameter of $\cong 1cm$ (As noted in experiments). The evaporative surface area is considered circular and constant. The position of the thermal boundary layer is evaluated and averaged over the sample length and also the mass transfer coefficient according to the flow rate. A perfect thermal contact boundary condition is employed at the edge of the thermal boundary layer and heat transfer is then considered beneath this position. The mole fraction of water vapour is calculated via the relative humidity and also ascribed as constant based on continual replenishment from the stream. Firstly the situation is considered where a heat source exists beneath the sample slide. This maintains the temperature beneath the slide at ambient temperature which is 293 K. A variety of flow rates are considered and the evaporation rates, interfacial temperatures and water deposition rates are evaluated.

Figure 7.7 shows the simulated evaporation rates.

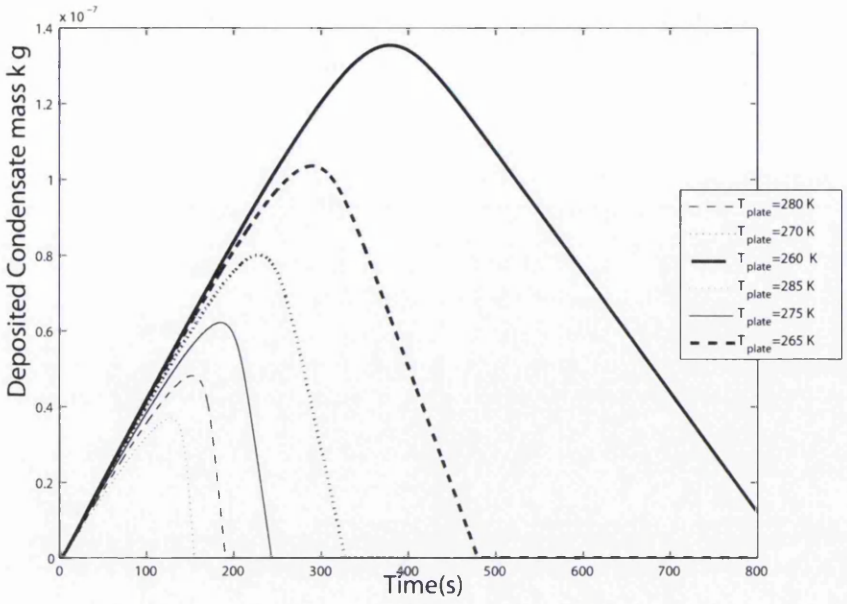

Figure 7.7: Evaporation rates for a 50μL solution drop with 5% polystyrene evaporating under differing laminar flow rates in an 80% relative humidity airflow

Intuitively the rate of evaporation increases with increasing flow rate and with the area of the droplet now held constant the profiles are approximately linear.

The temperature everywhere within the domain is now solved over the duration of the growth experiment.

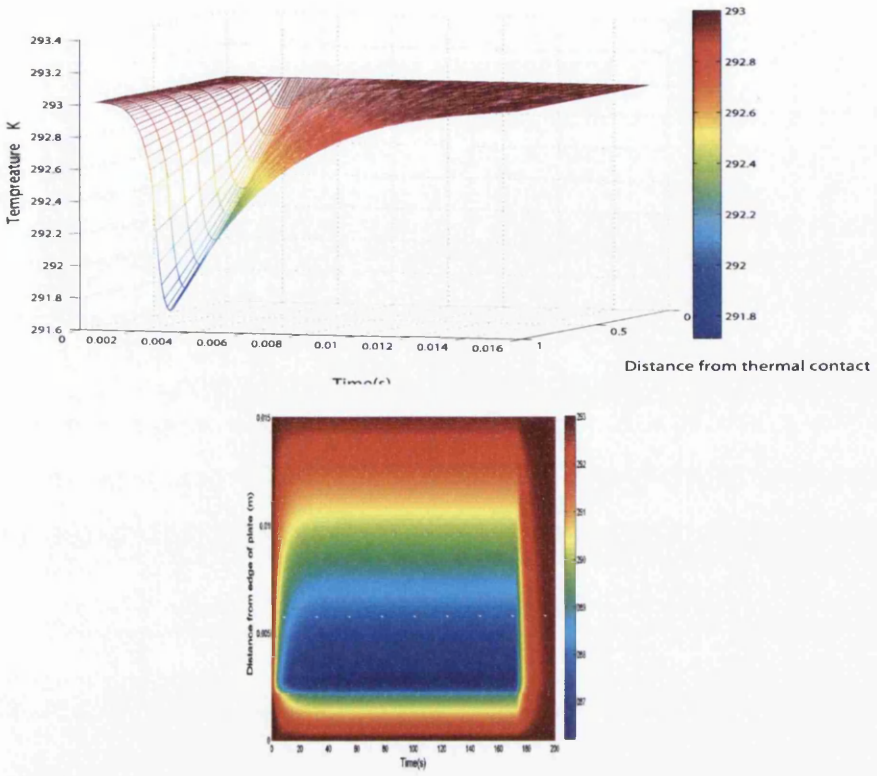

Figure 7.8: Plots depicting solutions for the temperature distributions

Figure 7.9 shows the interface temperature drops for the different flow rates considered.

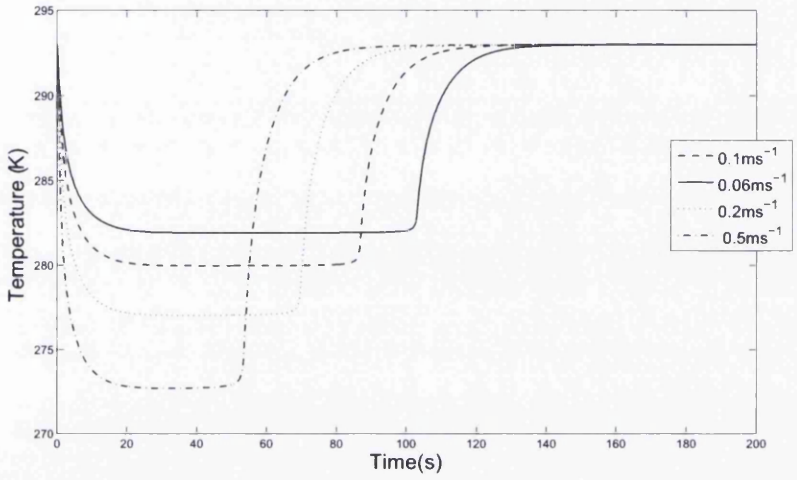

Figure 7.9: Temperature drops for a 50μL solution drop with 5% polystyrene evaporating under differing laminar flow rates in an 80% relative humidity airflow

From these thermodynamic changes the deposited condensate masses can be calculated over the course of the growth experiment (Figure 7.10)

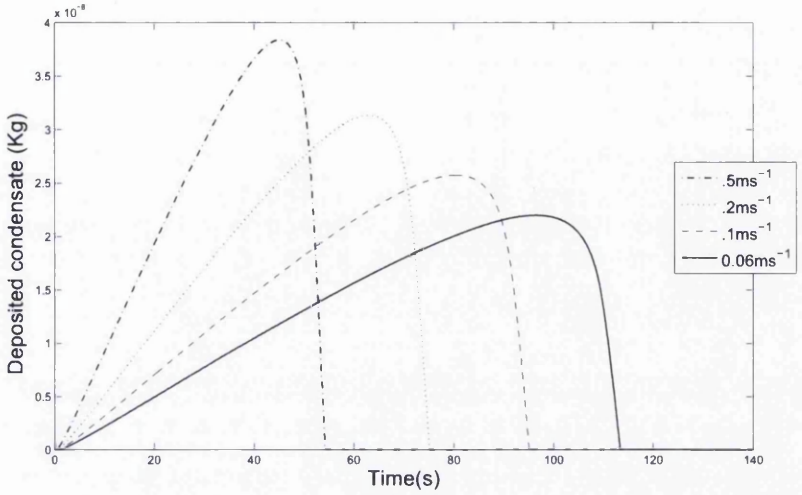

Figure 7.10: Condensate mass for a 50μL solution drop with 5% polystyrene evaporating under differing laminar flow rates in an 80% relative humidity airflow

Clearly increased evaporation rate with increased flow is leading to a larger amount of deposited condensate, despite the timescales for the completion of the process becoming lesser.

Now we consider the same situation using $50\mu L$ of casting solution with Chloroform as the solvent. Figure 7.11 shows the evaporation profiles at different flow rates.

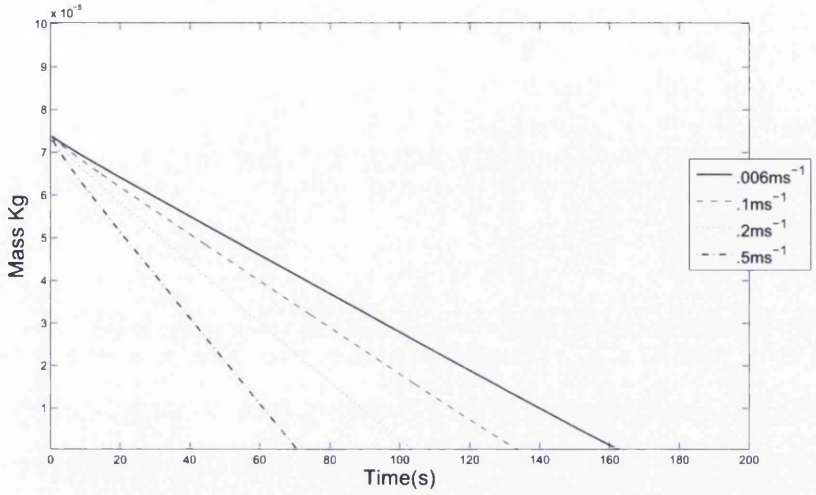

Figure 7.11: Evaporation rates for a 50μL solution drop of Chloroform with 5% polystyrene evaporating under differing laminar flow rates in an 80% relative humidity airflow

The timescales for evaporation are clearly larger than the corresponding flow rate when using carbon disulphide as a solvent.

Figure 7.12 shows the corresponding interface temperature drops.

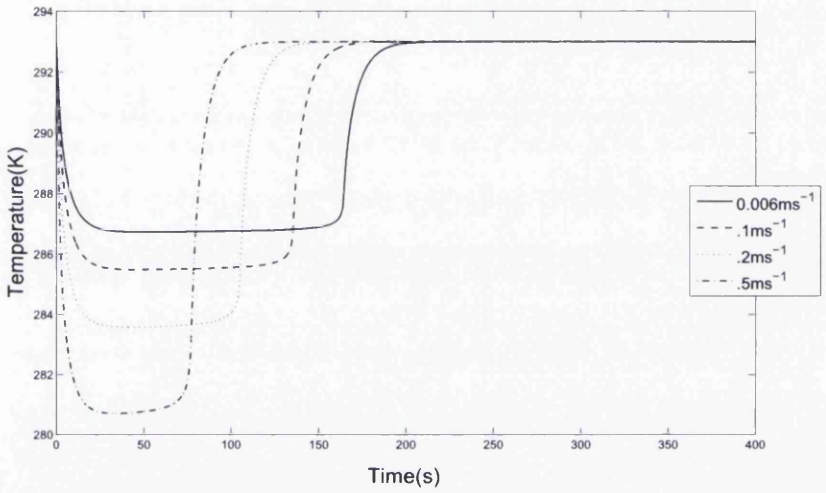

Figure 7.12: Temperature drops for a 50μL solution drop of chloroform with 5% polystyrene evaporating under differing laminar flow rates in an 80% relative humidity airflow

and figure 7.13 shows the deposited condensate masses.

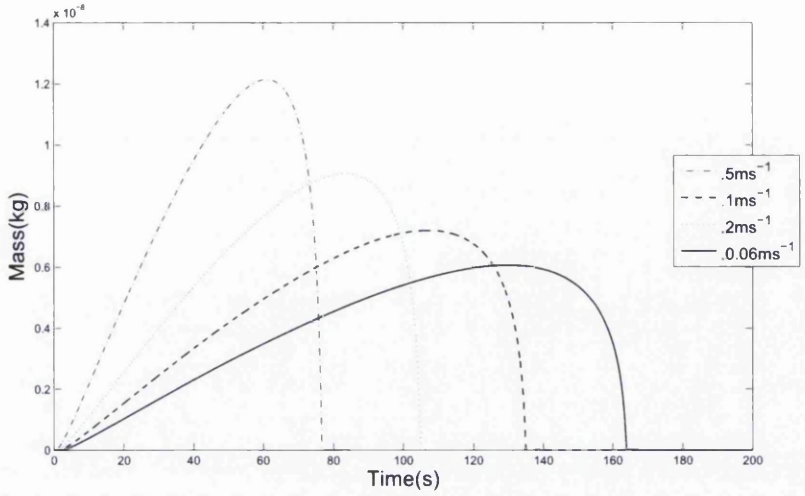

Figure 7.13: Condensate mass for a 50μL solution drop of chloroform with 5% polystyrene evaporating under differing laminar flow rates in an 80% relative humidity airflow

The quantities of deposited condensate are lower than the corresponding case when using carbon disulphide. Despite the larger timescales for evaporation the increased cooling in the case of carbon disulphide leads to larger deposited masses of condensate.

Now the same situation is examined except that the bottom of the glass sample slide is considered to be totally thermally insulated i.e. no heat flux from the bottom boundary. Figure 7.14 shows the evaporation profile for a $50\mu L$ drop of carbon disulphide with the insulated bottom boundary.

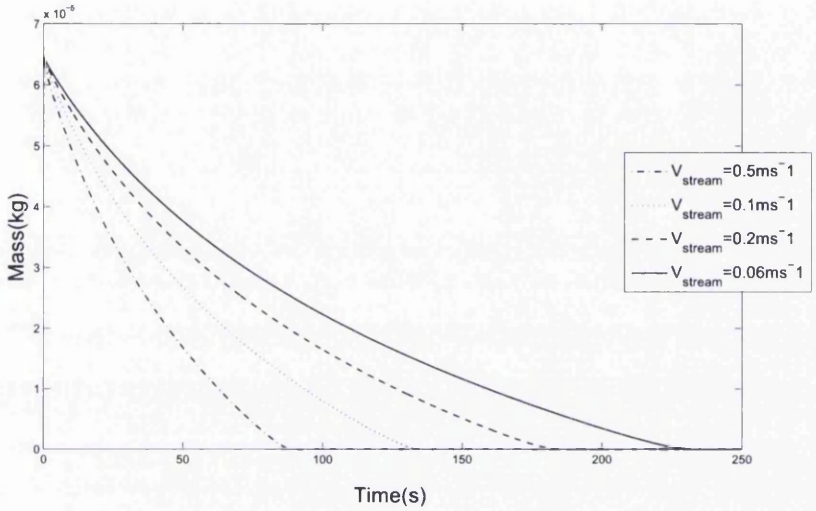

Figure 7.14: Evaporation rates for a 50μL solution drop with 5% polystyrene evaporating under differing laminar flow rates in an 80% relative humidity airflow with perfect insulation beneath the sample slide

With an insulated bottom boundary the evaporation rates are decreased, and lowered saturation vapour pressure and diffusivity lead to a non linearization of the profile. Figures 7.15 and 7.16 show the corresponding temperature drops and the deposited condensate masses respectively.

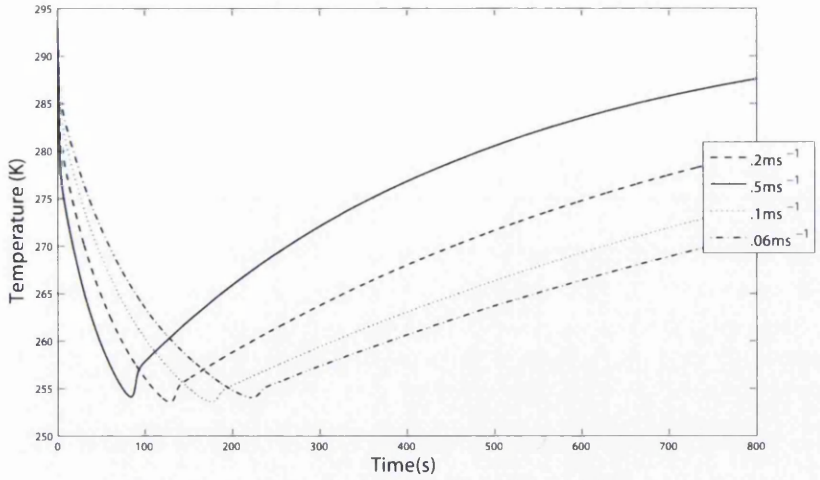

Figure 7.15: Temperature drops for a 50μL solution drop with 5% polystyrene evaporating under differing laminar flow rates in an 80% relative humidity airflow with perfect insulation beneath the sample slide

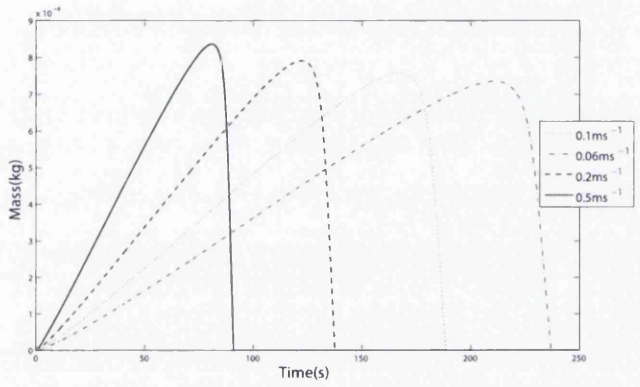

Figure 7.16: Condensate mass for a 50μL solution drop with 5% polystyrene evaporating under differing laminar flow rates in an 80% relative humidity airflow with perfect insulation beneath the sample slide

7.2.1 Effect Of Slide Thickness

Now we look at the influence of substrate thickness on the dynamics, with a perfect thermal contact boundary condition on the bottom boundary. Figure 7.17 shows the simulated evaporation profiles when using different substrate thicknesses for a 50μL drop of Carbon disulphide and a flow rate of $0.2ms^{-1}$.

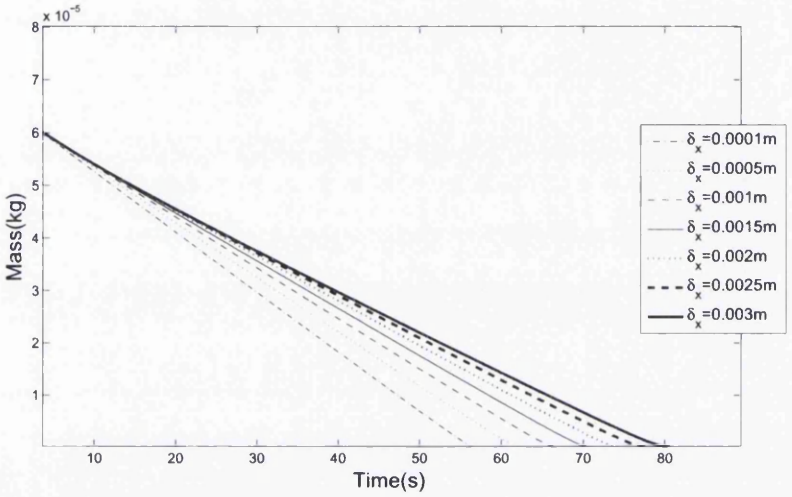

Figure 7.17: Evaporation profiles for different substrate thicknesses for an ambient temperature 293K and a flow rate of $0.2ms^{-1}$

and the corresponding interface temperature drops and condensate masses are depicted in figures 7.18 and 7.19 respectively.

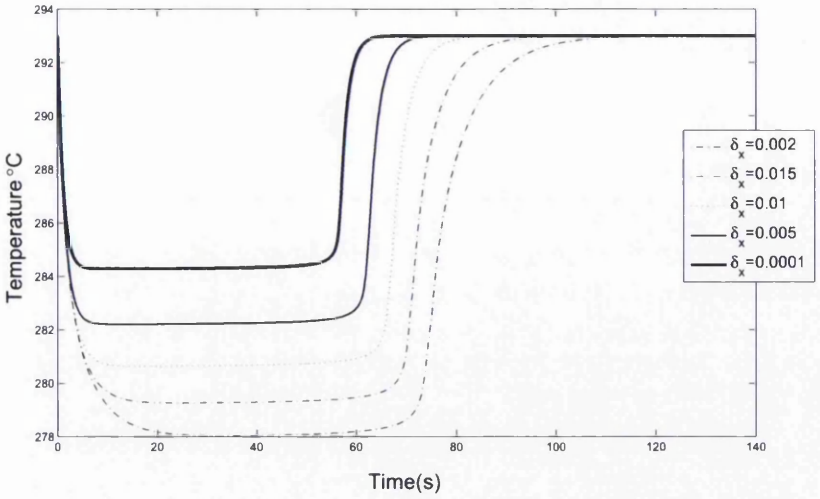

Figure 7.18: Temperature drops for different substrate thicknesses for an ambient temperature 293K and a flow rate of $0.2ms^{-1}$

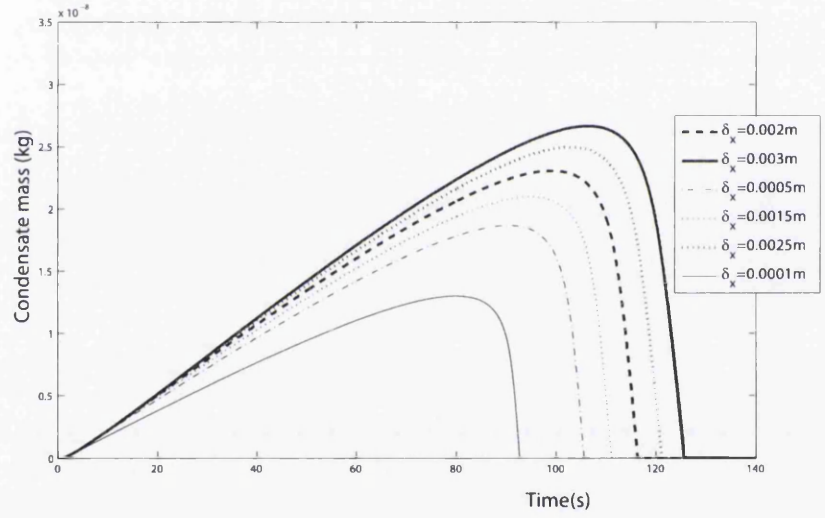

Figure 7.19: Condensate masses for different substrate thicknesses, for an ambient temperature 293K and a flow rate of $0.2ms^{-1}$

7.2.2 Effect Of Humidity

Now we look at how changing the humidity of the airflow effects the condensate mass profiles. Figure 7.20 shows the simulated condensate mass profiles for a range of relative humidities using a flow rate of $0.006ms^{-1}$ at an ambient temperature of $25°C$ using carbon disulphide.

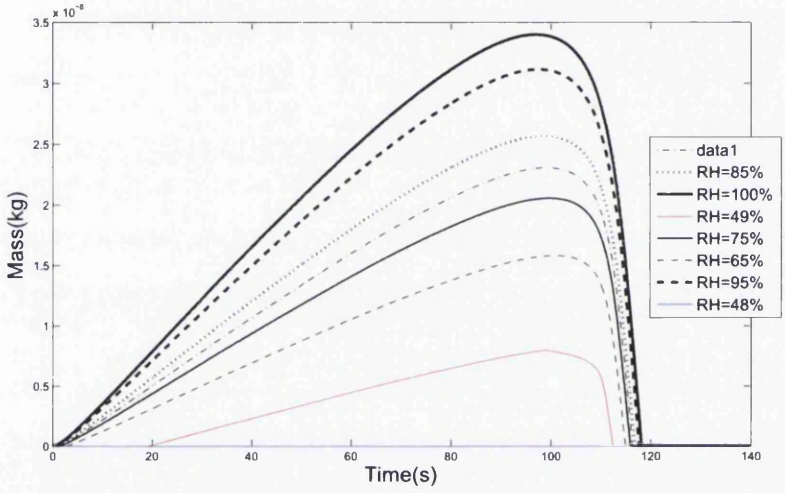

Figure 7.20: Condensate masses for different relative humidities when using carbon disulphide

Clearly decreasing relative humidity leads to decreasing amounts of deposited condensate and below 49% no condensate is formed.

Figure 7.21 shows the corresponding profiles when using chloroform.

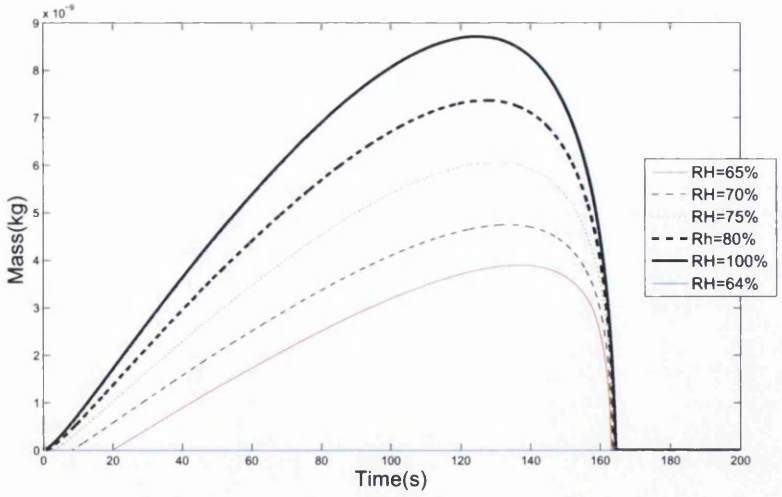

Figure 7.21: Condensate masses for different relative humidities when using chloroform

The same behaviour is evident when using chloroform. Although in this case the relative humidity must be above 65% in order to form condensate.

7.2.3 Using Cooling To Aid Condensation

Here we look at the different condensate mass profiles when using bottom boundaries maintained at differing temperatures below ambient. Once again the ambient temperature is 293 K. The flow rate used in these calculations was always $0.006ms^{-1}$

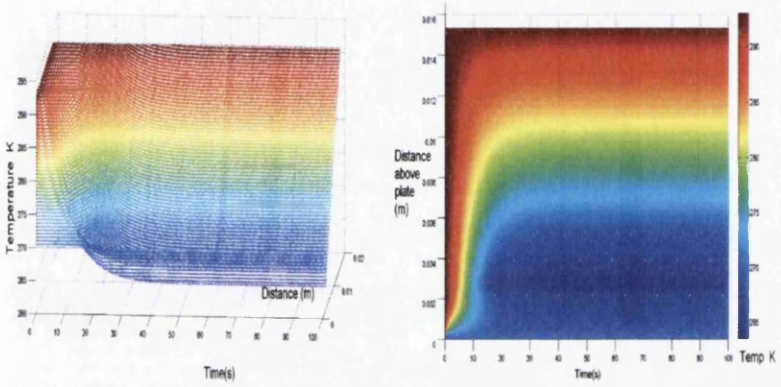

Figure 7.22: Plots depicting solutions for the temperature distributions with cooled bottom boundaries

Figure 7.23 shows the condensate mass profiles for different temperature bottom boundaries when using carbon disulphide as a solvent.

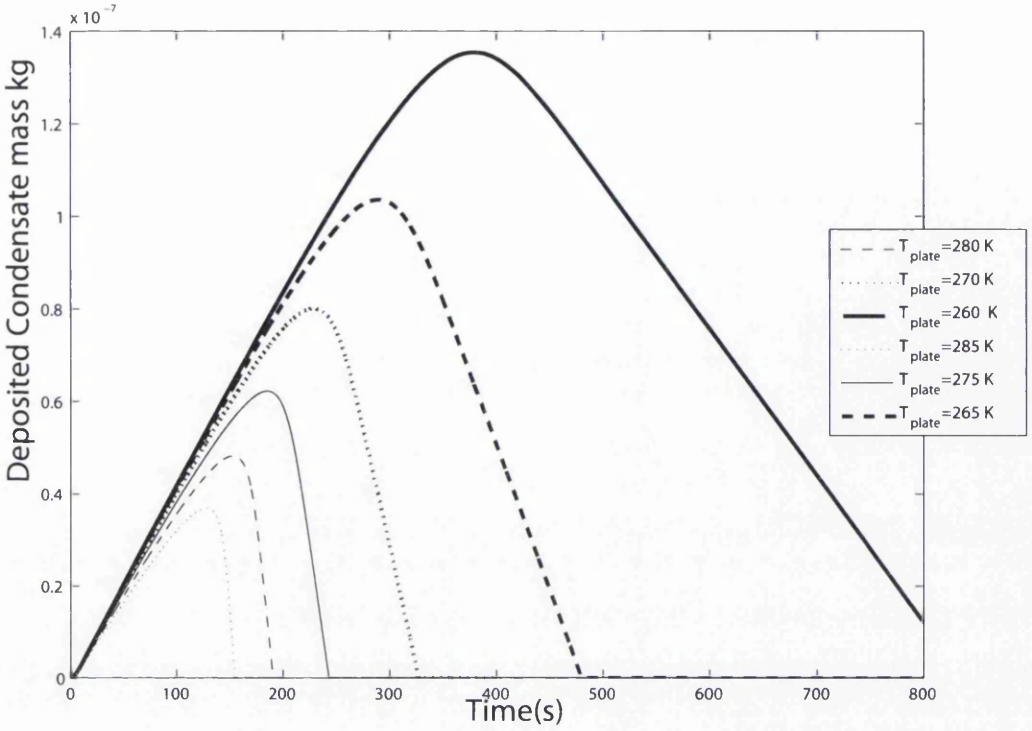

Figure 7.23: Deposited condensate masses at different plate temperatures

As expected the process can be severely altered by cooling of the sample solution, leading to higher quantities of deposited condensate.

Chapter 8

Numerical Modelling

Discussion

When the model was used to look at evaporation of solutions containing polymer a constant surface area was prescribed. This immediately led to increased rates of evaporation compared to the pure solvent case and a linear evaporation profile was observed. This also however had a dramatic effect on the thermodynamics. When a perfect thermal contact boundary condition was used beneath the glass slide, this induced an almost constant surface temperature at the interface for some time during the simulated casting procedure. The rate of removal of energy by evaporation and the rate of arrival of energy through conduction from the boundaries through the glass slide and the air above therefore arrived at a balance producing an equilibrium situation.

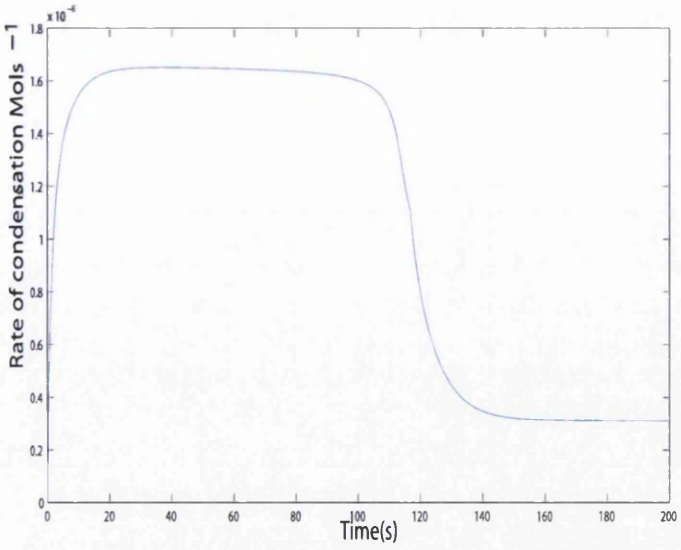

Figure 8.1: Rate of condensation with perfect thermal contact boundary condition

The rate of deposition of condensate followed a similar pattern and a region of constant flux can be observed (figure 8.1). This flux was removed from the mass balance when the evaporation of solvent had ceased since at this point the polymers mass fraction in the mixture has reached unity and the mixture should now display solid like properties. It is assumed therefore that any deposited condensate formed after this point should not influence the pore sizes and therefore should not be included.

The temperature profiles when considering a totally insulated bottom boundary were very different. The temperature steadily decreased through the duration of the evaporation process. With heat only available from the air

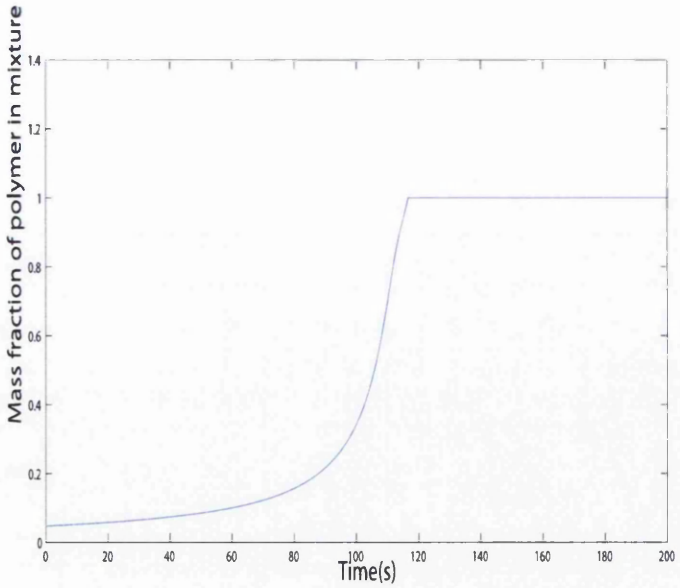

Figure 8.2: Mass fraction of polymer

above the evaporating solution, the temperature drops were correspondingly higher and the evaporation rates therefore lower and non-linear due to lowering saturation vapour pressures and diffusivity's. These larger timescales for evaporation and the higher drops in temperature inevitably led to higher amounts of deposited condensate.

The rate of condensation (figure 8.3) can be seen to asymptotically increase throughout the growth experiment. The asymptotic nature of the profile is due to decreases in diffusivity slowing down diffusive transport of vapour to the casting solution surface. This decrease in diffusivity therefore seems to set a limit on how high the rates of condensation can become with decreasing temperature.

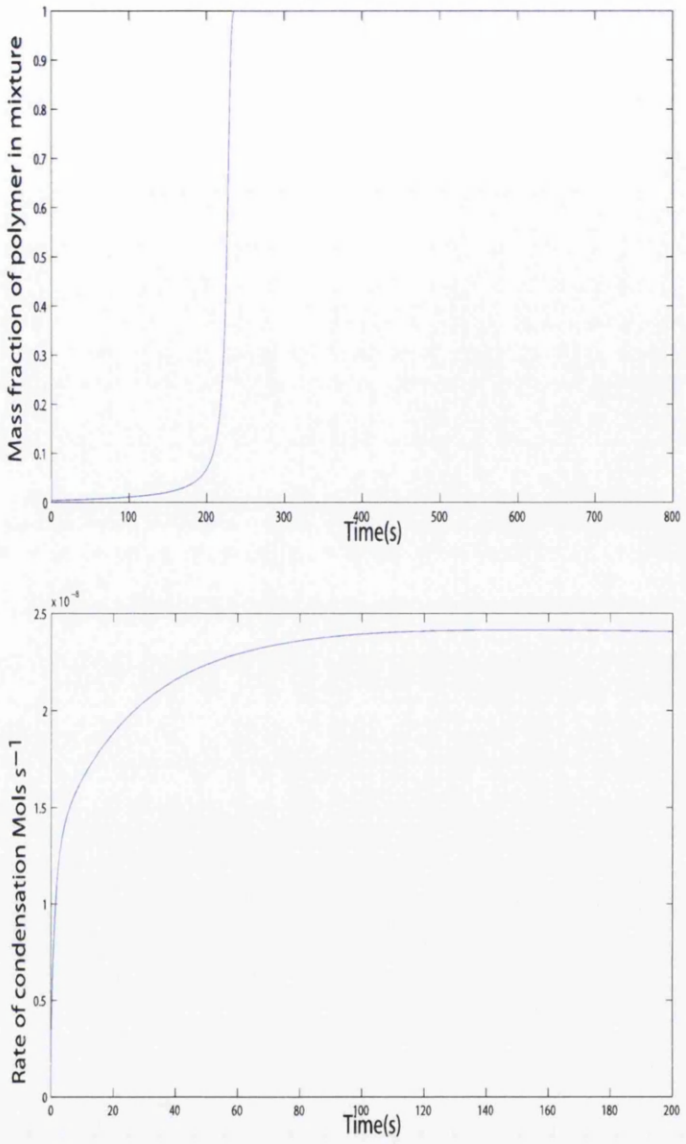

Figure 8.3: (i) Mass fraction of polymer (ii) Rate of condensation with perfect insulation at the bottom boundary

When looking at cooling assisted condensation the interface temperature profiles once again experienced regions where a steady state situation was set

up (figure 8.4).

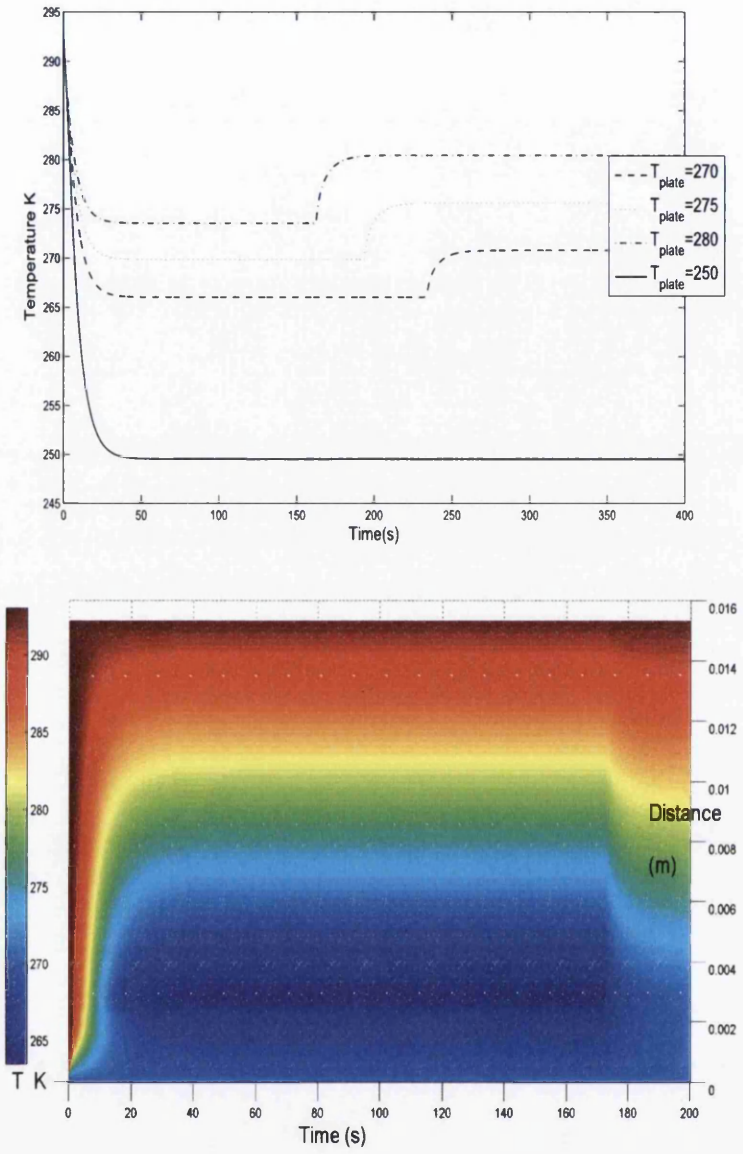

Figure 8.4: Temperature profiles using plate

When cooling to temperatures as low at -20°C the evaporation rate became so slow as not directly influence the thermodynamics significantly and

the interface simply became approximately the temperature of the plate. So it seems within the context of this numerical model, as long as the bottom of the substrate is maintained at constant temperature a steady state situation can be realised for some time after deposition of the casting solution resulting in a period where a constant rate of condensation is apparent. It seems that the interplay between diffusivity, saturation vapour pressure, the rate of evaporation/condensation, the latent heats and the thermal properties are related to the thermodynamics in such a way as to allow the interface temperature to always reach a steady state at some point in the process in this case. The duration and temperature of this steady state part of the process depends on the plate temperature, airflow rate and resulting rates of evaporation.

If the nature of the substrate were to change the dynamics of the process can be altered significantly. For example if we were to use a Fiber-glass type material as a substrate, with thermal properties, k=0.05 $Wm^{-1}K^{-1}$, $\rho = 5670kgm^{-3}$ and c=$1000jkg^{-1}K$. Figure 8.5 shows the interface temperature profiles when holding the plate at ambient temperature (293K) and using a flow rate of $0.06ms^{-1}$.

There is no period of constant temperature at the interface in this case just cooling followed by re-equilibrium. The rate of condensation follows the expected profile asymptotically increasing with time as when using a totally insulated boundary. It seems as though a standard glass slide provides access

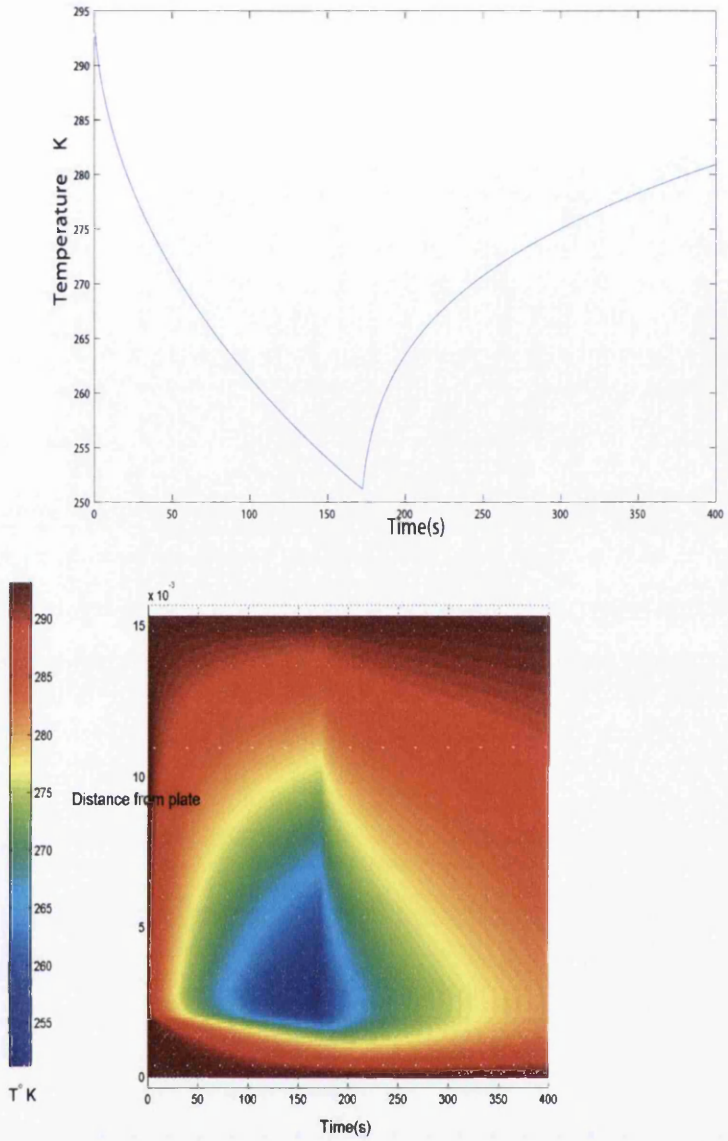

Figure 8.5: Temperature profiles using plate

to an equilibrium regime whilst allowing the liquid to cool enough to saturate water vapour in the prescribed flow.

When looking at the effect of relative humidity on the deposited conden-

sate, we observed that below 49% no vapour was deposited as liquid water at a flow rate of $0.06ms^{-1}$ and an ambient temperature of 20°C when using carbon disulphide as a solvent . It has been observed in the literature [52] that the casting chamber had to have a relative humidity above 50% to produce structured films. This demonstrates that the calculations made for the interface temperature drops are indeed realistic since it is this that determines the limit in actual vapour density needed to saturate at the interface and liquify. Although within the context of our results increasing the flow rate should see this percentage decrease as increased flow rates induces higher evaporation rates and therefore increased rates of cooling. It must also be noted that these calculations were carried out assuming efficient heat transport to the bottom of the sample slide enabling the temperature to remain at ambient, deviation away from this condition should see this percentage fall. In the case of chloroform a relative humidity 64% was needed to create condensate under the same conditions. However the numerical scheme predicts that at 28°C a relative humidity of greater than 56% is needed to produce condensate when using Chloroform. It has been noted that a relative humidity of 55% was needed in stagnant conditions to form macro-porous polymers structures in a stagnant humid environment, when using chloroform as the solvent a [27]. Once again suggesting that our simulations of the thermodynamics give realistic estimates for the interface temperature.

How important the rate of condensation could be on ordering and growth, of droplets on the surface is not yet clear and requires more work relating both concepts into one complete theory. Of course this numerical model assumed the rate of evaporation was the same over the whole of the casting solution based upon an averaged mass transfer coefficient. If a local mass transfer coefficients were prescribed to calculate rates of evaporation across the film at different surface positions one might find that a steady state temperature distribution is not apparent across the whole film, due to the differing rates of evaporation. These questions will inevitably be the path to future work on this subject.

The maximum condensate mass in the simulations is seen to always increase with increased prescribed flow due to faster evaporation and therefore cooling. In the literature it is frequently noted that smaller pore sizes are achieved with higher flow rates. This seems to suggest that within the context of our physical model at present growth and nucleation must be highly dependant on the timescale for which the evaporation process occurs, such that even though the amount of deposited vapor is higher at increased flow rates smaller pores still arise. It could be however that neglecting coupling effects between the condensing vapour and evaporating solvent have therefore overestimated the dependence of flow on deposited condensate. It is also quite likely that the derived mass transfer coefficient is overestimating the ef-

fect of increased flow on the evaporation rate, this is because a singular value of the flow rate was used neglecting any reduction as the flow passes over the surface, this overestimation will have inevitably lead to an exaggerated dependence of the temperature drops on the flow rate and therefore also the condensation rate. Further experimentation will be required to assess how accurate the simulated dependence of flow on evaporation rates is.

Chapter 9

Conclusion

Within the context of breath figure substrates cast under stagnant conditions, sometimes large physical areas can be produced across the film surface having relatively small changes in pore size. These situations were observed in our experiments however, we also observed films cast having profiles of pore size from the centre of the cast films outwards increasing or decreasing sometimes by up to two micron. The possibility of creating large regions with relatively uniform pore sizes is clearly possible using our experimental setup however, doing this repeatedly and understanding why this only happens sometimes remains a challenge. This knowledge will only come with increased accuracy in recreating the casting conditions which influence the growth in our experimental setup. The image analysis program is now proving an essential device for quantifying improvements to the experimental setup and assessing the degree of long range order in produced materials. The experimental sys-

tem itself would benefit by the investment in a high accuracy environmental chamber and also a mechanical deposition system. Within the context of this work it is believed that to continually produce films with long range order of the quality necessary to realise applications requiring this order, such as photonic band gap materials an automated high precision experimental setup is required that eliminates any human intervention in the casting procedure. In order for this kind of setup to be realised the casting solution should be continually mixed up to the point of deposition to ensure that initially no concentration gradients are present in the casting solution. Dispersion of the polymer to the edges of the films due to the capillary flows induced by preferential evaporation at the edges of the casting solution may be avoided by enclosing the casting solution within a cylindrical container. Removing these edge effects should also remove the capillary action set up across the film surface leading to a more uniform distribution of polymer through the duration of the process.

In order to see whether the predictions made by the model for deposited condensate are realistic, the image analysis routine was used to gain an approximation of the deposited condensate mass in the films cast at 75%, 80% and 85% relative humidity. The results were averaged for each set of casting conditions and the results are shown in figure 9.1.

These experiments were carried out without any applied flow, the best

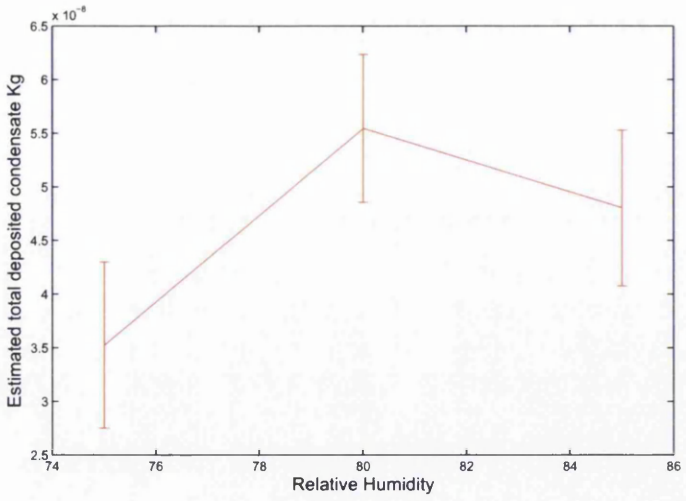

Figure 9.1: An estimate of total deposited condensate at each relative humidity

comparison we have at present is to compare the results to our lowest flow rate results, lowering the flow rate any further in the simulations would mean invalidating some of the assumptions made in deriving the mass transfer coefficients. The corresponding results from the numerical model are given in figure 9.2.

Clearly the numerical model seems to make at least correct order of magnitude predictions, the masses calculated in the experiments are larger and show larger relative increases between the differing relative humidities. It doesn't come as a surprise that the simulations underestimate the amount of condensate. The driving force used in the Maxwell Stefan equation neglected certain effects (see future work) which could increase the condensate mass

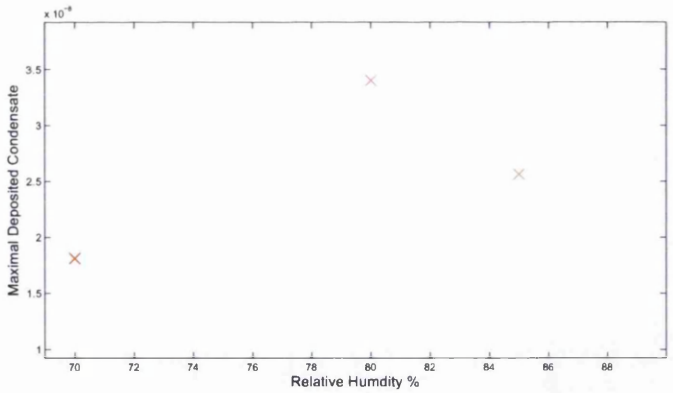

Figure 9.2: Numerical model maximal total deposited condensate at $0.06ms^{-1}$

prediction significantly.

The numerical modelling work therefore has shown that the essential bulk dynamics of the process can be described leading to realistic estimates of deposited condensate masses. Although the influence of flow on this mass needs further study, it has been shown that the temperature drops experienced due to the evaporative cooling effect can be simulated with very reasonable comparison to experimental results. Also it has been shown that the extent of heat conduction from beneath the substrate within this representation of the physical system can lead to large changes in deposited condensate mass, emphasizing the need for quotation of the material on which the substrate lies in publications. It has been demonstrated that periods can exist in the casting method where the solution interface has a constant temperature and a rate of constant rate of condensation can be achieved, if the bottom of the

substrate when made from glass is maintained at a constant temperature. This steady state period is due to the occurrence of a balance of energies at the interface. It was also demonstrated that if the substrate had a lower thermal conductivity, that these regions of steady state behaviour are not apparent and the interface continues to cool throughout evaporation of the casting solution leading to asymptotically increasing rates of condensation. The thickness of the substrate used can also affect interface temperature drops quite drastically, in the case of perfect thermal contact and constant temperature at the bottom of the substrate. This could lead to significantly different results for ordering and pore sizes for breath figure structures cast on cover glasses as oposed to sample slides for instance. This observation suggests yet another way that the process may be manipulated. The substrate thickness could be altered whilst keeping all other parameters constant to yield different timescales for the process and therefore different pore sizes in the structures.

When looking at the influence of relative humidity on deposited condensate it was observed that the humidity when looking at low rates of flow had to be above 49% at 20°C in order for condensate to form when using carbon disulphide as a solvent and 54% for chloroform at an ambient temperature of $25°C$ these results are in good agreement with experimental results in the literature demonstrating that the estimates of the interface temperature profiles are realistic.

The modelling presented herein will now allow application to studying growth and re-arrangement of condensate on the surface of the casting solution and it is intended that this will eventually lead to a quantitative relation between pore size/ordering and casting conditions and further understanding of how to successfully exploit the process to its full potential.

Chapter 10

Future work

10.1 Numerical Modelling

The numerical model presented at present, contains a number of assumptions, many of which were made in order to utilise the computational resources available. The path of the experimental work undertaken was chosen because it was thought that stagnant conditions might simplify numerical modelling techniques. To the contrary it was discovered that it actually makes things more complex, at least in terms of the computational resources required. This is because under stagnant conditions, boundary layer theories have no meaning, concentration gradients exist everywhere in the system and due to the length scales over which these extend dispersion of evaporated solvent is now governed by three dimensional equations. An obvious path for future work would be to consider a three dimensional diffusion equation and to use

a finite element method rather than a finite difference approach. This is of course if the resources could be granted.

The same can be said for the thermodynamical treatment, although lesser assumptions were made here a three dimensional treatment would obviously offer significant improvement in describing the heat transfer mechanisms. This could then lead to assessment of possible thermodynamic effects occurring within the evaporating solution and also across its surface.

In describing the production of breath figures when using flows of moist air, a finite element treatment and the subsequent solution of the Navier Stokes equations would not only aid the development of a new experimental setup for the incorporation of flow, but also then give a more accurate depiction of the influence of flow on the dynamics. This treatment in fact is already being considered and meshes are being constructed to allow a two dimensional solution for the velocity profiles over the sample.

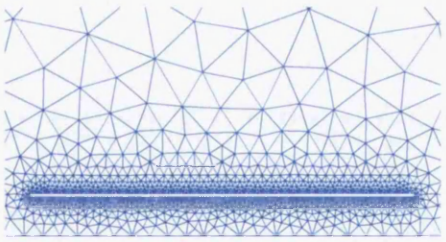

Figure 10.1: Mesh structure for a flat plate

Although already the Maxwell Stefan equations do allow prediction of the mass of condensed liquid water once again some of the simplifying assumptions should be overcome. At the moment larger flow rates always lead to higher rates of condensation due to the increased rate of cooling, caused by these higher evaporation rates. We are not including frictional effects between evaporating solvent and condensing water, which should lead to a degradation in condensate mass. At present the thickness δ in the equation used to calculate the flux of water vapor to the surface is the only direct parameter effecting this flux temperature aside. This thickness decreases with increased flow rates therefore enhancing mass transfer to the surface. At the moment therefore advective transport for the condensing vapour beneath this thickness is therefore neglected. Some theoretical analysis is therefore needed to determine a mass transfer coefficient for the condensing vapour as an alternative to using the thickness δ. In deriving the evaporative mass transfer coefficient a constant velocity was also assumed everywhere above the casting solution interface. Any degradation near the surface is neglected, this will have inevitably lead to an over-estimate for the influence of flow on evaporation and thus indirectly on the condensation rates through the over estimation of increased interface temperature drops.

Further improvement could include the effects of thermal diffusion (Soret effect). This involves updating the form of the driving force in the Maxwell-

Stefan equations, from the version which uses the mol fractions as the driving force to a generalized manner that accounts for the above effects [53].

$$d_i = -\sum_{j\neq i}^{n=1} \frac{x_i x_j (u_i - u_j)}{D_{ij}} - \sum_{j\neq i}^{n=1} x_i x j \alpha_{ij} \frac{\nabla T}{T} \tag{10.1}$$

where α_{ij} is the multicomponent thermal diffusion factor given by

$$\alpha_{ij} = \frac{1}{D_{ij}} \left(\frac{D_i^T}{\rho_i} - \frac{D_j^T}{\rho_j} \right) \tag{10.2}$$

and D_i^T is the thermal diffusion coefficient of component i.

With a more in depth treatment, the current method for describing the saturation condition could also be changed. At present a phase change is initiated only when a saturation condition is created at the liquid-vapour interface based on the bulk vapour-density. Finite temperature differences can drive vapour to the interface, therefore increasing the vapour density in this region. A saturation condition can therefore be created at the interface sooner than prescribed by considering when the bulk vapour density reaches the saturation vapor density, according to the interfacial temperature. Although it seems that the cooling is rapid enough such that creating the saturation condition as the bulk vapour concentration becomes saturated is a reasonable assumption.

It has been demonstrated that the essential dynamics of the process can all be included in a numerical model, and that reasonable estimates can be made

for the amount of liquid deposited dependant on the casting conditions. However using the Maxwell-Stefan equations in this way will only really provide us with deposited liquid masses, and not droplet diameters so this is therefore really at present a model describing film-wise condensation, this is merely because at present the film surface is considered to be totally wettable. In order to build on the work carried out theories of nucleation, surface energetics, buoyancy and surface diffusion should be incorporated within the context of the thermodynamic treatment. It should be considered that critical nuclei could be created above the evaporating surface also , and calculation of the rate the diffusion of these nuclei to the surface could be key.

Some of the early simulation work carried out by Beysons and Knobler considered the production of small droplets on a 2-dimensional surface which were meant to represent the production of critical nuclei. These droplets were created at a constant rate on the surface and then allowed to diffuse. Since the use of the Maxwell-Stefan equations starts to give quantitative estimates for the deposited liquid water masses in a given area we can now start to consider quantified time dependant surface fluxes and look at the corresponding droplet growth rates. In fact programs have all ready been created to describe surface deposition and coalescence (Random Sequential Adsorption), however these results at the moment do not bare any physical significance and so were left out in the results section.

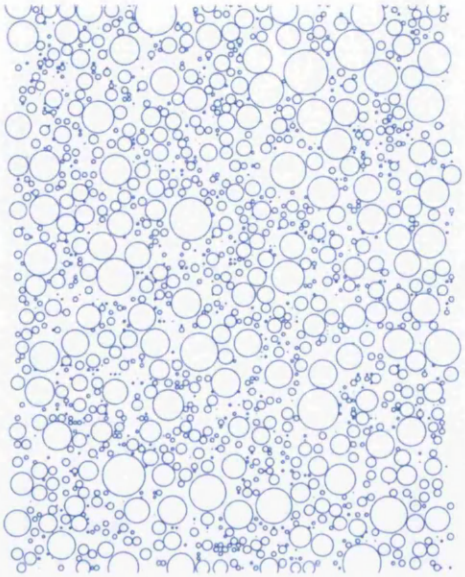

Figure 10.2: Simulation of surface deposition

By building on this work in the future we can start to make quantitative estimates of the expected pore size in a given film based on the casting conditions. This however is not expected to be any trivial task. The role of the polymer in the dynamics has not yet been included fully, exactly how to do this is not yet clear. The influence of incorporation of a polymer on solvent evaporation rates would be possibly the first logical objective to complete. Remaining questions are then related to how to carry out simulations describing nucleation and growth on the surface when describing systems whereby the polymer/solvent combination serves as to suppress droplet coalescence. At a microscopic level workers observe essentially non coalescing behaviour [7] in some material systems. Would it still be appropriate to place the critical nuclei at random locations and still allow these to coalesce as in the early work of Beysons and Knobler [10] or is it just the large droplets for which coalescence is suppressed and do these droplets grow by deposition of critical nuclei from above only. Also are the cavities that are observed in the final polymer film created by the deposited droplets when they have they're maximal size. These kind of issues could be considered on the basis of when the casting solution starts to show solid like behaviour, or when does the solutions gel point occur, presumably this will depend on the whole of the process dynamics. That is the solvent mass still remaining and the liquid temperature, which are functions of the deposited mass, solvent used and the

casting conditions (Flow rate etc).

From an experimental point it seems as though updating our method of deposition of the casting fluid is essential. Long range order is available within the context of our apparatus but reproducibility is an issue. The apparatus will continue to be modified and using the image analysis technique improvements can now be quantified. It is intended that eventually the process will not involve human intervention at all and the casting conditions will be created with high precision. A new experimental setup is needed to include flow in the process also, this will then truly allow comparison to the numerical model. Using the image analysis method it will be very interesting to see whether pore-size and ordering distributions are dramatically changed across the film surface with relation to theoretical ideas.

Chapter 11

Appendix

11.1 Binary Liquid Activity Coefficient Calculation For Water-CS_2

In the binary mixture of consideration, we only have two molecules, each of which belong to their own structural group, which makes the calculation much simpler. Ie carbon-disulphide contains only one molecule which is group 28, so ${V_{28}}^{(1)} = 1$. So

$r_1 = \sum_k {v_k}^{(i)} R_k = (1)(2.0576)$

and similarly for $q_1 = 1.6576$

, $q_2 = 1.4$ and $r_2 = 0.920$

it follows that

$l_1 = \frac{z}{2}(r_1 - q_1) - (r_1 - 1) = 0.9504$ and

$l_2 = -2.32$

$\phi_1 = \frac{r_1 x_1}{\sum_j q_j x_j} = \frac{2.0576 x_1}{(x_1)(2.0576)+(x_2 0.920)}$

and

$\phi_2 = \frac{r_2 x_2}{\sum_j q_j x_j} = \frac{0{,}920 x_1}{(x_1)(2.0576)+(x_2 0.920)}$

similarly for

$\theta_1 = \frac{q_1 x_1}{\sum_j q_j x_j} = \frac{1.656 x_1}{1.656 x_1 + 1.4 x_2}$

and

$\theta_1 = \frac{q_2 x_1}{\sum_j q_j x_j} = \frac{1.4 x_2}{1.656 x_1 + 1.4 x_2}$

Now, the combinatorial contribution, to the activity coefficient, can be calculated for both species by substituting the values calculated above, into equation 3.12.

$$ln\gamma_i^{C\ Combinatorial} = ln\frac{\phi_i}{x_i} + \frac{z}{2} q_i ln\frac{\theta_i}{\phi_i} + l_i - \frac{\phi_i}{x_i}\sum_j x_j l_j \qquad (11.1)$$

In order to calculate the residual part of the activity coefficient we need to calculate the group interaction parameter ψ_{mn}, using tabulated values of the interaction parameter a_{mn} .

$a_{28,7} = 1081K$, $a_{7,28} = 887.1K$, $a_{7,7}0$ and $a_{28,28} = 0$ this permits calculation of ψ_{mn} which is a temperature dependant function given by 3.22.

$\psi_{28,7} = exp(-\frac{U_{28,7} - U_{7,28}}{RT}) = exp(-\frac{1081}{T})$

and similarly

$\psi_{7,28} = exp(-\frac{887.1}{T})$

also $\psi_{7,7} = \psi_{28,28} = 1$

at this stage the group residual activity coefficient of group k should be calculated in a reference solution containing only molecules of type i ,however in the binary mixture of consideration both molecules only contain molecules from one main group so the group residual coefficient is zero . In order to calculate the group activity coefficient $ln\Gamma_k$, we must calculate θ_m using

$$\theta_m = \frac{\mathcal{Q}_m \mathcal{X}_m}{\sum_n \mathcal{Q}_n \mathcal{X}_n} \tag{11.2}$$

Where $\mathcal{X}_m$ is the mole fraction of group m in the mixture . Since in this case there are two molecules and two groups these values are just the values of the mole fractions for the molecules in the mixture.

so $\theta_1 = \frac{x_1 \mathcal{Q}_1}{x_1 \mathcal{Q}_1 + x_2 \mathcal{Q}_2}$

$\theta_2 = \frac{x_2 \mathcal{Q}_2}{x_2 \mathcal{Q}_1 + x_2 \mathcal{Q}_2}$

We can now calculate the group activity coefficient $ln\Gamma_k$ according to

$$ln\Gamma_k = Q_k \left[1 - ln(\sum_m \theta_m \psi_{mk}) - \sum_m \frac{\theta_m psi_{km}}{\sum_n \theta_n n \psi_{nm}} \right] \tag{11.3}$$

giving the expressions for $ln\Gamma_1$ and $ln\Gamma_2$ as

$ln\Gamma_1 = Q_1 \left[1 - ln(\theta_1 \psi_{11} + \theta_2 \psi_{21}) - \left\{ \frac{\theta_1 \psi_{11}}{\theta_1 \psi_{11} + \theta_2 \psi_{21}} + \frac{\theta_2 \psi_{12}}{\theta_1 \psi_{12} + \theta_2 \psi_{22}} \right\} \right]$

and

$ln\Gamma_2 = Q_2 \left[1 - ln(\theta_1 \psi_{12} + \theta_2 \psi_{22}) - \left\{ \frac{\theta_1 \psi_{21}}{\theta_1 \psi_{11} + \theta_2 \psi_{21}} + \frac{\theta_2 \psi_{22}}{\theta_1 \psi_{12} + \theta_2 \psi_{22}} \right\} \right]$

Substitution of the above expressions into 11.4

$$ln\gamma_i^{R\,Residual} = \sum_k v_k{}^i (ln\Gamma_k - ln\Gamma_k{}^{(i)}) \tag{11.4}$$

and using 11.5

$$ln(\gamma_i) = ln\gamma_i^{C\,Combinatorial} + \gamma_i^{R\,Residual} \tag{11.5}$$

yields the expression for the activity coefficients for both species

11.2 Transport Equation Using A Cubic Velocity Profile Within The Blasius Boundary Layer

Using a cubic velocity profile within the boundary which reaches V_x at the edge

$$3\frac{U_s}{2}\frac{z}{4.99(\frac{\nu}{U_x})^{\frac{1}{2}}}\left(\frac{Z}{\sqrt{x}}\right) - 3\frac{U_s}{2}\frac{z}{4.99(\frac{\nu}{U_x})^{\frac{3}{2}}}\left(\frac{Z}{\sqrt{x}}\right)^3 \tag{11.6}$$

let $\frac{Z}{\sqrt{x}} = \xi$

Now using this velocity profile in the transport equation above the sample solution, instead of a constant velocity gives;

$$3\frac{U_s}{2}\frac{z}{4.99(\frac{\nu}{U_x})^{\frac{1}{2}}}(\xi) - 3\frac{U_s}{2}\frac{z}{4.99(\frac{\nu}{U_x})^{\frac{3}{2}}}(\xi)^3\frac{\partial Cx,z}{\partial x} = D\frac{\partial^2 C(x,z)}{\partial z^2} \tag{11.7}$$

Expressing the derivatives in terms of ξ

$$\frac{\partial \xi}{\partial x} = -\frac{1}{2}\frac{Z}{x^{\frac{3}{2}}} \tag{11.8}$$

and

$$\frac{\partial \xi}{\partial z} = -\frac{1}{\sqrt{x}} \tag{11.9}$$

$$\frac{\partial C}{\partial x} = \frac{\partial C}{\partial \xi}\frac{\partial \xi}{\partial x} = -\frac{1}{2}\frac{Z}{x^{\frac{3}{2}}}\frac{\partial C}{\partial \xi} \tag{11.10}$$

and

$$\frac{\partial^2 C}{\partial Z^2} = \frac{\partial}{\partial Z}\left(\frac{\partial C}{\partial Z}\right) = \frac{\partial}{\partial Z}\left(\frac{\partial C}{\partial \xi}\frac{\partial \xi}{\partial y}\right) = \frac{\partial}{\partial Z}\left(\frac{1}{\sqrt{x}}\frac{\partial \xi}{\partial Z}\right) = \frac{1}{\sqrt{x}}\frac{\partial^2 C}{\partial \xi^2}\frac{\partial \xi}{\partial Z} = \left(\frac{1}{\sqrt{x}}\right)^2\frac{\partial^2 C}{\partial \xi^2} \tag{11.11}$$

setting $\frac{1}{4.99\sqrt{\frac{\nu}{U_x}}} = \alpha$and $\gamma_z = \frac{2D_z}{U_x}$ then substituting in for the derivatives gives

$$\left(3\alpha\xi - \alpha^3\xi^3\right) - \frac{1}{2}\frac{Z}{x^{\frac{3}{2}}}\frac{\partial C}{\partial \xi} = \gamma_z\left(\frac{1}{\sqrt{x}}\right)^2\frac{\partial^2 C}{\partial \xi^2} \tag{11.12}$$

$\frac{xZ}{x^{\frac{3}{2}}} = \frac{Z}{\sqrt{x}} = \xi$

This then gives the equation

$$\left(\frac{\alpha^3\xi^4}{2} - \frac{3}{2}\alpha\xi^2\right)\frac{\partial C}{\partial \xi} = \gamma_z\frac{\partial^2 C}{\partial \xi^2} \tag{11.13}$$

Bibliography

[1] Bishnu.P.Khanal and Eugene R Zubarev. Rings of nanorods. *Angewandte.chem.int.ed.2007*, 46:2195–2198, 2007.

[2] Sahill Kapur. *Photolithography:An Overview.* Siam, 1985.

[3] O.D.Velev, T. A. Jede, R.F.Lobo, and A. M. Lenhoff. Microstructured porous silica obtained via colloidal crystal templates. *Prepared for Presentation at 1998 Annual AIChE Meeting Session 203 Nanostructured Materials*, 61(1):1–21, 1998.

[4] Byron Gates, Yadong Yin, and Younan Xia. Fabrication and characterization of pourous membranes with highly ordered three dimensional periodic structures. *Chem Matter*, 11:2827–2836, 1999.

[5] A.J.Imhof and A.J.Pine. Uniform macroporous ceramics and plastics by emulsion templating. *Advanced Materials*, 10(9):697–700, 1998.

[6] H.G.Braun and E.Meyer. Thin microstructured polymer films by surface -directed film formation. *Thin Solid films*, 345:222–228, 1999.

[7] M.s.Barrow, R.L.Jones, and C.J.wright. Physical characterissation of micropourous and nanoporous polymer films by atomic force microscopy,scanning electron microscopy and high speed video microphotography. *Spectroscopy*, 18:577–585, 2004.

[8] Song Lulu. *Study Of Ordered Macropurous Polymer Films By Templating Breath Figures.* PhD thesis, Georgia Institute Of Technology, 2005.

[9] Serge Ulrich, Serge Stoll, and Emile Pefferkorn. Computer simulations of homogenous deposition of liquid droplets. *Langmuir*, 20:1763–1771, 2003.

[10] A.Steyer, P.Guenoun, and D.Beysens. Growth of droplets on a substrate by diffusion and coalescence. *Physical Review A*, 44(12), 1991.

[11] J.Aitken. *Nature*, 86:515, 1911.

[12] Rayleigh. Breath figures. *Nature*, 18(5):416–417, 1911.

[13] D.Beysons and C.M. Knobler. Growth of breath figures. *Physical Review Letters*, 57(12):1344–1347, 1986.

[14] C.M.Knobler and D.Beysens. Growth of breath figures on fluid surfaces. *Europhysics letters*, 15:707–712, 1988.

[15] G.Widawski, M.Rawiso, and B. Franois. Self-organized honeycomb morphology of star-polymer polystyrene films. *Nature*, 367:387, 1994.

[16] J.Li, Zhang Long, and P.Gopalakrishnakone. Ordered honeycomb-structured polymer films by a breath figure method in vacuum. *4th Kaula Lumper conference on Biomedical engineering 2008*, 23:337–340, 2008.

[17] M.Srinivasarao, D.Collings, A.Philips, and S. Patel. Three-dimensionally ordered array of air bubbles in a polymer film. *science*, 292:79, 2001.

[18] A.V.Limaye, R.D.Narhe, A.M.Dhote, and S.B.Ogale. Evidence for convective effects in breath figure formation on volatile fluid surfaces. *Physical Review Letters*, 76(20):3762–3765, 1996.

[19] R.Monti, R.Savino, and G.Alterio. Pushing of liquid drops by the marangoni. *Acta Astronautica*, 51(11):789, 2001.

[20] Q. S. Liu and B. Roux. Marangoni convection in immiscible double liquid layers. *Microgravity Science and Technology*, 7:103–111, July 1994.

[21] S. J. Tavener and K. A. Cliffe. Two-fluid marangoni-bernard convection with a deformable interface. *J. Comput. Phys.*, 182(1):277–300, 2002.

[22] R.Monti and R.Savino. Modelling of non-coalescing liquid drops in the presence of thermocapillary convection. *Meccanica*, 3:115–133, 1996.

[23] M.H.Stenzel. Formation of regular honeycomb patterned pourous films by self organization. *Aust.J.Chem*, 55(239):na, 2002.

[24] O.Pitois and B.Francois. Formation of micropourous membranes. *Eur.Phys*, 8(2225), 1999.

[25] O.Pitois and B.Francois. Crystallization of condensation droplets on a liquid surface. *Colloid Polym Sci*, 277(Na):574–578, 1999.

[26] M.Shimomura and T Sawadaishi. Bottom up stradegy of materials fabrication:a new trend in nanotechnology of soft materials. *Elsevier*, 6:11–16, 2001.

[27] O.Karthaus and N.Maruyama. Water-assisted formation of micrometer-size honeycomb patterns of polymers. *Langmuir*, 16(15):6071, 2000.

[28] A.Boker, Y.Lin, K.Chiapperini, and R.Horowitz. Hierarchical nanoparticle assemblies formed by decorating breath figures. *Nat. Mater.*, 3:302–306, 2004.

[29] B de Boer, U. Stalmach, H. Nijland, and G. Hadziioannou. Microporous honeycomb-structured films of semiconducting block copolymers and their use as patterned templates. *Advanced Mater.*, 12:1281, 2000.

[30] X.Zhao, Q.Cai, and G.Shi. Formation of ordered microporous films with water as templates from poly(d,l-lactic-co-glycolic acid) solution. *J. Appl. Polym. Sci.*, 90:1846, 2003.

[31] M.H.Stenzel-Rosenbaum, T. P. Davis, A.G.Fane, and V. Chen. Porous polymer films and honeycomb structures made by the self-organization

of well-defined macromolecular structures created by living radical polymerization techniques. *Angew. Chem. Int.*, 40:3428, 2001.

[32] S.Yunus, A.Delecorte, C.Poleunis, P.Bertrand, A.Bolognesi, and C.Botta. A route to self organised honeycomb microstructered polysyrene films and their chemical characterization by tof-sims imagaing. *Advanced Materials*, 17:1079–1084, 2007.

[33] Luke.A.Connal and Greg.G.Qiao. Honeycomb coated particles,pourous doughnuts,golf balls and hollow pourous pockets. *Soft matter*, 3:837–839, 2007.

[34] V.Berger. From photonic band gaps to refractive index engineering. *Optical Materials*, 11:131–142, 1999.

[35] M.Haupt, S.Miller, R.Sauer, k.Thonke, A.Mourann, and M.Moeller. Breath figures:self-organizing masks for the fabrication of photonic crystals and dichroic filters. *Jornal of applied Physics*, 96(6):3065–3069, 2004.

[36] D.Beattie, K.Wong.C.Williams, L.Warren, T.Davis, C.B.kowollik, and M.Stenzel. Honeycomb-structured pourous films from polypyrrole-containing block copolymers prepared via raft polymerization as a scaffold for cell growth. *Biomacromolecules*, 7:1072–1082, 2006.

[37] Fereydoon Family and Paul Meakin. Kinetics of droplet growth processes:simulations, theory and experiments. *Physical Review A*, 40(7):3836–3853, 1989.

[38] B j.Briscoe and K.P Galvin. The evolution of 2d constrained growth system of droplets-breath figures. *J.Phys.D:Appl.Phys*, 23:422–428, 1990.

[39] L.J.Delaney and L.C.Eagleton. *AIChe*, 8:418–420, 1962.

[40] Neil.Pieterse and Walter.W.Focke. Diffusion-controlled evaporation through a stagnant gas:estimating low vapour pressures from thermogravimateric data. *thermochimica Acta*, 406:191–198, 2003.

[41] Robert.C.Reid, John.M.Prausnitz, and Bruce.E.Pouling. *The properties of liquids and gases.* Mcgram Hill, 1986.

[42] Various. *Photolithography:An Overview.* McGraw-Hill, 1997.

[43] E.N.Fuller, P.D.Schettler, and J.C.Giddings. *Industrial Chemical Enginnering*, 11:19–27, 1966.

[44] Marcia.Ascher. Explicit solutions of the one dimensional heat equation for a composite wall. *Mathematics of computation*, 14:346–353, 1960.

[45] P.F.Peterson. Diffusion layer modelling for condensation with multicomponent noncondensable gases. *Journal of heat transfer*, 122:716–720, 2000.

[46] J.M.Coulson and J.F.Richardsons. *Chemical Engineering volume 1 (Fluid Dlow,Heat Transfer and Mass Transfer).* Elseveir, 2004.

[47] J.A.Dowdy and N.S.Karbash. Experimental determination of heat and mass transfer coefficients in rigid impregnated cellilose evaporative media. *ASHRAE Transactions part 2*, 93:382–395, 2003.

[48] J.R.Camargo and C.D.Ebinuma. A mathematical model for direct evaporative cooling air conditioning system. *engenharia termica*, 4:30–34, 2003.

[49] Marcos.B.Bellorio and Joao.M.D.Pimenta. Theoretical analaysis of air conditioning by evaporative cooling influence on gas turbine cycles performence. *18th international congree of mechanical engineering*, 2003.

[50] Mark.S.Gockenbach. *Partial Differential Equations.* Siam, 2002.

[51] R. D. Deegan, O. Bakajin, T. F. Dupont, G. Huber, S. R. Nagel, and T. A. Witten. Capillary flow as the cause of ring stains from dried liquid drops. *nature*, 389:827–829, October 1997.

[52] Martina.H.Stenzel. Formation of regular honeycomb-patterned porous polymer films by self organization. *Aust.J.chem*, 55:239–243, 2002.

[53] R.Taylor and R.Krishna. *Multicomponent Mass Transfer.* Wiley series in chemical engineering, 1993.